UNIVERSITY OF COPENHAGEN
FACULTY OF SCIENCE

Master's Thesis in Physics

Modeling Lasing in a Thermal Strontium Ensemble

Mikkel Tang

Supervisors: Stefan Alaric Schäffer and Jan Westenkær Thomsen

Niels Bohr Institute
6th of August, 2018

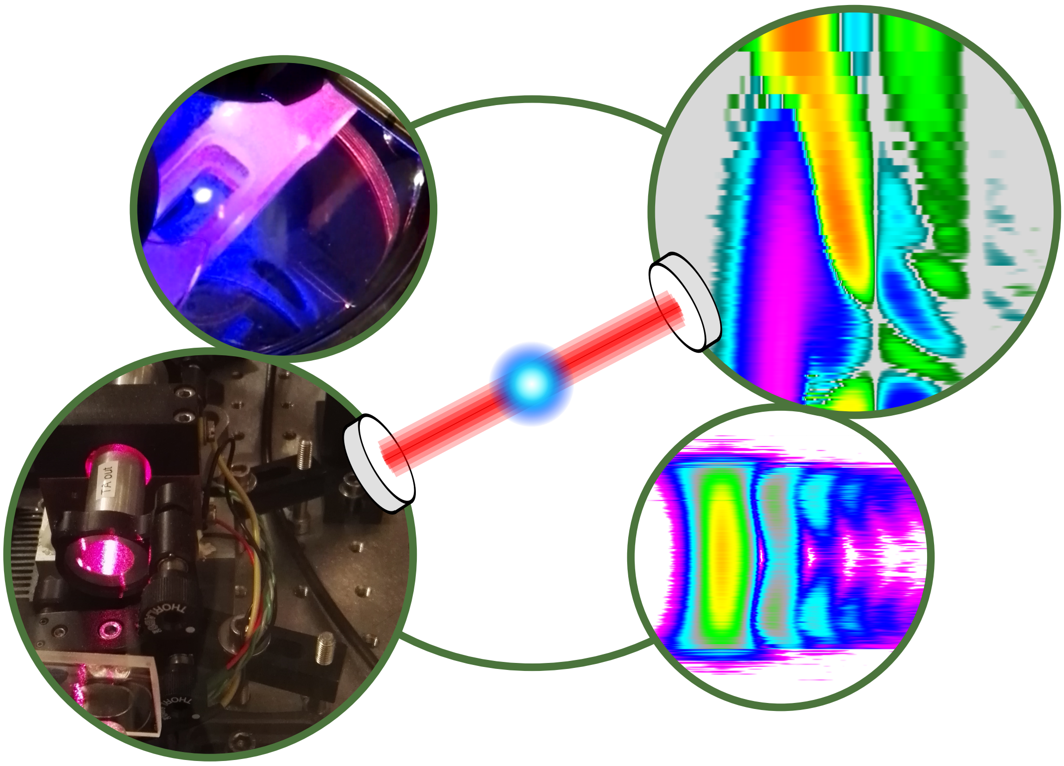

Acknowledgements

I would like to thank my supervisor, Stefan Alaric Schäffer, for the great amount of effort he has put into teaching me skills in the lab, his big share in our experimental work, and our physics discussions. These, his feedback and critical questions have been indispensable in improving the model and setup from the initial state and in obtaining the experimental results presented in this thesis.

I would also like to thank my other supervisor, Jan Westenkær Thomsen. He helped to put the project on tracks from the very beginning and taught me many things about the setup, and about the theory of superradiance, with great enthusiasm. Despite becoming very busy as head of institute, he still found time for a meeting whenever I had something to discuss, and our many group meetings.

I am also grateful to Asbjørn Arvad Jørgensen and Martin Romme Henriksen, two Ph.D. students in our group, who both have offered a lot of help in the lab and feedback on my work throughout the project.

The cooperation with three (now graduated) bachelor students, Mads Tønnes, Mikkel Ibsen and Christian Bærentsen, from the beginning of the project in 2016 through 2017 has also been indispensible for the project, for which I am thankful. Their experimental work allowed me to compare the initial model to real data and they also deserve a big share of the credit in upgrading our experimental setup.

I would like to thank Jörg Helge Müller from QUANTOP and Anders Søndberg Sørensen and Luca Dellantonio from Theoretical Quantum Optics. I have had several discussions with them about the physics of the system and the model which have taught me a lot.

Finally I would like to thank Martin Hayhurst Appel, who worked on the model before me. Inheriting his progress has, no doubt, been a lot faster than it would have been to start from scratch.

Abstract

The fields of laser physics and quantum optics have sparked countless technological applications and are important for high-precision frequency measurements, where the interactions between laser beams, optical cavities and atoms are used to obtain frequencies with unprecedented stability. These stable frequency references see applications in the global positioning system, test of fundamental physics and are now being used to detect gravitational waves. There are big prospects for optical frequency references actively stabilized to narrow atomic transitions using cold atoms and atomic ensembles [1] [2].

Here we present a model of a thermal ensemble of atoms interacting with a pump pulse and cavity mode, including the possibility of a laser driving the optical cavity. The goal is to accurately model our proof-of-principle experimental system, which utilizes a mK ensemble of laser-cooled Strontium to stabilize a cavity to the narrow $^1S_0$ - $^3P_1$ transition. We use this model to investigate the influence of the different experimental parameters on the system dynamics during the pump pulse and lasing process, and to predict the potential advantages of upgrading the pump pulse power, beam angle, beam profile or constructing a second stage MOT for cooling on the $^1S_0$ - $^3P_1$ transition. Based on the predictions, the pump pulse power was upgraded, which is also documented in this thesis.

To test the model we present experimental results which are compared to model predictions. These include Rabi oscillations due to the pump pulse and how the lasing dynamics depend on the number of atoms and the seed laser power. We also present results for how the dynamics depend on the cavity detuning, where we observe oscillations in the cavity output power, which the model offers insight into by looking at the ensemble in both spatial groups and velocity-groups. We find several qualitative features of the model experimentally. Quantitative comparisons are limited by high uncertainties on especially the temperature and the precise ensemble location, in addition to systematic bias in simulations due to approximations which require a large amount of processing power to eliminate. Experiments with varying number of atoms and especially varying seed laser power show good prospects for using the model quantitatively, while our results from experiments with varying cavity detuning show features the model seems incapable of explaining quantitatively.

However it remains a promising tool for predicting the order of magnitude one can expect various experimental changes to have on the system, and offers the physical explanations for how many parameters influence the system. Based on this model we expect that the Doppler broadening of the ensemble limits the achievable frequency stability of the system. Building a second stage MOT would offer a great opportunity to test the model in a very different regime as well as improving the potential frequency stability.

Nomenclature

AOM	- Acousto-optic modulator
ASE	- Amplified spontaneous emission
APD	- Avalanche Photodetector
MOT	- Magneto-optical trap
ND filter	- Neutral-density filter
PBS	- Polarizing beam splitter
RF	- Radio frequency
SF	- Superfluorescence
SR	- Superradiance
SSEP	- Steady state excited population
TA	- Tapered amplifier

---

a, $a^\dagger$	- Cavity field annihilation/creation operators
$\vec{B}$	- Magnetic field
E	- Energy
$\vec{E}$, E_0	- Electric field/electric field amplitude
g_i	- Atom-cavity coupling parameter of atom i (angular frequency)
$\vec{k}, k$	- Wave vector/wavenumber
I	- Intensity
L	- Cavity length
N	- Number of ensemble atoms
N_g	- Number of atom groups
N_{pg}	- Number of atoms per atom group
P_{out}	- Cavity output power
P_p	- Pump pulse power
P_{seed}	- Seed laser power
R	- Ensemble density parameter
t_π, t_π^W	- Ensemble π pulse duration/π pulse duration for population within the cavity waist
T	- Temperature
y_{MOT}	- Ensemble offset along y axis with respect to MOT-field center
W, W_e	- Cavity mode waist radius
W_{pi}	- Pump pulse waist radius along axis i
Γ	- Linewidth of the ^{1}S$_0$ - ^{3}P$_1$ transition (angular frequency)
Δ	- Detuning
η	- Seed laser driving strength parameter
θ_p	- Angle of the pump pulse beam profile with respect to the xz-plane
κ	- Cavity linewidth (angular frequency)
σ_{ij}	- Atomic operators with state subscripts: g: ^{1}S$_0$, e: ^{3}P$_1$, c: ^{1}P$_1$
$\langle\sigma_{ee}\rangle$	- Expectation value of ^{3}P$_1$ (excited) population
$\langle\sigma_{ee}^S\rangle$	- Steady state excited population (SSEP)
$\langle\sigma_{ee}^W\rangle$	- Excited population within the cavity waist (also $\langle\sigma_{ee}\rangle_W$)
τ	- Characteristic transient time of AOM
ϕ_p	- Angle of the pump pulse beam with respect to the cavity (z) axis
χ	- Rabi frequency (angular)
ω	- Electronic transition frequency (angular)
Ω	- Generalized Rabi frequency (angular)

Contents

List of Figures

List of Tables

CHAPTER 1

Introduction

This project lies at the crossroads of two important technologies full of interesting physics: Atomic clocks and lasers. Atomic clocks set the record for providing the most precise measurements of any physical quantity, frequency, with fractional inaccuracies below 10^{-17} reported [3]. A clock with this stability could run for longer than the age of the universe and still keep track of the time that has passed with a precision better than a single second. Centuries ago we could measure time by counting the oscillations back and forth on a pendulum - if the frequency of the oscillations is stable, we have a good clock and can make precise measurements of time. In modern atomic clocks, it is instead electronic oscillations at optical THz frequencies that act as extremely stable pendulums.

Atomic clocks have many applications. The most striking example is the global positioning system (GPS) which deeply relies on the precision of atomic clocks on satellites in orbit. These satellites send a signal to the device we want to locate, and the device sends a signal back. By measuring the time it takes for these signals to propagate between the satellite and device at the speed of light, and accounting for the effects of special and general relativity, we can measure the distance between the satellite and the device. If the distance is known between the device and three satellites, the device can be located, and the more precisely the time can be measured with the atomic clocks, the more precisely we can locate the device. Today many areas of research also rely on atomic clocks with high precision, for example the discovery of gravitational waves in 2016 [4].

Atomic clocks rely on the physics of lasers, which are required to generate light with the extremely narrow spectral features required for probing the electronic transitions. In our case the system is also itself a form of pulsed laser - the atomic ensemble of Strontium used in our setup is a gain medium located within an optical cavity. Thus laser physics is important for our system, but also has applications for a broad range of other areas. Lasers are used today in areas spanning from eye surgery, welding and cutting metal, to reading barcodes or data stored on optical discs [5, p. 8].

1.1 Introduction to the Strontium Clock Experiment

The main objective of this work is to model the physics of our quasi-continuous proof-of-principle system utilizing cold ^{88}Sr for frequency stabilization, so that we can describe the physics governing the system and make quantitative predictions to guide our experimental work towards improving its performance. This section will give a brief overview of the experimental setup.

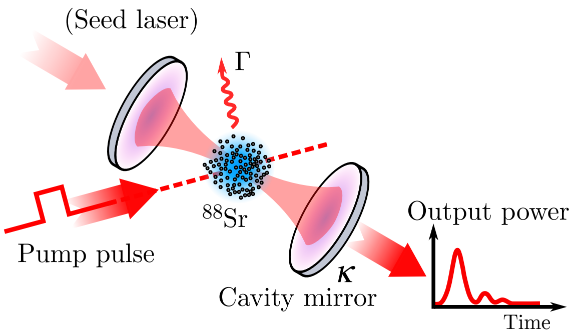

Figure 1.1: *Illustration of the atomic ensemble and its environment, excluding the MOT beams. The ensemble is excited by a pump pulse. After this, a lasing process occurs in the cavity mode which we can monitor by observing the output power. We have the option of driving the cavity with a seed laser, stimulating the lasing process.*

To capture and cool the Strontium atoms, an oven heats up a Strontium sample, generating a vapor pressure of atoms that propagate through an opening, forming a beam. This beam of atoms is slowed and cooled by a Zeeman slower while propagating into a vacuum chamber. The atoms are finally trapped, forming an ensemble, and further cooled to a few mK by a Magneto-Optical Trap (MOT), using the $^1S_0$ - $^1P_1$ transition. The ensemble is located within an optical cavity supporting a mode with the frequency of the $^1S_0$ - $^3P_1$ transition (see the level structure on Fig. 1.2). This transition is dipole-forbidden and has a narrow linewidth of $\Gamma = 2\pi \cdot 7.5$ kHz, which is what gives it potential for use in an atomic clock.

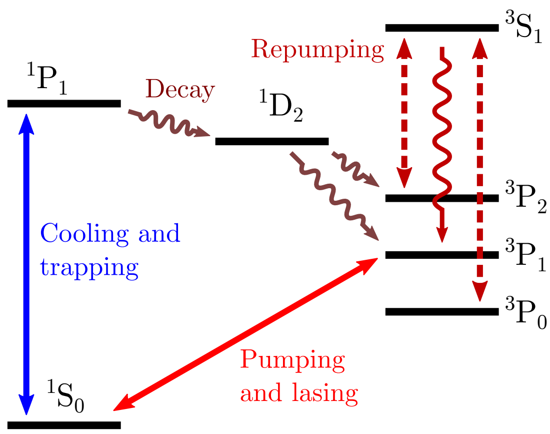

Figure 1.2: *The relevant level structure and electronic transitions for the experiment. Squiggly lines are decay channels, while full and dotted lines are also driven by lasers.*

However the ensemble has a temperature of a few mK, which gives it a Doppler broadening of a few MHz that could limit our frequency stability. But if the ensemble radiates into the cavity mode with a linewidth near the single-atom linewidth (illustrated on Fig. 1.1), the setup could be used as a very stable frequency reference. Then the experiment would operate in the bad cavity regime (the cavity has a linewidth of 620 kHz), and noise due to the cavity mechanics would be reduced [2, p. 1]. Our system using a single transition for MOT cooling has the advantage of being relatively simple and being able to trap many atoms ($N \sim 10^8$). For comparison others [6] have used the $^1S_0$ - $^3P_1$ transition for second stage cooling an ^{87}Sr ensemble to a few μK. By subsequently trapping ~2000 of the atoms in an optical lattice, they obtained a fractional absolute frequency uncertainty of $2.1 \cdot 10^{-18}$.

To obtain a signal with the stable frequency of the $^1S_0$ - $^3P_1$ transition, we need the atoms to radiate into the cavity mode. This is done by using a cycle of laser pulses shown on Fig. 1.3. For a majority of the time, MOT lasers are cooling the atoms on the $^1S_0$ - $^1P_1$ transition. When the MOT beams are off, we expose the atoms to a pump pulse on the $^1S_0$ - $^3P_1$ transition, exciting typically about 70 % of the atoms within the cavity mode. This inversion means that if one atom spontaneously emits into the cavity mode, stimulated emission by other atoms will amplify the light, resulting in a lasing pulse in the cavity mode. Thus our system acts as a pulsed laser, and is capable of operating either on its own as a master laser, or as a gain medium for an input seed laser field (see Fig. 1.1). We observe the lasing pulse in the output power of the cavity. Our objective is for this signal to have as high a frequency stability as possible, and also a high intensity so that the signal to noise ratio is high.

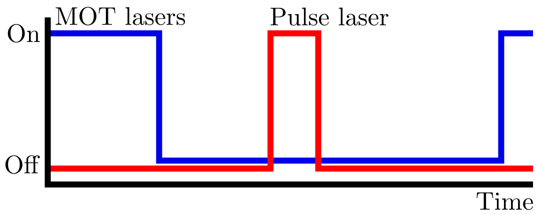

Figure 1.3: *Typical laser sequence while operating the experiment. The whole cycle typically lasts at least 500 µs - the MOT lasers may be off for 100 µs, and the pump pulse on for 100-200 ns.*

The project should be seen in the context of the status of the experiment when the project began in February 2016. At this time the pump pulse was capable of delivering about 20 mW, exciting about 28 % of the ensemble atoms. We had only observed lasing pulses with the seed laser on - the system worked as a slave laser, but not as a master laser.

1.2 Outline of the Thesis

In chapter 2 we present the theoretical building blocks for understanding the system, focusing on smaller components of the system: The cavity interacting with the seed laser and a single atom interacting with a cavity mode. In chapter 3 we extend the model to an ensemble of atoms and include the interaction with the pump pulse. We investigate the ensemble dynamics due to the pump pulse, and the lasing dynamics after the pulse. In chapter 4 we present the experimental work on the setup related to upgrading the pump pulse for improving the experiments. In chapter 5 we present the experimental results for determining the parameters that are important for the model, results on the properties of the ensemble, and compare them to the model predictions. In chapter 6 we look at the prospects of second-stage cooling based on simulations. Throughout the report, we will be using a coordinate system as illustrated in Fig. 1.4.

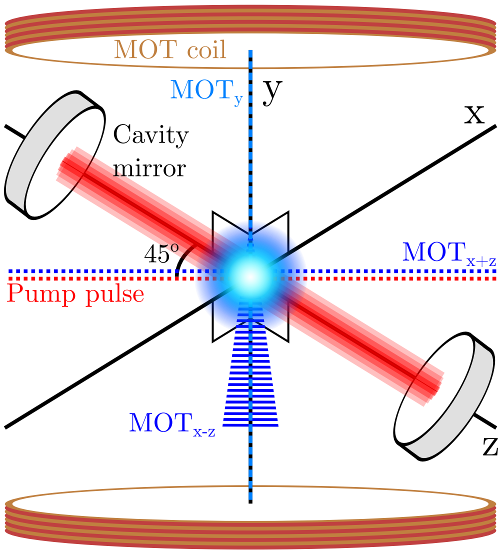

Figure 1.4: *The coordinate system used in this thesis.*

CHAPTER 2

Cavity Quantum Electrodynamics with Cold Strontium

In our pulsed Strontium clock experiment we trap ^{88}Sr atoms in a MOT using the $^1S_0 - ^1P_1$ transition, and subsequently, the millions of atoms interact with the cavity mode and a pulse laser, both near the resonance of the $^1S_0$ - $^3P_1$ transition. In some of our experiments, the cavity is driven by a seed laser in addition. The physics of the basic components of the system are investigated in this section: the cavity and its interaction with a seed laser and single atoms. This will provide insight for interpreting our experiments and serve as a starting point for modeling the full system.

2.1 Time-dependence in Quantum Mechanics

The dynamics of the electronic structure of the Strontium atoms and its interaction with photons are described by quantum mechanics. In this theory the value of a matrix element, $\langle\psi(t)|A|\psi'(t)\rangle$, must not depend on how we choose to describe it. However this leaves choice for whether the states, $|\psi\rangle$, or the operators, A, carry the time dependence. This leads to three pictures [7, p. 80-85]:

The Schrödinger picture, where the states carry most or all of the time dependence and evolve according to Schrödinger's equation, with the solution:

$$|\psi_S(t)\rangle = e^{-iHt/\hbar}\,|\psi_S(0)\rangle \tag{2.1}$$

The Heisenberg picture, where all the time evolution is transferred from the states to the operators:

$$|\psi_H(t)\rangle = e^{iHt}\,|\psi_S(t)\rangle \qquad\qquad A_H(t) = e^{iHt}A_S e^{-iHt} \tag{2.2}$$

And an intermediate - the interaction picture - where only part of the time evolution, due to H_0, is transferred to the operators:

$$|\psi_I(t)\rangle = e^{iH_0t}\,|\psi_S(t)\rangle \qquad\qquad A_I(t) = e^{iH_0t}A_S e^{-iH_0t} \tag{2.3}$$

Here the full Hamiltonian has the form $H = H_0 + H_I(t)$. H_0 is chosen to be a time-independent, interaction-free part of the Hamiltonian, which gives trivial, analytical time-dependencies for the operators. This picture will be used extensively for describing the dynamics of our system.

For the system we are interested in, it is useful to consider the time evolution of expectation values, rather than operators, since the equations for millions of atoms would otherwise require immense computing power, and averaging on the atomic level should have little influence on the whole ensemble. In addition, we will make use of the Markov approximation, which states that the reservoir has no memory of its past. This approximation is valid under the condition [8, p. 669]:

$$t_S, t_R \ll \Delta t \ll t_D \tag{2.4}$$

Here t_S is the system timescale and t_R the reservoir correlation time. Δt is a coarse-grained timescale where the equations of motions are valid (such as timesteps in a numerical integration), and t_D is the decay timescale. In our case, the system timescale is on the scale of optical transition frequencies, $t_S \approx \omega_{ae}^{-1} \approx 10^{-16}$ s. The decay timescales are $t_D = \kappa^{-1} = 256$ ns for the cavity mode, and $\Gamma^{-1} = 21$ μs for the atoms. The reservoir correlation time may be estimated as the timescale of a photon traversing the ensemble, $R/c \approx 10^{-11}$s (neglecting back-scattering). On a timescale longer than this, a spontaneously emitted photon leaving one atom can no longer affect another atom in the ensemble - the reservoir "forgets" that the process has taken place and is back in the vacuum state. Thus we see that for our system, we can safely employ the Markov approximation and describe the system behavior on nanosecond timescales and upwards, as we are interested in. For a Markovian system coupled to an environment, the time evolution of the system can be modeled with a master equation. For an operator A in the interaction picture, this leads to the following time-evolution of the expectation value: [9, p. 14]:

$$\frac{d}{dt}\langle A\rangle = \frac{i}{\hbar}\langle [H_I, A]\rangle + \mathcal{L}(A) \tag{2.5}$$

Where $\mathcal{L}$ is the Lindblad superoperator, leading to decay terms.

2.2 Quantizing the Electromagnetic Field

The cavity mode is modeled as a quantized electric field. The basic idea behind quantizing the electromagnetic field is to find solutions to Maxwell's equations in vacuum, and write these in terms of variables resembling position and velocity/momentum [10, p. 10-15]. One demands that these variables are operators satisfying the canonical commutation relation. One can then define new operators - the annihilation and creation operators a and $a^\dagger$ - in terms of the canonical position and momentum operators. These satisfy the bosonic commutation relation $\left[a, a^\dagger\right] = 1$ and define the Fock/number space, where the energy of a single mode electromagnetic field is written as:

$$H = \hbar\omega\left(a^\dagger a + \frac{1}{2}\right) \tag{2.6}$$

Where $\hbar\omega$ is the energy per photon in the mode, $a^\dagger a = n$ is the number operator, representing the number of photons, and the factor $1/2$ represents zero-point energy.

2.3 An Optical Cavity Driven by a Laser

In the Schrödinger picture, the Hamiltonian of a single-mode cavity driven by a laser is given by [9, p. 14]:

$$H = \hbar\omega_e a_S^\dagger a_S + \frac{1}{2}\hbar\eta\left(a_S e^{-i\omega_s t} + a_S^\dagger e^{i\omega_s t}\right) \tag{2.7}$$

The first term represents the energy of the cavity mode with frequency ω_e - the zero-point term has been dropped because it commutes with the Hamiltonian and thus does not affect the dynamics we are interested in. The second term represents the interaction with the driving laser at one of the mirrors. The driving laser has frequency ω_s and a driving strength η. Defining an interaction picture with $H_0 = \hbar\omega_s a^\dagger a$ gives the interaction picture annihilation operator a in terms of the Schrödinger picture operator a_S:

$$\dot{a} = \frac{i}{\hbar}\left[\hbar\omega_s a^\dagger a, a\right] = -i\omega_s a \implies a = a(t=0)e^{-i\omega_s t} = a_S e^{-i\omega_s t} \tag{2.8}$$

The interaction Hamiltonian in the interaction picture becomes:

$$H_I = H - H_0 = \hbar\Delta_e a^\dagger a + \frac{1}{2}\hbar\eta\left(a + a^\dagger\right) \tag{2.9}$$

Using Eq. 2.5, the expectation value of the annihilation operator evolves according to:

$$\dot{\langle a \rangle} = -\frac{i}{2}\eta - \left(i\Delta_e + \frac{\kappa}{2}\right)\langle a \rangle \tag{2.10}$$

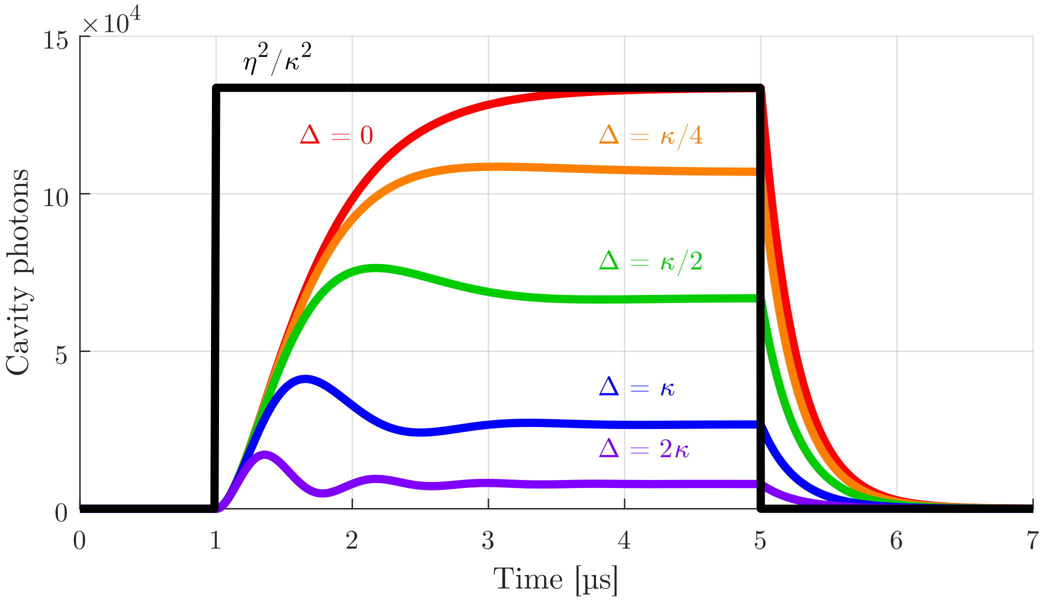

Figure 2.1: *Simulated dynamics of a cavity driven by a laser from t = 1 μs to 5 μs for various detunings. After 5 μs the intra-cavity photon population decays at a rate $\kappa = 2\pi\cdot$620 kHz, the cavity linewidth. The driving strength $\eta = 1.4 \cdot 10^9$ rad/s is used in this example, corresponding to a driving power P_{in} = 150 nW, a common value for our experiments.*

The steady state solution to Eq. 2.10 is $\langle a \rangle = \eta/(2\Delta_e + i\kappa)$, so the cavity photon number approaches $\langle n \rangle = \langle a^\dagger a \rangle = \eta^2/(\kappa^2 + 4\Delta_e^2)$ (one can show that for Eq. 2.9, $\langle a^\dagger a \rangle = \langle a^\dagger \rangle \langle a \rangle$, which simplifies the calculations). In Fig. 2.1, the dynamics of the cavity field are shown for various detunings, based on numeric integration of Eq. 2.10. The output power is $P_{out} = \hbar\omega_e n\kappa$, and in the steady state, this must be equal to the input power, assuming no reflection on the input mirror or absorption. This means η can be related to the power of the driving laser P_{in} by $\eta = \sqrt{P_{in}\kappa/\hbar\omega_e}$. Note that this model accounts for interference at the input mirror, and the output power P_{out} calculated here is the power leaking through the output mirror only - when the driving laser is on resonance with the cavity, destructive interference prevents the cavity mode from leaking through the input mirror.

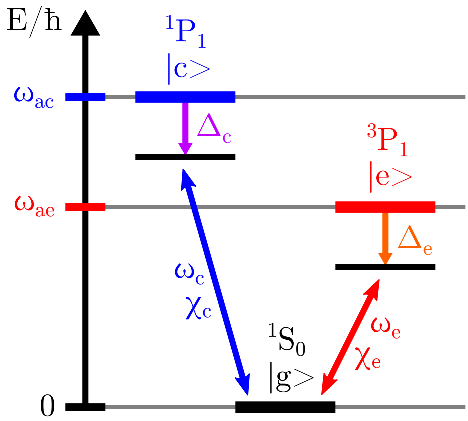

Figure 2.2: *Energies of the 3 level system. The laser detunings Δ are defined with respect to the atomic resonances ω_a, as $\omega_c = \omega_{ac} + \Delta_c$ (MOT lasers) and $\omega_e = \omega_{ae} + \Delta_e$ (cavity mode). The pump pulse has equivalent definitions for ω_p, χ_p and Δ_p.*

2.4 A Cavity with an Atom

To include the atoms in the model, we define the most relevant atomic energy levels like in Fig. 2.2. The level $|c\rangle$ (for *cooling*) refers to the $^1P_1$ state, $|g\rangle$ refers to the $^1S_0$ ground state, and $|e\rangle$ refers to the excited state $^3P_1$. With these definitions, the energy of a single atom in the cavity is given by H_a below. In the full model, there will be a sum of these terms, one for each atom.

$$H_a = \hbar\omega_{ae} |e\rangle\langle e| + \hbar\omega_{ac} |c\rangle\langle c| \tag{2.11}$$

In addition the model must include the interaction between the atoms and the lasers. In the dipole approximation the interaction energy of an atom in an electric field is given by $H = -e\hat{r} \cdot \hat{E}$ [5, p. 73]. For these interactions, the detuning of the various lasers with respect to the atomic energy levels will become relevant; the definition of these are also shown on Fig. 2.2. For the cavity mode, we may write the electric field as a standing wave:

$$\hat{E} = \hat{\epsilon} E_0 \left(a + a^\dagger\right) \sin(kz) \tag{2.12}$$

Where ϵ is the polarization unit vector. The dipole operator can be written:

$$\hat{d} = -\hat{\mu}\mu_0 \left(|g\rangle\langle e| + |e\rangle\langle g|\right) \tag{2.13}$$

Where $\hat{\mu}$ is the atomic dipole unit vector. Thus the interaction Hamiltonian becomes:

$$H_{ie} = (\hat{\mu} \cdot \hat{\epsilon})\, \mu_0 \left(|g\rangle\langle e| + |e\rangle\langle g|\right) E_0 \left(a + a^\dagger\right) \sin(kz) \tag{2.14}$$

The Hamiltonian governing our driven cavity with an atom can be written as (note all operators are in the Schrödinger picture):

$$\begin{aligned} H &= \hbar\omega_e a^\dagger a + \hbar\omega_{ae}\sigma_{ee} + \hbar\omega_{ac}\sigma_{cc} \\ &+ \frac{1}{2}\hbar\eta\left(ae^{-i\omega_s t} + a^\dagger e^{i\omega_s t}\right) + (\hat{\mu}\cdot\hat{\epsilon})\,\mu_0\left(\sigma_{ge}+\sigma_{eg}\right)E_0\left(a+a^\dagger\right)\sin(kz) \end{aligned} \tag{2.15}$$

Where the frequencies ω are defined in Fig. 2.2, and ω_s is the seed laser frequency. Defining an interaction picture with respect to $H_0 = \hbar\omega_s a^\dagger a + \hbar\omega_s\sigma_{ee} + \hbar\omega_c\rho_{cc}$ gives the interaction picture operators in terms of the Schrödinger picture ones: $a = a_S\exp(-i\omega_s t)$ and $\sigma_{ge} = \sigma_{ge}^S\exp(-i\omega_s t)$. In this picture, the interaction Hamiltonian becomes:

$$\begin{aligned} H &= \hbar\Delta_{es}a^\dagger a + \hbar\Delta_{as}\sigma_{ee} + \frac{1}{2}\hbar\eta\left(a+a^\dagger\right) \\ &+ (\hat{\mu}\cdot\hat{\epsilon})\,\mu_0\left(\sigma_{ge}e^{i\omega_s t} + \sigma_{eg}e^{-i\omega_s t}\right)E_0\left(ae^{i\omega_s t} + a^\dagger e^{-i\omega_s t}\right)\sin(kz) \end{aligned} \tag{2.16}$$

Where Δ_{es} is the detuning of the seed laser with respect to the cavity, and Δ_{as} the detuning of the seed laser with respect to the atomic transition. Now we can use the rotating wave approximation and drop the rapidly oscillating terms:

$$\begin{aligned} H &= \hbar\Delta_{es}a^\dagger a + \hbar\Delta_{as}\sigma_{ee} \\ &+ \frac{1}{2}\hbar\eta\left(a+a^\dagger\right) + (\hat{\mu}\cdot\hat{\epsilon})\,\mu_0 E_0\sin(kz)\left(\sigma_{ge}a^\dagger + \sigma_{eg}a\right) \end{aligned} \tag{2.17}$$

Using Eq. 2.5 results in three coupled equations of motion for the expectation values:

$$\langle\dot{a}\rangle = -\frac{i}{2}\eta - \left(i\Delta_{es} + \frac{\kappa}{2}\right)\langle a\rangle - ig\langle\sigma_{ge}\rangle \tag{2.18}$$

$$\langle\dot{\sigma_{ge}}\rangle = \left(i\Delta_{as} - \frac{\Gamma}{2}\right)\langle\sigma_{ge}\rangle + ig\left(\langle\sigma_{ee}a\rangle - \langle\sigma_{gg}a\rangle\right) \tag{2.19}$$

$$\langle\dot{\sigma_{ee}}\rangle = -\Gamma\sigma_{ee} + ig\left(\left\langle\sigma_{ge}a^\dagger\right\rangle - \langle\sigma_{eg}a\rangle\right) \tag{2.20}$$

Where the atom-cavity coupling parameter g from the dipole interaction terms has been defined by modeling the cavity mode as a symmetric Gaussian beam and defining z as the cavity axis:

$$g = \overbrace{\sqrt{\frac{6c^3\Gamma_{eg}\omega_e}{W_e^2 L\omega_{ae}^3}}}^{\text{Bare frequency } g_0} \cdot \overbrace{\sin\left(\frac{\omega_e z}{c}\right)}^{\text{Longitudinal mode}} \cdot \overbrace{\exp\left(-\frac{x^2+y^2}{W_e^2}\right)}^{\text{Transverse Gaussian mode}} \tag{2.21}$$

In terms of the cavity mode frequency ω_e, atomic transition frequency and linewidth ω_{ae} and Γ_{eg}, cavity mode waist radius W_e, cavity length L and atomic position (x, y, z). In principle, one would need more equations for the two-operator expectation values, and their equations of motion will then contain expectation values with three operators, and so on. Such a set of equations may possibly be closed using mean field approximations [7, chap. 4] and physically reasonable truncations. However, we are ultimately interested in describing a large ensemble - in our experiments, the cavity field will often contain thousands of photons spread out over a macroscopic mode volume (V $\approx$ 0.6 cm^3), leaking through the cavity mirrors and also interacting with thousands of atoms within the mode volume. We use these facts as a motivation for factorizing the expectation values for each operator. This is a semiclassical approximation that, in the final model describing the ensemble, leaves us with a number of differential equations scaling linearly with the number of atoms, which is crucial when there are about 100 million atoms. The resulting equations describe Rabi oscillations between $|g\rangle$ and $|e\rangle$ for the atoms, in the resonant case oscillating fully between the states with the Rabi frequency $\chi = 2g\sqrt{a^\dagger a}$, and in the detuned case, oscillating faster with the generalized Rabi frequency $\Omega = \sqrt{\chi^2 + \Delta_{as}^2}$, but with lower amplitudes. The fact that we have an ensemble of atoms moving at finite, thermal velocities along the cavity axis makes it interesting to investigate the effects of this motion. The position of the cavity mirrors may fluctuate in time due to thermal and mechanical effects, which may have a significant influence for the dynamics. Therefore we will study two cases: A cavity on resonance, and a detuned cavity.

2.4.1 An Atom Moving in a Resonant Cavity

If the cavity mode is on resonance with an atom with $v_z = 0$ along the cavity axis, the atom experiences an electric field oscillating at its resonance frequency, and undergoes damped Rabi oscillations until it reaches a steady state excited population $\langle\sigma_{ee}\rangle_S$ between 0 and 0.5, depending on the local field strength. If it is moving, it will additionally experience a slowly oscillating change in the electric field, and $\langle\sigma_{ee}\rangle$ will undergo oscillations with envelope period $t = \lambda/v_z$ after a transient time related to the atomic decay time Γ. Some examples of the dynamics are shown in Fig. 2.3.

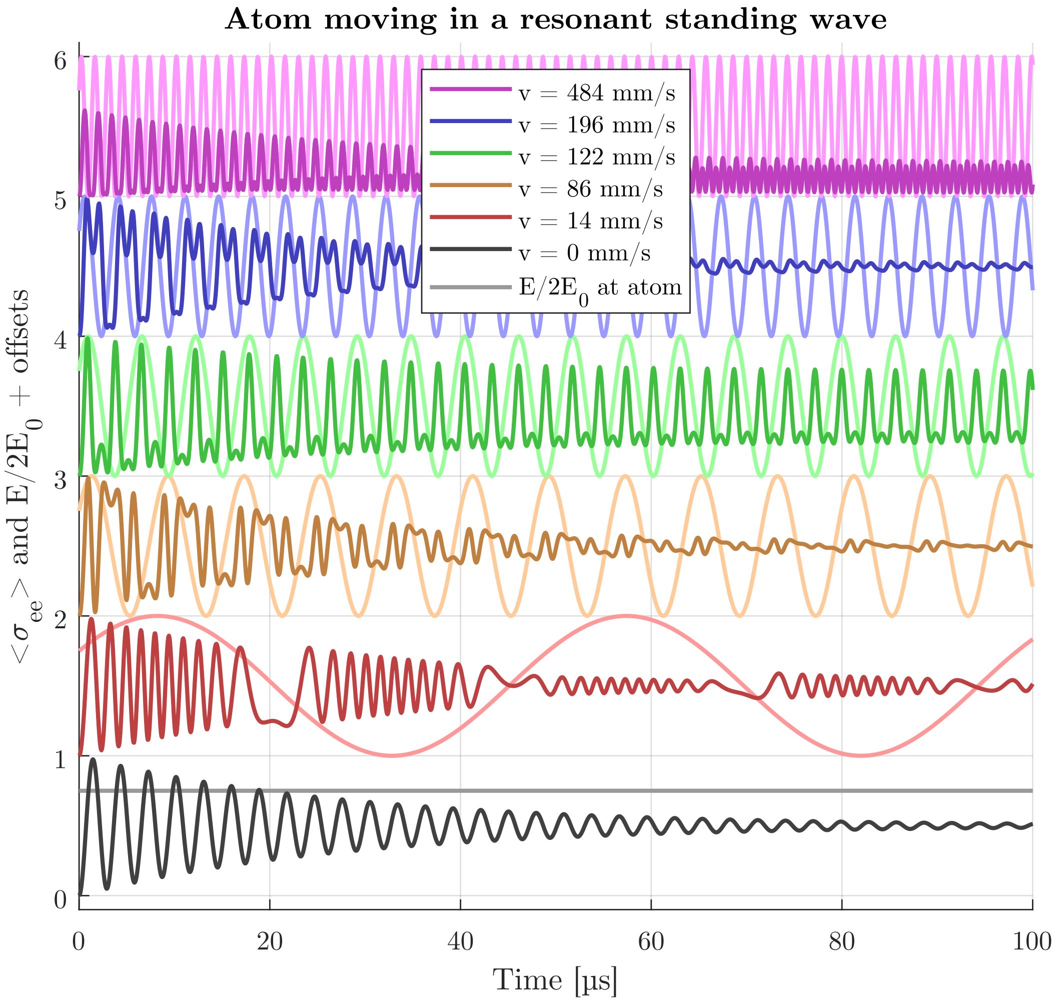

Figure 2.3: *The oscillations between ground and excited state of an atom in a cavity, for different velocities v along the cavity axis. The atoms undergo damped Rabi oscillations related to the local field strength, and the envelope of these oscillations are periodic with λ/v. The parameters used here are λ = 689 nm, $\Gamma = 2\pi\cdot 7.5$ kHz, P_{in} = 200 nW and $\kappa = 2\pi\cdot 620$ kHz. The brighter-colored lines represent the electric field at the location of the atom.*

Within the envelopes there may be fast oscillations if the electric field is intense, and the pattern of the oscillations strongly depends on the velocity of the atom. Fig. 2.3 reveals dynamics that may seem counter-intuitive: $\langle\sigma_{ee}\rangle_S$ approaches 0.5 for both 86 and 199 mm/s, but for 14 mm/s and 123 mm/s, $\langle\sigma_{ee}\rangle_S$ approaches 0.497 and 0.4, respectively. The dynamics can be interpreted by considering the standing wave cavity field as the mixture of two traveling waves with opposite Doppler shifts with respect to the atom. For high velocities $\langle\sigma_{ee}\rangle$ goes to 0, as both the traveling wave components become too far-detuned to interact with the atom. For simplicity, it is assumed $x = y = 0$ in this section - the effect of being located outside the beam center would lead to the same type of dynamics, but g reduced by a constant factor due to the Gaussian profile of the cavity mode.

To get an idea of how an atom with a given velocity couples to the cavity mode, $\langle\sigma_{ee}\rangle_S$ is found as a function of the atomic speed along the cavity axis, and the corresponding Doppler shift kv_z, by averaging $\langle\sigma_{ee}\rangle$ over the envelope period λ/v_z for atoms with a given v_z, a long time $\gg 1/\Gamma$ after the start of the simulation. This can be seen in Fig. 2.4, and interpreted similarly to a spectrum [11, p. 195]: The x axis shows the frequency corresponding to the Doppler shift of an atom with a given speed, and y-values for $\langle\sigma_{ee}\rangle_S$ close to 0.5 means the atom is interacting strongly enough for the transition to become saturated.

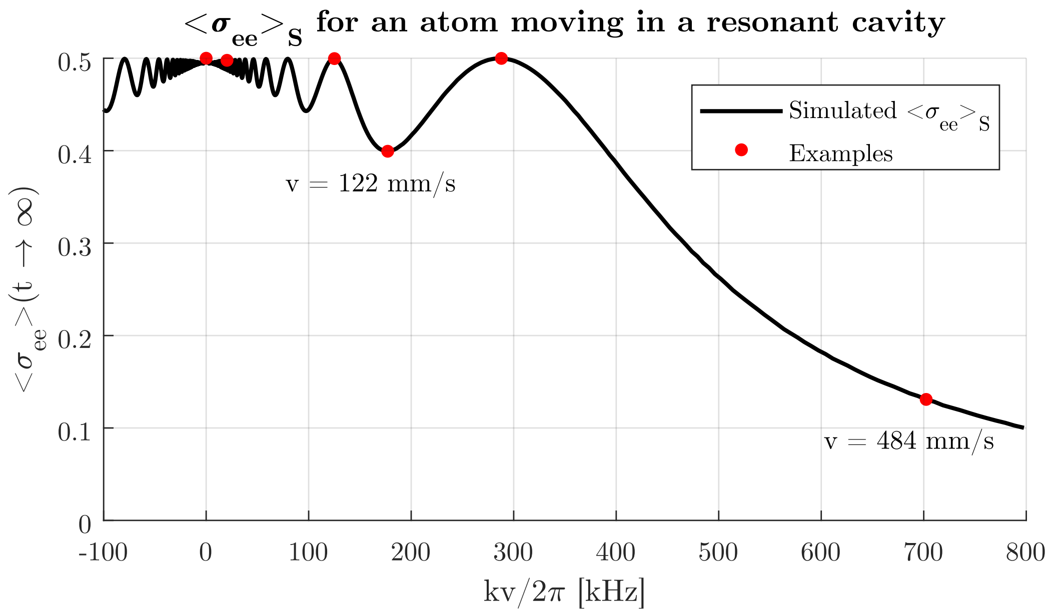

Figure 2.4: *Steady state excited population of an atom moving in a resonant standing wave with velocity v, as a function of the corresponding Doppler frequency $kv/2\pi$. The examples refer to the dynamics shown in Fig. 2.3, and the same parameters are used in this figure.*

The intra-cavity power is another important factor in the dynamics. This is investigated in Fig. 2.5, represented by the corresponding cavity input power. Here we see that for a low power, $\langle\sigma_{ee}\rangle_S$ is only non-zero for atoms that move very slowly along the cavity axis. However, for increasing power, atoms with higher velocities may couple to the field, as expected from power broadening.

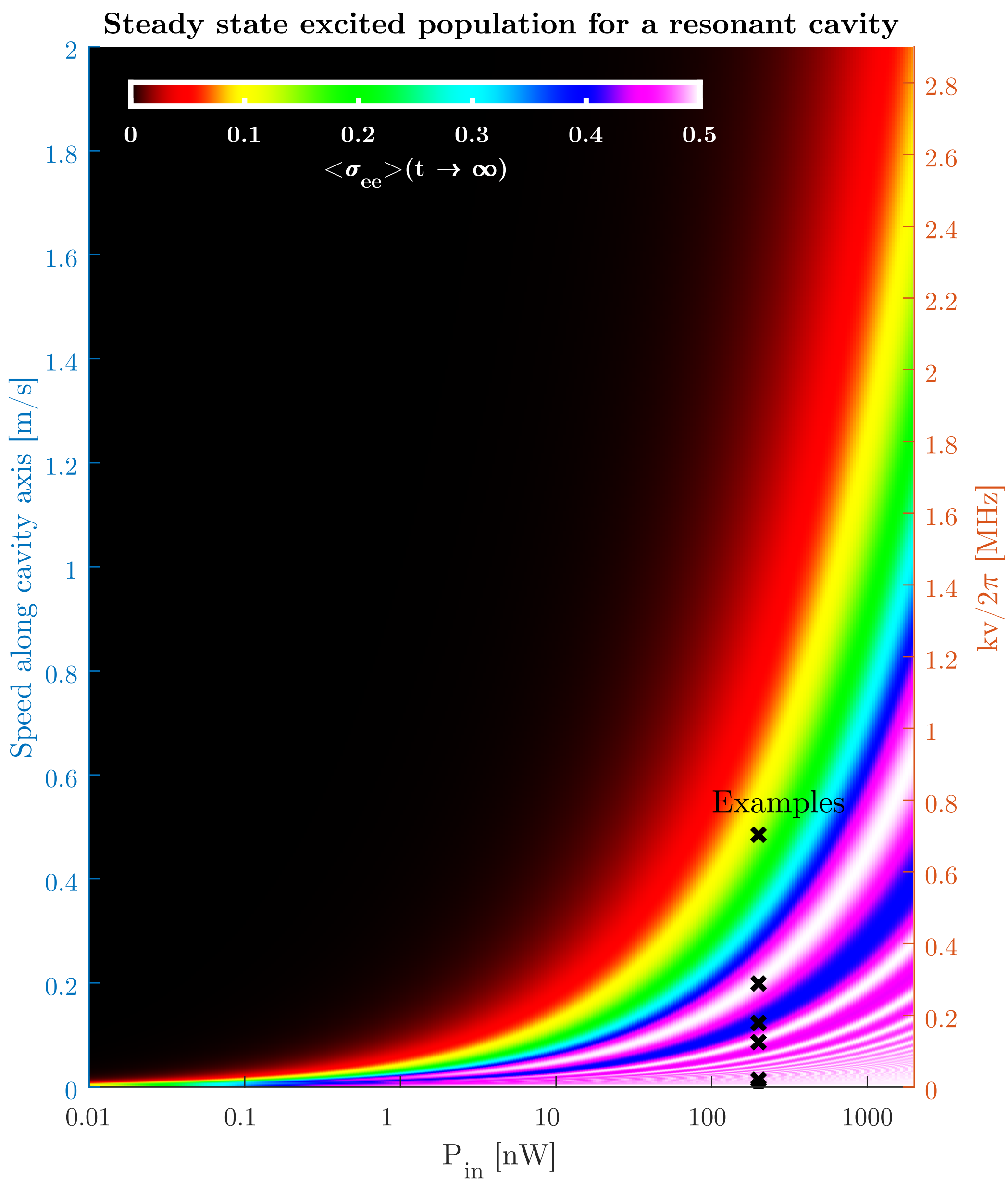

Figure 2.5: *Steady state excited population of an atom moving in a standing wave, resonant with the transition frequency, for a wide range of atomic speeds and cavity input powers. The examples refer to Fig. 2.3.*

2.4.2 An Atom Moving in a Detuned Cavity

If the cavity and driving laser are detuned from the atomic transition, the population dynamics change significantly. For example, an atom standing still now undergoes detuned, damped Rabi oscillations, so the steady state excitation probability will be below 0.5. The population dynamics and velocity-dependence of $\langle\sigma_{ee}\rangle_S$ can be seen in Fig. 2.6. An important result is that the cavity detuning causes a dip in the excitation probability for slow-moving atoms, which interact less with the cavity mode. However, for some velocities the movement along the varying electric field combined with the generalized Rabi frequency of the oscillations conspire to keep $\langle\sigma_{ee}\rangle$ oscillating near 0.5. For example a very sharp resonance feature is prominent around v = 238 mm/s: Initially, the dynamics are similar to nearby velocities, such as the 275 mm/s example, but on longer timescales, a slow dynamic becomes clear. The dynamics for v = 646 mm/s, where the Doppler shift is approximately the cavity detuning, are also very similar to the v = 0 example of Fig. 2.3. For v = 646 mm/s, the atom is on resonance with one of the traveling wave components, and interacts only weakly with the other component, leading to dynamics that resemble regular Rabi oscillations, but with minor differences due to the wave mixing. For higher velocities, the dynamics are similar to regular, detuned Rabi oscillations, with one component of the traveling wave near resonance, and the other now far-detuned.

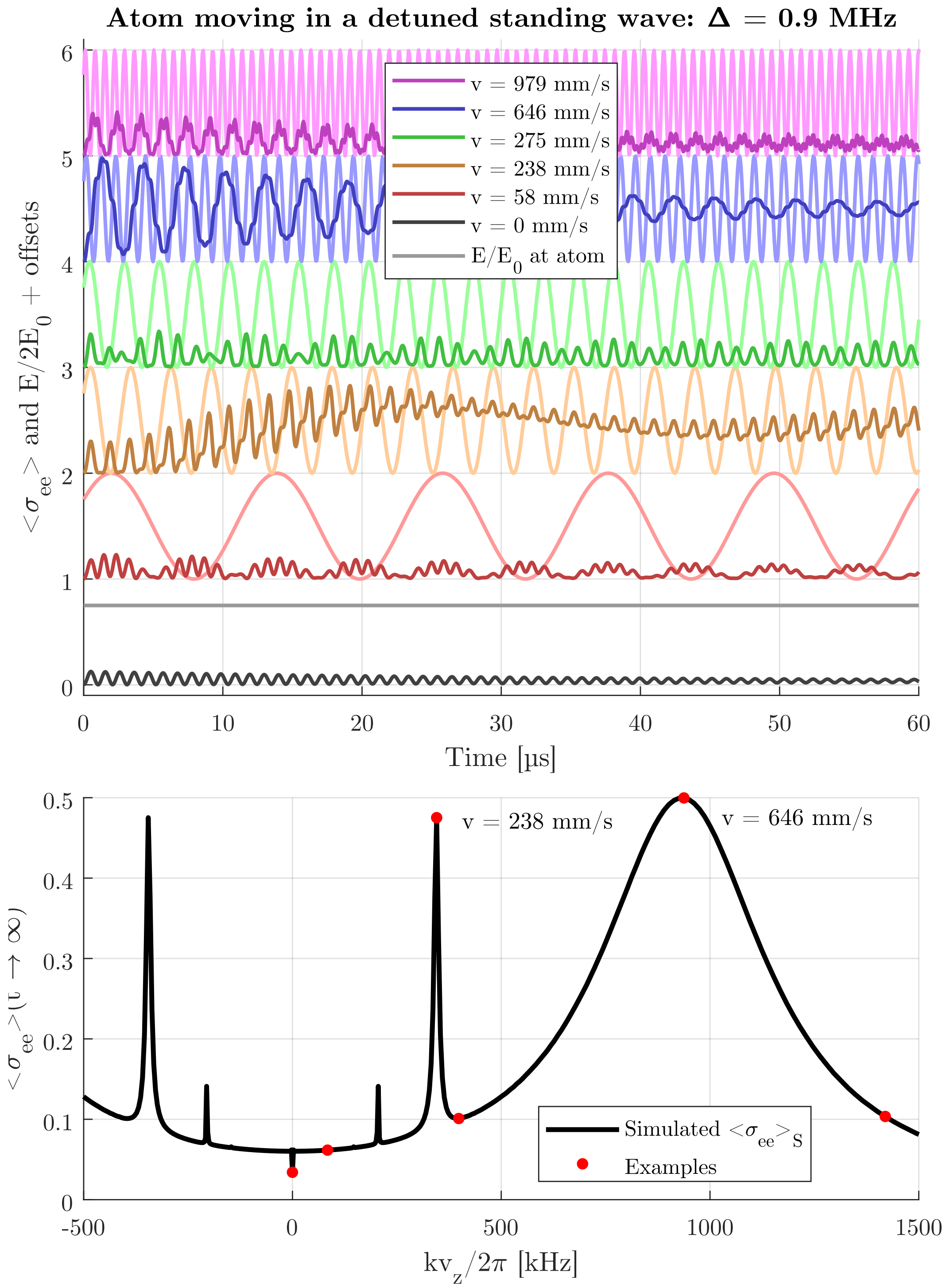

Figure 2.6: *In the upper figure, the dynamics of the atomic excited population is shown for atoms with different velocities in a cavity detuned by* $\Delta = 2\pi \cdot 0.9$ *MHz wrt. the atomic resonance. The cavity is driven by a* P_{in} *= 200 nW laser on resonance with the cavity. The lower figure shows how* $\langle \sigma_{ee} \rangle_S$ *depends on the velocity along the cavity axis. Note the* $v = 0$ *case is sensitive to the location of the atom.*

The influence of cavity field power on the population dynamics is investigated in Fig. 2.7. In the case of a detuned cavity, we see that for low power, $\langle \sigma_{ee} \rangle_S$ is only non-zero for velocities that correspond to a Doppler shift equal to the cavity detuning. This makes sense, as the atom effectively couples to only the resonant traveling wave component, the other being too far detuned compared to the power broadening to interact with the atom. For increasing power, the range of atomic velocities that can interact with the field increases, until both the traveling wave components are within range of certain velocities. At this point the effects of the waves mixing begins to become prominent, with new resonances appearing, similarly to the resonant cavity case.

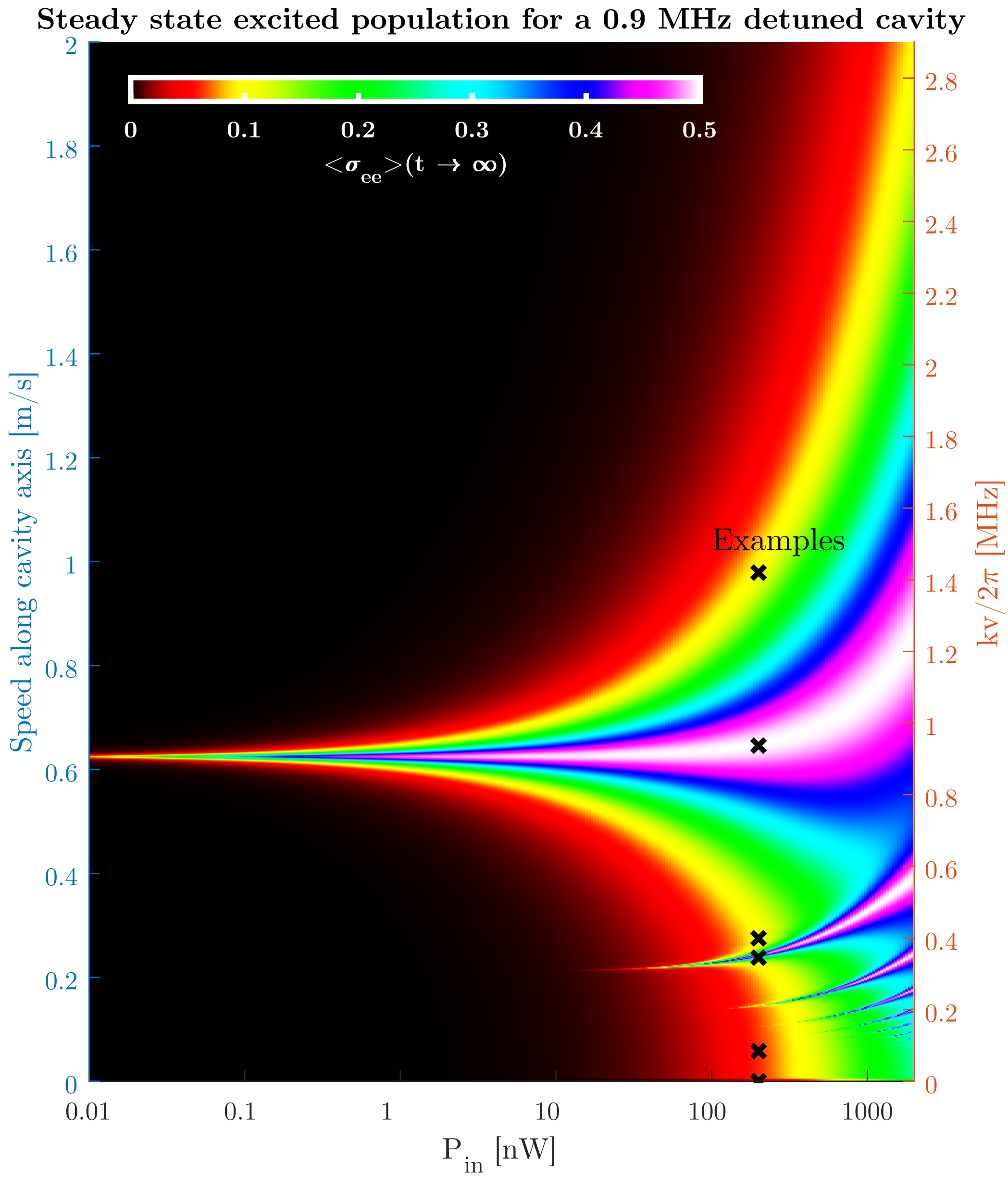

Figure 2.7: *Steady state excitation probability of an atom moving in a standing wave, detuned from the transition frequency, for a wide range of atomic speeds and cavity input powers. The examples refer to Fig. 2.6.*

2.4.3 Particle Interpretation

The results found in section 2.4.1 and 2.4.2 can also be interpreted in terms of multi-photon processes. These have been studied analytically by A. Tallet [12], who found similar population dynamics for two-level atoms moving in two opposite-traveling pump fields. The first order (d=1) process is illustrated in 2.8 - for the d'th order, d photons are absorbed from one direction, and d-1 emitted in the opposite direction. The outer peaks in Fig. 2.3 and 2.6 (lower) are single-photon resonances due to Rayleigh scattering, also called Bennett holes. As we move towards lower Doppler shifts on the figures, we encounter the first order doppleron resonance, e.g. at v = 238 mm/s in Fig. 2.6. The second order doppleron resonance is visible near v ≈ 180 mm/s in Fig. 2.7. The higher the order, the less likely the process is to happen for a given power.

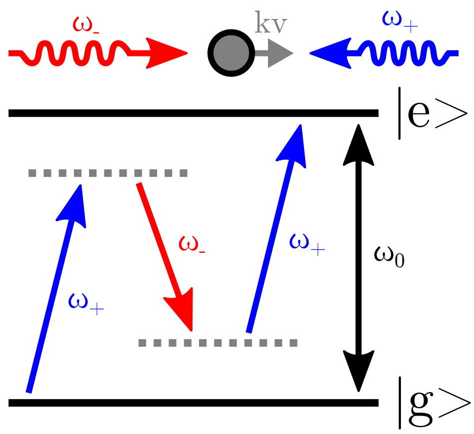

Figure 2.8: *Illustration of a first order doppleron resonance. The atom absorbs two blueshifted photons from the left-propagating mode and emits a redshifted photon into the right-propagating mode, completing a transition from ground to excited state.*

2.4.4 Characterizing the Resonances

On Fig. 2.5 and 2.7 we see the Bennett holes and doppleron resonances diverge for increasing power. Here we should remember that the bare states $|e\rangle$ and $|g\rangle$ are not eigenstates of the Hamiltonian - the eigenstates are dressed states (illustrated in Fig. 2.9), and their interaction picture energies are not split by the detuning Δ, but by the generalized Rabi frequency, $\Omega = \sqrt{\chi^2 + \Delta^2}$. Since g and thus χ varies in time as the atom moves, we may expect the resonance velocities to scale with $\sqrt{\alpha\chi_m^2 + \Delta^2}$, with χ_m being the mean value. To investigate the Doppleron resonance condition of the simulations we first calculate χ_m by averaging over the absolute value of the sine and using the relation for the intra-cavity photon number of section 2.3:

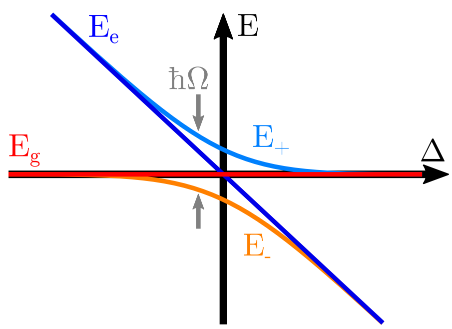

Figure 2.9: *Illustration of the dressed states of an atom: The eigenstate energies E_+ and E_- of the interaction picture Hamiltonian are split by Ω rather than Δ.*

$$\chi_m(P_{in}) = 2g_0\sqrt{n}\,\langle \sin(kz)\rangle = \frac{4g_0}{\pi}\sqrt{\frac{P_{in}}{\hbar\omega_e\kappa}} \tag{2.22}$$

Where $g_0 = \sqrt{6c^3\Gamma_{eg}\omega_e/W_e^2 L\omega_{ae}^3}$. This is used to define the following function with a fitted parameter α:

$$kv_d(P_{in}) = \frac{\sqrt{\alpha\chi_m^2 + \Delta^2}}{2d+1} \tag{2.23}$$

This function is based on the Doppleron resonance condition found by A. Tallet, however he found a single value for α [12, p. 1338].

The function is fitted to each of the Bennett hole and doppleron peaks of Fig. 2.5 and 2.7. Examples of fits to the Bennett holes and first to fourth order dopplerons are shown in Fig. 2.10 for the resonant cavity. According to the fits, α varies with both the doppleron order and cavity detuning - see Table 2.1.

d	α ($\Delta = 0$)	α ($\Delta = 0.9$ MHz)
0	0.4267 ± 0.0002	0.3485 ± 0.0008
1	0.7290 ± 0.0006	1.155 ± 0.008
2	0.825 ± 0.002	1.185 ± 0.004
3	0.868 ± 0.003	1.171 ± 0.004
4	0.891 ± 0.005	1.150 ± 0.004

Table 2.1: *Fit values for α, depending on the Doppleron order d (0 for Bennett holes) and cavity detuning Δ.*

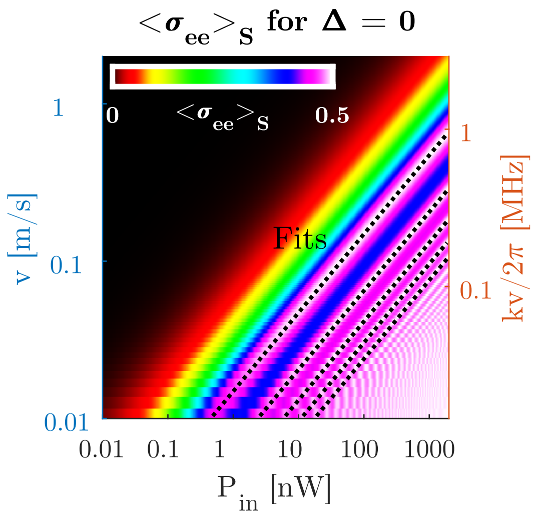

Figure 2.10: *$\langle\sigma_{ee}\rangle_S$ for a resonant cavity, with double-logarithmic axes, illustrating how both the locations and widths in kv-space of the Bennett hole and doppleron features scale with χ and $\sqrt{P_{in}}$. The dotted lines are fits.*

The Bennett hole resonance is useful for characterizing the range of velocities that will primarily participate in an interaction with the cavity field: For a cavity on resonance, $\langle\sigma_{ee}\rangle_S$ is highest for kv equal to or lower than the Bennett hole resonance, and decreases monotonically for higher speeds. For a detuned cavity, $\langle\sigma_{ee}\rangle_S$ is highest for speeds corresponding to the resonance, and is also decreasing for higher speeds. Since the resonances scale with the Rabi frequency and cavity detuning in quadrature, the Bennett hole is very close to the cavity detuning for a wide range of powers and does not begin to diverge before $\chi \approx \Delta$. This is significantly different from the case of a resonant cavity, where the Bennett hole resonance shifts even at low power.

CHAPTER 3

Dynamics of the Cold Strontium Ensemble

In the previous chapter, the physics of the cavity and its interaction with individual atoms was analyzed. However, in our experiments, the cavity is populated by millions of atoms with thermal velocities. The aim of this chapter is to extend the model to describe the dynamics of the full ensemble.

3.1 Including the Pump Pulse and a Thermal Ensemble

In our experiment, we excite the atomic ensemble with a pump pulse laser. This is a powerful laser ($P_p \approx 100$ mW) which does not drive any cavity, so we can neglect the dynamics of the pulse photons and implement a semiclassical dipole interaction term [11, p. 153-154]:

$$H_{ip} = \hbar \frac{\chi_p}{2} \left(\sigma_{ge} + \sigma_{eg}\right) \left(e^{ik_p r - i\omega_p t} + e^{-ik_p r + i\omega_p t}\right) \tag{3.1}$$

The dynamics of the new system is governed by H_{ip} plus the Hamiltonian of Eq. 2.15, and turning on the pulse laser gives rise to Rabi oscillations between state $|g\rangle$ and $|e\rangle$. The Rabi frequency is modelled with a Gaussian beam profile:

$$\chi_p = \overbrace{\sqrt{\frac{12c^2\Gamma_{eg}P_p(t)}{\hbar\omega_{ae}^3 W_{py} W_{pxz}}}}^{\text{Bare frequency}} \cdot \overbrace{\exp\left(-\frac{y^2}{W_{py}^2} - \frac{(x-z)^2}{W_{pxz}^2}\right)}^{\text{Beam profile}} \cdot \overbrace{\frac{4(y-y_{MOT})^2}{4(y-y_{MOT})^2 + x^2 + z^2}}^{\text{Magnetic field influence}} \tag{3.2}$$

Where P_p is the beam power, W_{py} and W_{pxz} are the waist radii of the beam along the y axis and in the xz-plane, respectively. The pulse beam propagation direction has an angle of $\approx 45°$ wrt. the cavity axis and lies in the xz-plane. The rightmost term in Eq. 3.2 stems from the anti-Helmholtz magnetic field of the MOT coils, and y_{MOT} is the center of the field along the y axis (this is elaborated in Section 3.2.7)[1]. A second model will also be used, which allows for rotated elliptical beam profiles:

$$\chi_p = \sqrt{\frac{12c^2\Gamma_{eg}P_p(t)}{\hbar\omega_{ae}^3 W_{p1} W_{p2}}} \cdot e^{-Ay^2 - B(x-z)^2 - Cy(x-z)} \cdot \frac{4(y-y_{MOT})^2)}{4(y-y_{MOT})^2 + x^2 + z^2} \tag{3.3}$$

Here W_{p1} and W_{p2} are the waist radii of the beam along its minor and major axes, and A, B and C are fit parameters to experimental beam profiler data, which will be determined later.

[1] Due to a code error, x and y were switched in this equation for simulations in Section 3.2 and some in 3.3 - however the effects on the results are negligible, except for Section 3.2.7, where the error has been fixed. For an estimate of the error, see Appendix A.1.

To account for the thermal ensemble of atoms, the Hamiltonian of Eq. 2.15 must be extended to include terms for each atom - this extension to N atoms interacting with a common radiation mode is known as the Tavis-Cummings model. Solving the dynamics of such a system would require a lot of computer power for an ensemble with millions of atoms, so the ensemble is approximated with N_g atomic groups. Each group contains $N_{pg} = N/N_g$ atoms, which all share the same position, velocity and other variables, rather than being treated independently. For sufficiently[2] small group sizes, the simulated dynamics approach the dynamics of the system where each atom is treated independently. The full Hamiltonian of the system in the Schrödinger picture is given by:

$$\begin{aligned} H &= \hbar\omega_e a^\dagger a + \sum_{i=1}^{N_g} \hbar\omega_{ae} N_{pg}\sigma_{ee}^i + \sum_{i=1}^{N_g} N_{pg}\hbar\omega_{ac}\sigma_{cc}^i \\ &+ \frac{1}{2}\hbar\eta\left(ae^{-i\omega_s t} + a^\dagger e^{i\omega_s t}\right) + \sum_{i=1}^{N_g} g_i N_{pg}\left(\sigma_{ge}^i + \sigma_{eg}^i\right)\left(a + a^\dagger\right) \\ &+ \sum_{i=1}^{N_g} \hbar\frac{\chi_p}{2} N_{pg}\left(\sigma_{ge}^i + \sigma_{eg}^i\right)\left(e^{i\vec{k_p}\cdot\vec{r_i} - i\omega_p t} + e^{-i\vec{k_p}\cdot\vec{r_i} + i\omega_p t}\right) \end{aligned} \tag{3.4}$$

Entering an interaction picture with respect to $H_0 = \hbar\omega_p a^\dagger a + \sum_{i=1}^{N_g}\hbar\omega_p N_{pg}\sigma_{ee}^i + \sum_{i=1}^{N_g} N_{pg}\hbar\omega_{ac}\sigma_{cc}^i$, using the RWA and factorizing the expectation values, we obtain the equations governing the time evolution of the system when the MOT lasers are off:

$$\begin{aligned} \langle\dot{a}\rangle &= -\frac{i}{2}\eta e^{i\Delta_{sp}t} - \left(i\Delta_{ep} + \frac{\kappa}{2}\right)\langle a\rangle - \sum_{i=1}^{N_g} i g_i N_{pg}\left\langle\sigma_{ge}^i\right\rangle \\ \left\langle\dot{\sigma_{ge}^i}\right\rangle &= \left(i\Delta_{ap} - \frac{\Gamma}{2}\right)\left\langle\sigma_{ge}^i\right\rangle + i\left(g_i\langle a\rangle + \frac{\chi_p^i}{2}e^{-i\vec{k_p}\cdot\vec{r_i}}\right)\left(\left\langle\sigma_{ee}^i\right\rangle - \left\langle\sigma_{gg}^i\right\rangle\right) \\ \left\langle\dot{\sigma_{ee}^i}\right\rangle &= -\Gamma\left\langle\sigma_{ee}^i\right\rangle + \sum_{i=1}^{N_g} i\left(g_i\left\langle a^\dagger\right\rangle + \frac{\chi_p^i}{2}e^{i\vec{k_p}\cdot\vec{r_i}}\right)\left\langle\sigma_{ge}^i\right\rangle \\ &- \sum_{i=1}^{N_g} i\left(g_i\langle a\rangle + \frac{\chi_p^i}{2}e^{-i\vec{k_p}\cdot\vec{r_i}}\right)\left\langle\sigma_{eg}^i\right\rangle \end{aligned} \tag{3.5}$$

Here we have introduced detunings with respect to the pump pulse frequency: For example $\Delta_{sp} = \Delta_s - \Delta_p$ for the seed laser with respect to the pump pulse, and similarly for the atoms Δ_{ap} and cavity mode Δ_{ep}.

The atomic motion is treated classically, assuming the atoms move with constant, thermal velocities at a temperature T. The initial positions of the ensemble are randomly distributed assuming the MOT density distribution is Gaussian, with a parameter R denoting the standard deviation of the density profile (see Fig. 3.1).

[2] We will investigate what constitutes sufficiently small in Section 3.3.1.

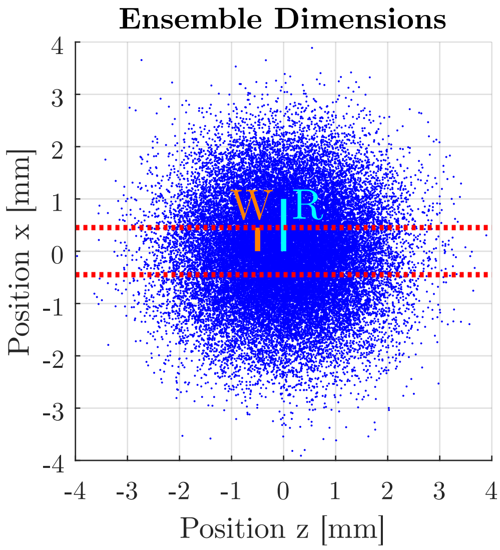

Figure 3.1: *Gaussian distributed positions in a simulation with N_g = 35,000 atom groups. Each group is shown as a blue dot and represents N_{pg} = 2,000 atoms. $R \approx 1$ mm is the standard deviation of the density distribution, and $W = 0.45$ mm is the cavity waist radius.*

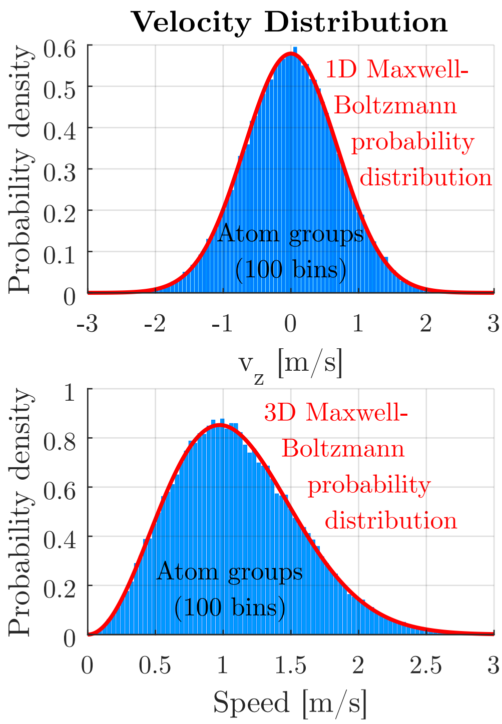

Figure 3.2: *Boltzmann-distributed velocities in a simulation with T = 5 mK and 70,000 atom groups.*

3.2 Dynamics of the Pump Pulse Interaction

In this section we investigate the dynamics of the interaction between the ensemble and the pump pulse. We assume there is no seed laser driving the cavity, and that the cavity is on resonance with the atoms. The objective of the pump laser is to create a large inversion in the part of the ensemble overlapping with the cavity mode, so that many atoms start lasing on the ${}^1S_0$ - ${}^3P_1$ transition, and we can obtain a large cavity output signal. A single atom can be transferred from the ground to excited state with a π pulse on resonance, with a duration $t_\pi = \pi/\chi_p$, but since we have an ensemble of thermal atoms, each atom may experience a different Rabi frequency χ_p^i. Furthermore, due to the thermal velocities, the atoms will experience different Doppler shifts with respect to the pulse frequency, and oscillate with the generalized Rabi frequency. Based on this, we define the pulse duration that excites the highest fraction of the ensemble as t_π^{ens}, and of the cavity mode, t_π^W. To create a large inversion, the experimental task is to make sure that the atoms oscillate with as similar Rabi frequencies and Doppler shifts as possible, and are excited on a timescale much shorter than the decay time $1/\Gamma = 21\ \mu s$ to avoid decays back to the ground state.

To obtain a uniform distribution of Rabi frequencies the intensity distribution should be uniform, so the pump pulse should have as large a waist as possible. To avoid decoherence, we also want to obtain a uniform distribution of generalized Rabi frequencies, $\Omega_p^i = \sqrt{(\chi_p^i)^2 + \Delta_i^2}$, which leads to the condition $\chi_p^i \gg \Delta_i$. This means we want to minimize the temperature of the atoms, so the Doppler shifts due to the thermal velocities become more uniform, and we want a pulse beam with high intensity, which requires small waists. Thus the beam waist size is a parameter that must be optimized, to balance the requirement for high but uniform intensity. If we have good knowledge of experimental parameters and our model is accurate, the model can predict the optimal pulse waists. To compare the influence of the different parameters on the ensemble dynamics during the pump pulse, we run simulations using parameters expected to be close to the experimental values (how to determine the parameters will be shown later), varying one at a time. The standard parameters used in Section 3.2 are given in Table 3.1.

Parameter	Symbol	Standard value
Pump pulse power	P_p	100 mW
Temperature	T	5 mK
Ensemble size	R	1 mm
Pulse waist	W_{xz}, W_y	2.5 mm
Magnetic field offset	y_{MOT}	4 mm

Table 3.1: *Standard parameters for investigating the ensemble dynamics during the pump pulse.*

3.2.1 The Pump Pulse Power

The higher the pump pulse power, the faster the Rabi oscillations will be for each atom in the ensemble, and the shorter the optimal pump pulse will be. Furthermore, power broadening will be stronger, so the pump pulse will interact strongly with a broader range of velocities along its axis, which means a larger fraction of the ensemble can be pumped to the excited state. The dynamics for the whole ensemble can be seen in Fig. 3.3.

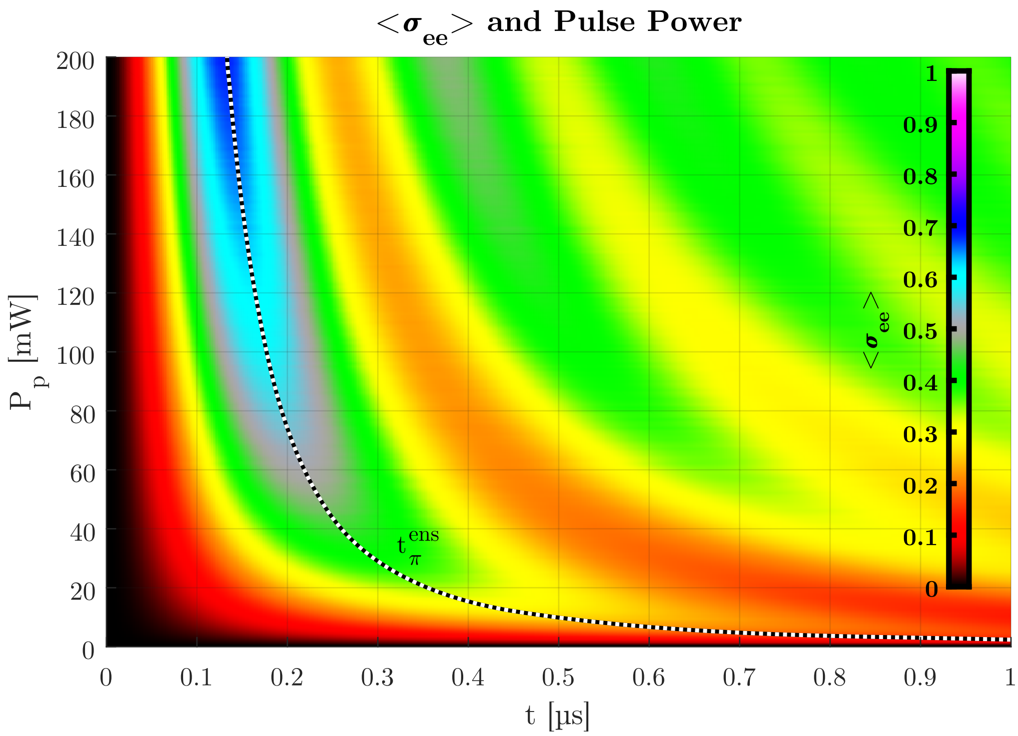

Figure 3.3: *Population dynamics for the ensemble for various pump pulse powers, after the pump pulse is turned on at $t = 0$. The higher the power, the higher excited population can be achieved. The duration t_π^{ens} is also shown: Here the excited population in the ensemble is highest for a given power.*

Since we are primarily interested in the atoms within the cavity mode, we also investigate the dynamics of the atoms located within the cavity waist: $\langle\sigma_{ee}\rangle_W$ defines the fractional excited population of this sub-ensemble. During a pump pulse, $\langle\sigma_{ee}\rangle_W$ reaches higher values and oscillates more strongly than $\langle\sigma_{ee}\rangle$. This is because of the cylinder-shape of this sub-ensemble (recall Fig. 3.1), which leads to a more uniform and generally higher intensity at these atoms compared to the whole ensemble. The dynamics for the atoms within the cavity waist can be seen in Fig. 3.4. Here the pulse durations t_π^{ens} and t_π^W are compared for both the whole ensemble and the cavity atoms: We see that the optimal pulse for exciting the most atoms in the cavity mode t_π^W is generally shorter than for maximally exciting the whole ensemble. This is again because the cavity atoms generally experience a more intense field, and therefore oscillate with higher Rabi frequencies. Furthermore, we see that for these parameters, at least about 30 mW of pump pulse power is required to excite more than 50 % of the atoms in the cavity waist. This should be the threshold (inversion) for the atoms to be able to lase within the cavity without any driving laser, as absorption would otherwise dominate over stimulated emission.

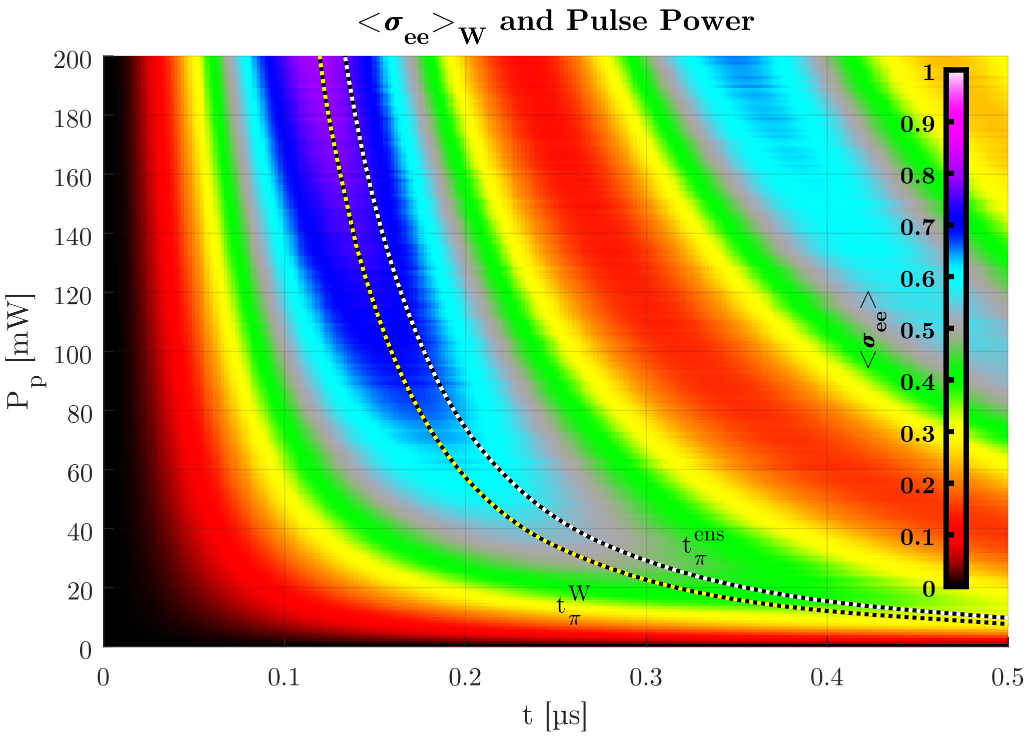

Figure 3.4: *Population dynamics within the cavity waist for various pump pulse powers. The pulse duration t_π^W (yellow and black) is generally shorter than t_π^{ens} (white and black). Note the time axis has a shorter span than in Fig. 3.3 to show the initial Rabi oscillation in greater detail.*

3.2.2 The Temperature

For lower temperatures, the atoms move with more uniform velocities, lowering the Doppler detunings Δ_i with respect to the pump pulse, so their generalized Rabi frequencies Ω_p^i approach χ_p^i for a resonant pump laser. At zero temperature, the variations in Ω_p^i are limited only by the pulse waist, and for a sufficiently large waist, the fractional excited population of the ensemble can approach 1. The temperature-dependence of the population dynamics are shown in Fig. 3.5 for the ensemble, and Fig. 3.6 for the population within the cavity waist. Because the generalized Rabi frequencies are lowered at lower temperatures, t_π^{ens} and t_π^W increase slightly for the lowest temperatures.

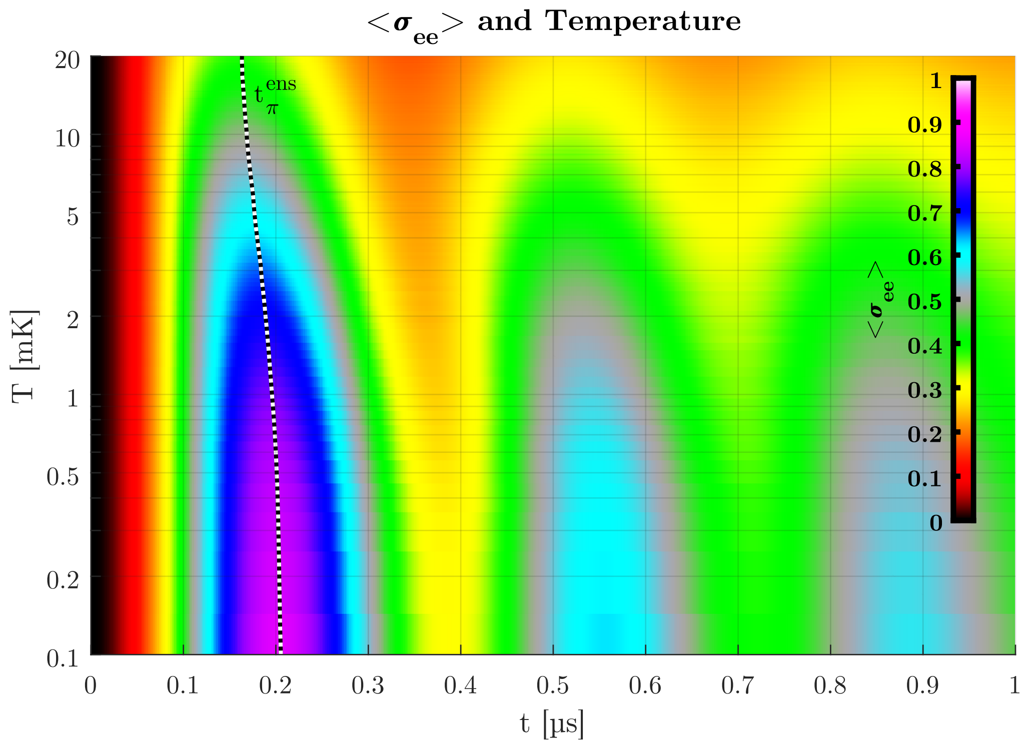

Figure 3.5: *Population dynamics for the ensemble for various temperatures. The lower the temperature, the higher excited population can be achieved.*

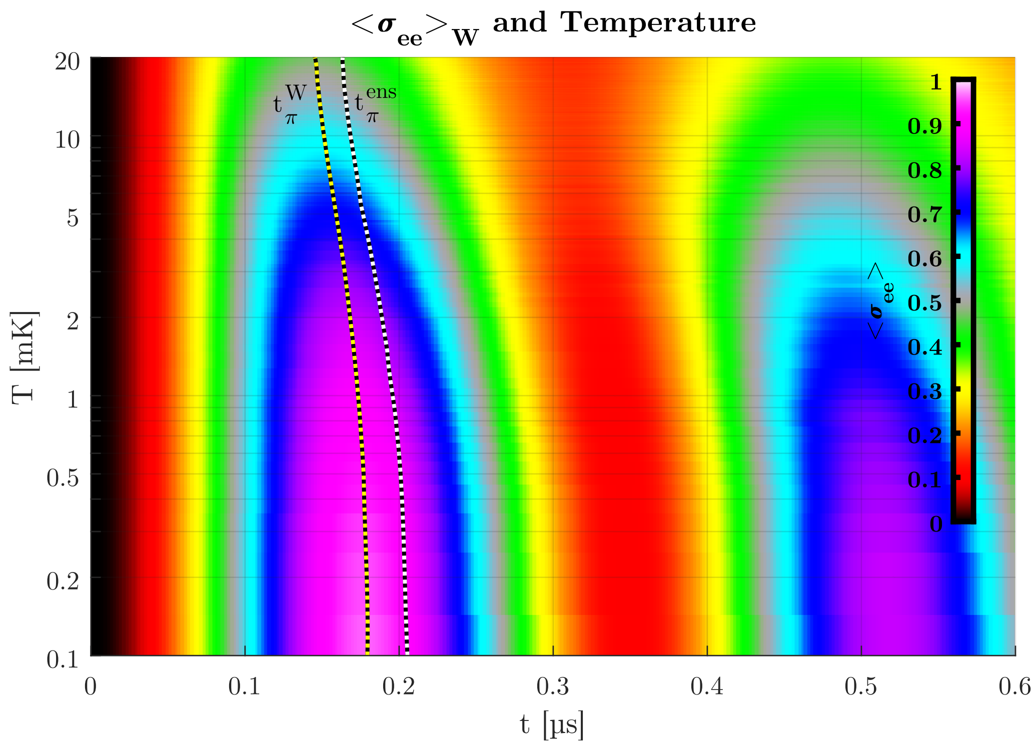

Figure 3.6: *Population dynamics within the cavity waist for various temperatures. For below about 1 mK, parameters other than temperature, such as the beam profile, become significant limiting factors for the achievable excited population.*

3.2.3 Seed Laser Power

Depending on the seed laser power, there will be an intra-cavity field which drives the ensemble between the ground and excited state, primarily within the cavity waist. For most experiments with the seed laser on, the atoms within the cavity waist will reach an equilibrium with the seed laser, which may take about 5-30 microseconds, depending on the power. The Rabi oscillations driven by the seed laser will no longer be coherent when the pump pulse is applied, and the seed laser just causes a certain, approximately constant, excited population with a spatial dependence. When the pump pulse interacts with the intra-cavity atoms, it will drive the excited atoms to the ground state, so the excited population will be lower for higher seed laser powers. The effect on the atoms within the cavity waist is shown in Fig. 3.7 - for the highest experimental powers, 15 % of the intra-cavity atoms will have been excited by the seed laser once the pump pulse is applied, and the obtainable $\langle \sigma_{ee}^{W} \rangle$ is reduced from 71 % to 60 % in this example simulation. Here atoms were given 30 μs to reach a steady state with the cavity field before the pump pulse was applied. The effect on the population dynamics when looking at the full ensemble is less than 2 %, making it hard to detect experimentally from e.g. fluorescence measurements.

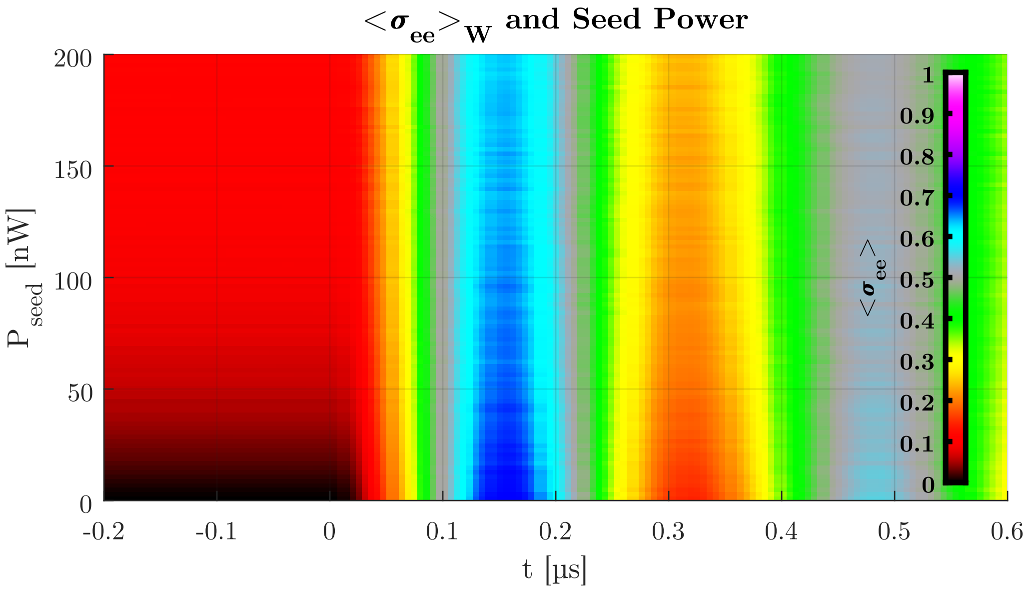

Figure 3.7: *Population dynamics for the atoms within the cavity waist for various seed laser powers. The pump pulse is turned on at t = 0. High seed laser power reduces the obtainable fractional excited population within the cavity waist.*

3.2.4 The Ensemble Density Profile

The more compact the ensemble is, the larger a fraction can be excited: the atoms experience a more uniform distribution of power from the pump pulse, reducing the spread in χ_p^i. The effect of varying the ensemble density profile parameter R is shown on Fig. 3.8, and the effect on the cavity waist population in Fig. 3.9. For ensemble sizes smaller than the cavity waist, the distinction becomes unnecessary as most atoms are located within the waist. $\langle \sigma_{ee}^{W} \rangle$ is less sensitive to the scaling of R than $\langle \sigma_{ee} \rangle$ is, as the expansion along two dimensions for increasing R is cut off by looking at the intra-waist population. For the smallest ensemble sizes ($R \ll W_p$), the temperature becomes the main limiting factor in approaching $\langle \sigma_{ee} \rangle = 1$. Another notable effect of a smaller ensemble is that the Rabi oscillations of the whole ensemble become more pronounced: Both the maxima and minima in $\langle \sigma_{ee} \rangle$ vary more in amplitude.

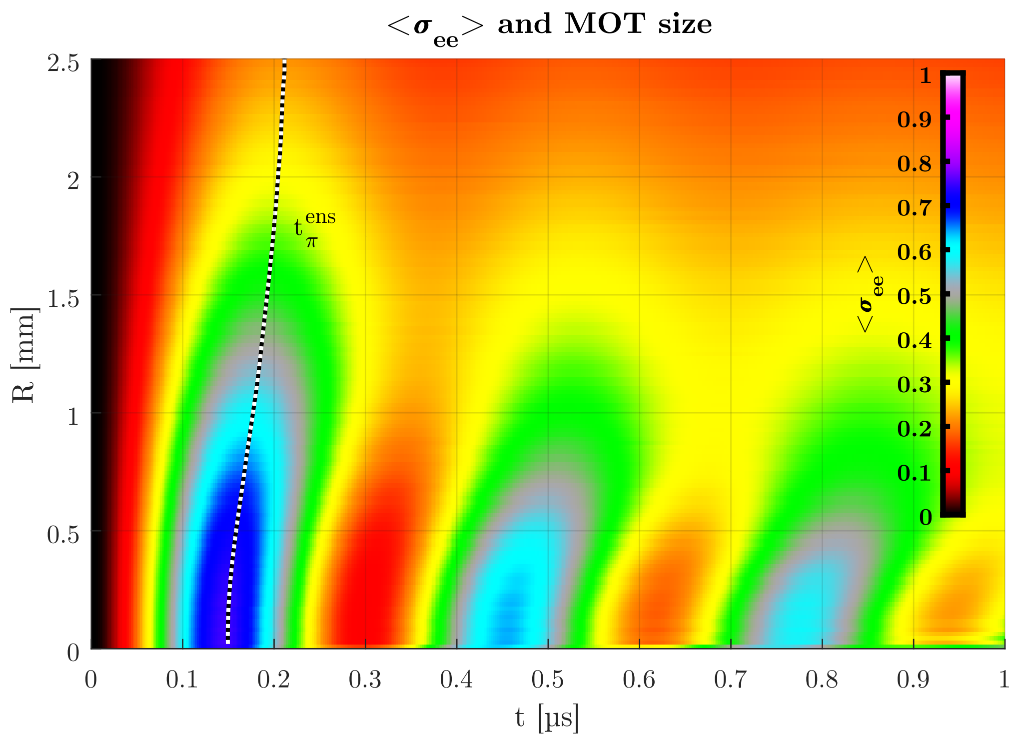

Figure 3.8: *Population dynamics for various ensemble density parameters R. The smaller and denser the ensemble is, the higher excited population can be achieved, until $R \ll W_p$, where the temperature becomes the main limiting factor.*

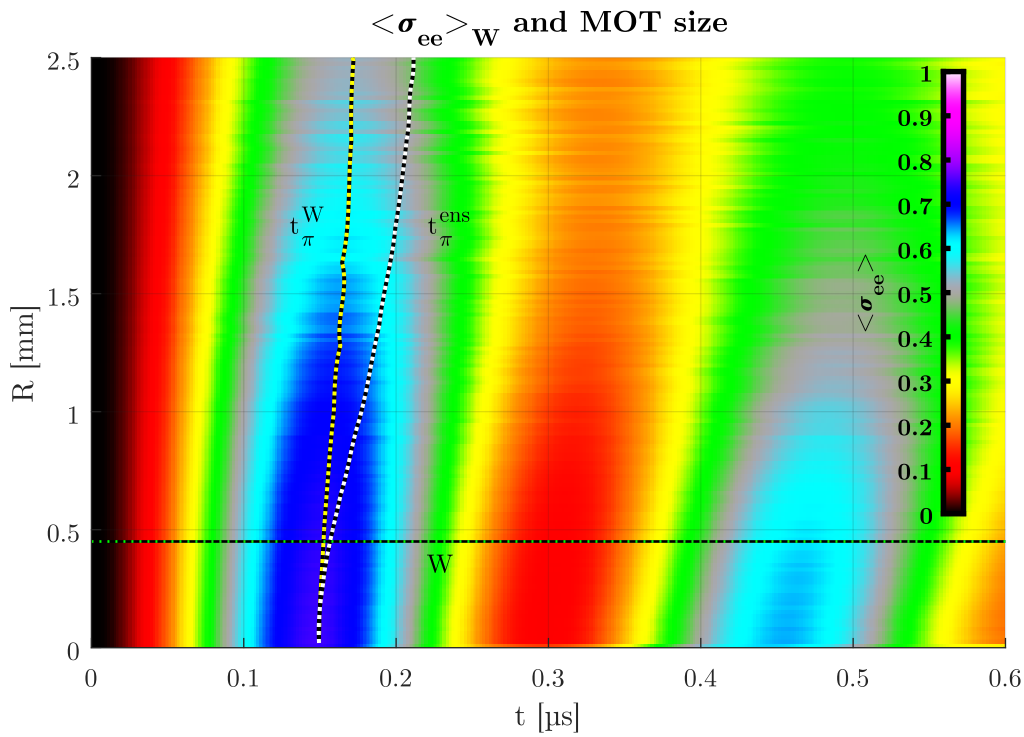

Figure 3.9: *Population dynamics for atoms within the cavity waist for various ensemble sizes. As $R \to W$, the distinction between ensemble population and the population within the waist becomes unnecessary.*

3.2.5 The Pump Pulse Waists

Enlarging the pulse waists have a similar effect to having a smaller ensemble: The spread in χ_p^i becomes smaller for the atoms in the ensemble, so higher $\langle\sigma_{ee}\rangle$ become possible. However, enlarging the waists means the intensity is also lowered for all atoms, so χ_p^i is lower, and Δ_i becomes a relatively more dominant factor in the generalized Rabi frequency for a given temperature, which lowers the obtainable $\langle\sigma_{ee}\rangle$. These effects give rise to an optimum waist size, which can be seen in Fig. 3.10, showing the highest obtainable $\langle\sigma_{ee}\rangle$ for different waist sizes, and Fig. 3.11, showing the population dynamics while varying one waist size. As expected for a spherical ensemble, there is no reason to have different waists along the axes if one wants to maximally excite the ensemble - here having roughly equal waist sizes is most optimal.

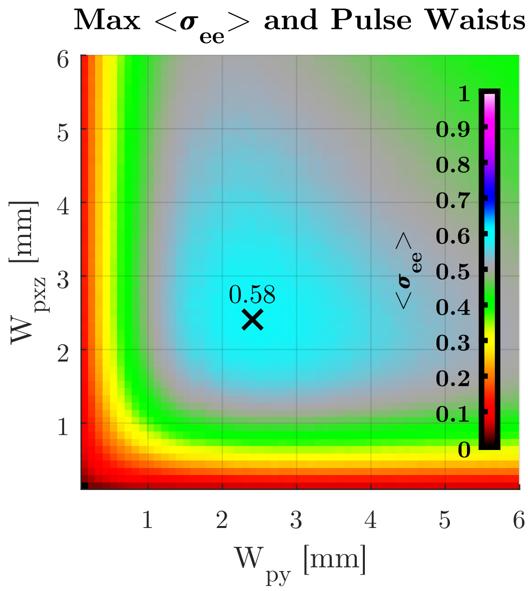

Figure 3.10: *Highest possible fractional excited population, depending on the pump pulse waist sizes along its axes. For these parameters, the peak is near W_p = 2.4 mm with $\langle\sigma_{ee}\rangle$ = 58 %.*

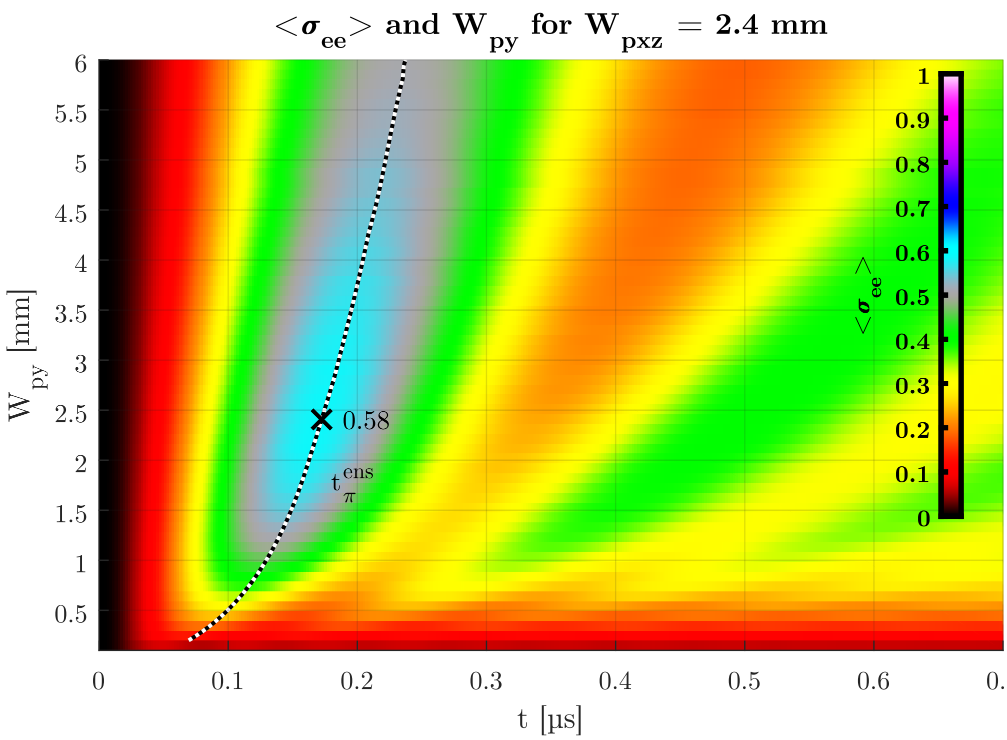

Figure 3.11: *Population dynamics for the ensemble for various pump waist sizes in the y dimension, for fixed xz-waist. The optimal waist sizes for exciting the ensemble are about 2.4 mm.*

For the population within the cavity waist there is a big difference between varying W_{pxz}, which aligns with the cavity axis, and W_{py}, which is perpendicular to it. The optimal waist dimensions for exciting atoms within the cavity mode is an elongated beam along the cavity plane with $W_{pxz} > W_{py}$: As seen in Fig. 3.12, the optimal dimensions are $W_{py} \approx 0.75$ mm and $W_{pxz} \approx 2.3$ mm, yielding $\langle \sigma_{ee}^{W} \rangle$ of up to 83 %. Due to the small waist size, the intensity and thus Rabi frequencies are very high. This leads to very short optimal pulse durations of 100 ns (see Fig. 3.13).

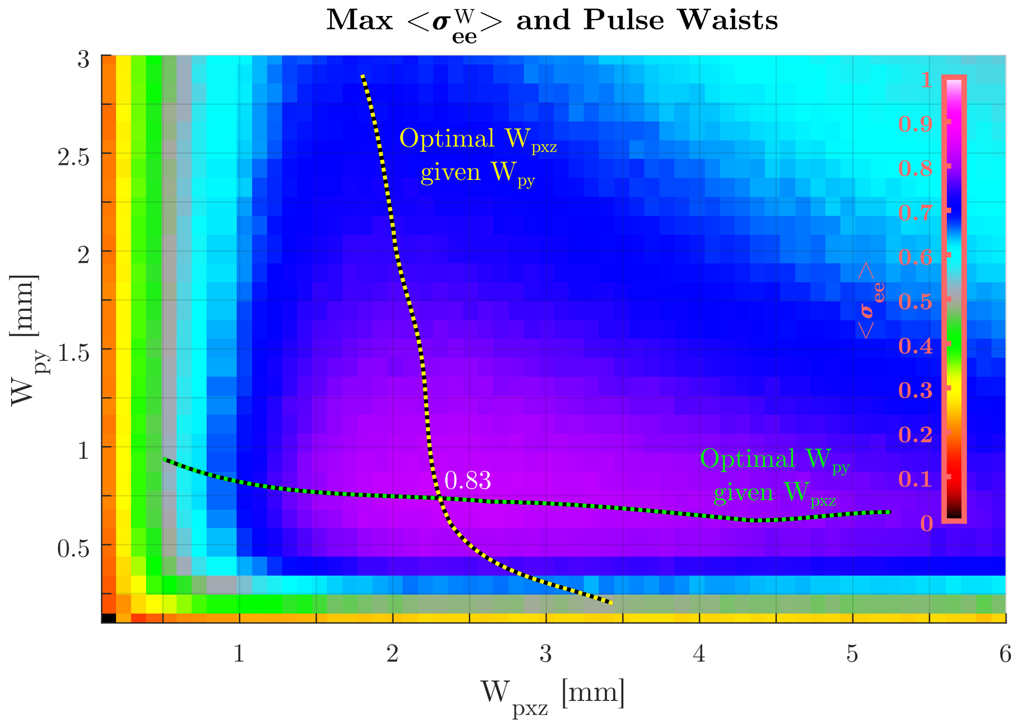

Figure 3.12: *Highest possible fractional excited population for atoms within the cavity waist, depending on the pump pulse waist sizes. The optimal pump pulse has $W_{py} \approx$ 2.3 mm and $W_{pxz} \approx$ 0.75 mm. Note the color scale is different from other figures.*

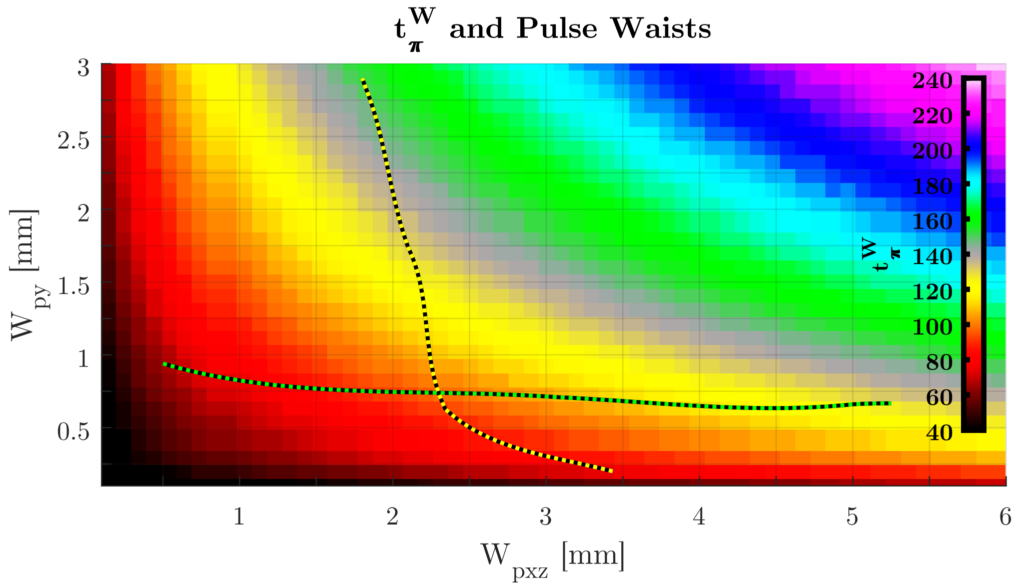

Figure 3.13: *Optimal pulse durations t_{π}^{W} for maximally exciting the atoms within the cavity waist, depending on the pump pulse waist sizes. The lines are the same as used in Fig. 3.12. For the optimal waist combination, t_{π}^{W} = 100 ns.*

3.2.6 Transient Pump Power Effects

To obtain the right frequency of the pump pulse light, the beam is sent through an acousto-optic modulator (AOM). This has a transient behavior which means the pump pulse power is not switched on and off instantly. To account for this, we modulate the pump pulse power in the simulation with a logistic opening and closing function as in Eq. 3.6.

$$P_p(t) = P_p^0 \cdot \frac{1}{1+\exp\left[(t_O - t)/\tau\right]} \cdot \frac{1}{1+\exp\left[-(t_C - t)/\tau\right]} \tag{3.6}$$

This represents the same dynamics as a hyperbolic tangent, just rewritten into a different mathematical form. Here τ is the characteristic timescale of the transient behavior, and we define t_O as the time when the power reaches half the value P_p^0 (the power if $\tau = 0$). Similarly t_C is the later time when the power falls to $P_p^0/2$. To see the consequences this can have for our experiment, we will consider an example: We want to maximally excite an ensemble with a 170 ns pulse. Depending on τ the pulse power will vary in time as seen in Fig. 3.14, and the population dynamics depending on τ can be seen in 3.15.

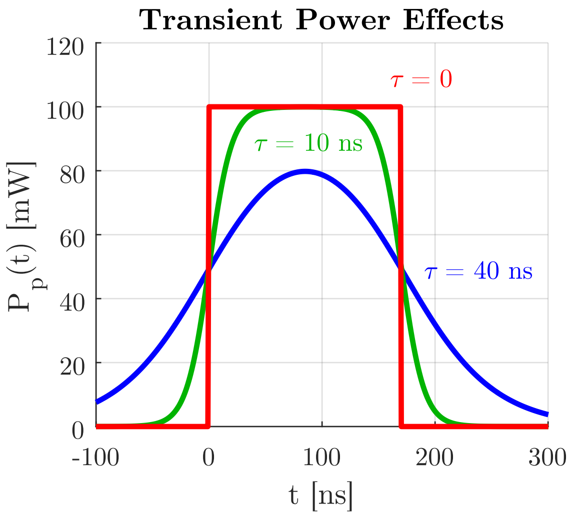

Figure 3.14: *The pump pulse does not turn on or off instantly, but has a transient behavior with a characteristic timescale τ.*

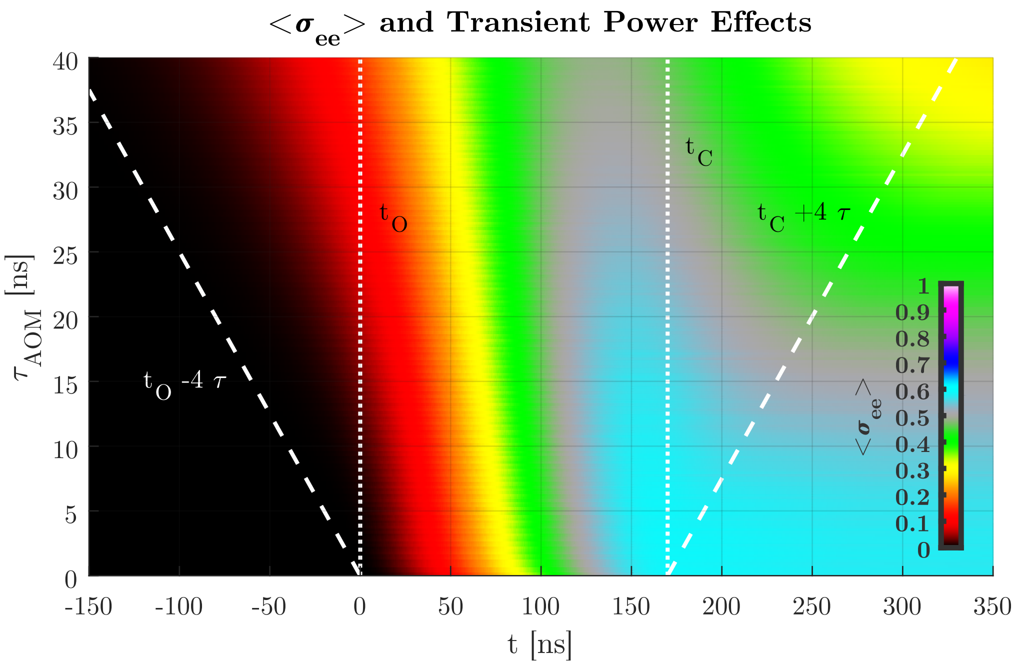

Figure 3.15: *Population dynamics depending on the transient timescale τ. The pump pulse is defined to last from t_O to t_C (170 ns), but the longer τ, the more slowly the pump pulse will turn on and off. This reduces the obtainable excited population.*

If $\tau > t_\pi^{ens}/10$, the peak power starts to drop below P_p^0. The area below one of the curves is the energy of the pump pulse, and this begins to increase once τ grows comparable to the pulse duration. Because of this the pulse duration must be decreased to compensate for the exponential tails of Eq. 3.6. As seen in Fig. 3.15, applying the 170 ns pulse with $\tau = 35$ ns will result in the ensemble being driven from 50 % excited at t = 150 ns almost down to 30 % at t = 300 ns due to light while the pulse is being turned off. An additional effect of a high τ is also that the Rabi frequencies will generally be lower during the interaction, which reduces the highest obtainable $\langle\sigma_{ee}\rangle$.

The transient effects become even more critical if we want to excite only the atoms within the cavity waist. For this, we found in Section 3.2.5 that the optimal pulse durations would be about 100 ns. There are two ways to solve this issue. The first is to use a 3π pulse of about 300 ns, however this leaves only slightly over 60 % of the cavity waist atoms excited, less than what can be achieved with a π-pulse optimized for the whole ensemble. The second and more viable option is to increase the waist sizes somewhat beyond the optimal values for $\tau = 0$ so the Rabi frequencies become lowered and longer pulses can be used. As seen on Fig. 3.12 and 3.14, one can for example still achieve about $\langle\sigma_{ee}^W\rangle = 0.75$ for $W_{py} = 1.2$ mm and $W_{pxz} = 3.4$ mm with a pulse duration of 130 ns. This also increases the excitation probability for atoms slightly outside the cavity waist which are not included when considering $\langle\sigma_{ee}^W\rangle$, but which may still have an influence on the lasing dynamics.

3.2.7 Location in the Magnetic Field

The MOT coils necessary for cooling the atoms form an anti-Helmholtz magnetic field which defines the quantization axis for the $^1S_0$ - $^3P_1$ $\Delta m = 0$ transition (see Fig. 3.16). The interaction strength depends on the projection of the electric field onto this quantization axis. Based on Maxwell's equation $\nabla \cdot \vec{B} = 0$ for the anti-Helmholtz configuration, a unit vector expression for the magnetic field can be found:

$$\hat{B} = \frac{1}{\sqrt{x^2 + 4y^2 + z^2}} \begin{pmatrix} -x \\ 2y \\ -z \end{pmatrix} \tag{3.7}$$

The light is polarized along the y axis, and given an intensity profile I, one can write:

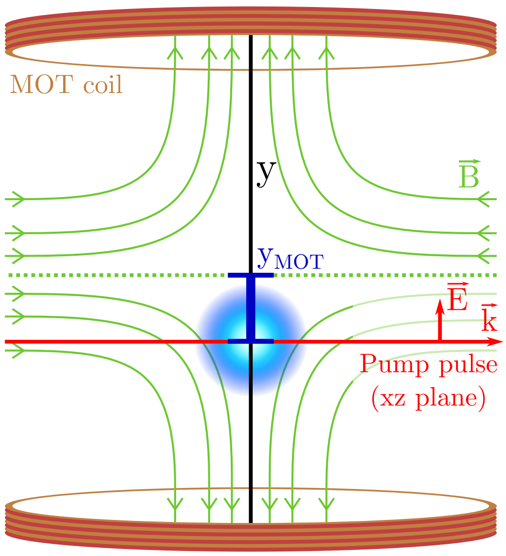

Figure 3.16: *Illustration of the anti-Helmholtz magnetic field and the ensemble displacement y_{MOT} with respect to it.*

$$\vec{E} \cdot \hat{B} = \sqrt{I} \cdot \frac{1}{\sqrt{x^2 + 4y^2 + z^2}} \cdot \begin{pmatrix} 0 \\ 1 \\ 0 \end{pmatrix} \cdot \begin{pmatrix} -x \\ 2y \\ -z \end{pmatrix} = \frac{2y\sqrt{I}}{x^2 + 4y^2 + z^2} \tag{3.8}$$

By taking the square of Eq. 3.8 one then finds that the effective intensity driving the $\Delta m = 0$ transition is the actual intensity multiplied by $4y^2/(x^2 + 4y^2 + z^2)$. This factor reduces the interaction strength and χ_p^i for the atoms near the center of the magnetic field, and reduces the maximum excited population that can be achieved. The effect on the ensemble can be seen in Fig. 3.17 and on the population within the cavity waist in Fig. 3.18.

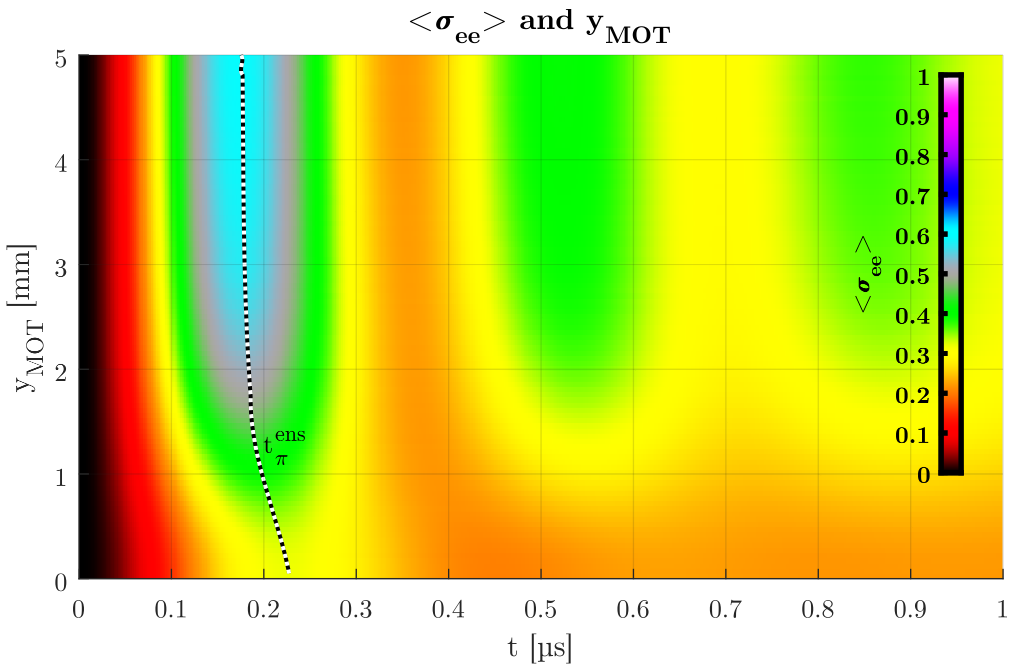

Figure 3.17: *Population dynamics depending on the location of the anti-Helmholtz magnetic field center. If it is offset more than about 3 mm, the ensemble is relatively unaffected.*

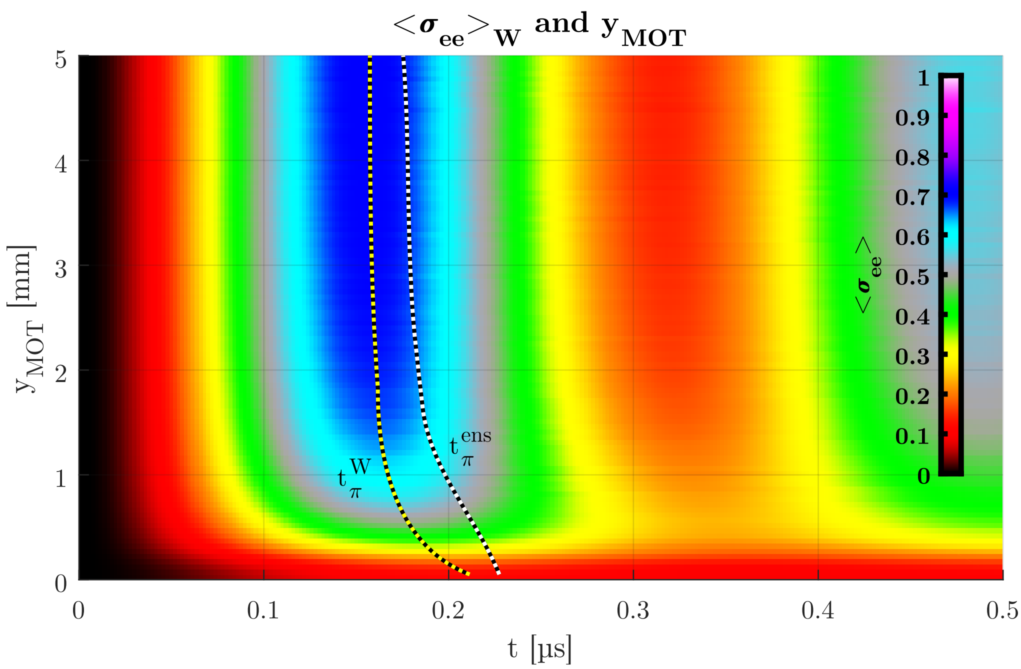

Figure 3.18: *Population dynamics for atoms within the cavity waist, depending on the location of the anti-Helmholtz magnetic field center. If it is more than 2 mm, $\langle\sigma_{ee}\rangle_W$ is barely effected, but for small offsets, the excited population will be very low.*

3.2.8 The Pump Pulse Beam Direction

In Chapter 2 we saw how the atomic interaction with the cavity field strongly depends on the atom's velocity along the cavity axis. Similarly for the pump pulse - assuming it is on resonance with the transition, the slowest atoms along the beam direction will interact most strongly with the field. We are interested in a stable frequency reference, so we would like for the cavity output pulse to have frequencies that are as close to the atomic transition as possible. As we shall see in Section 3.3, this frequency may be influenced by the speed along the cavity axis of an atom that spontaneously decays, as this leads to a Doppler detuning. To minimize this thermally induced spread in frequencies of the spontaneous emission, one can preferentially excite the atoms that move slowly along the cavity axis: This is where the pump pulse direction becomes important. In our experiment the beam direction is $\phi_p \approx 45°$ with respect to the cavity axis, but as seen in Fig. 3.19, we can create a stronger velocity-dependence of $\langle\sigma_{ee}\rangle$ by aligning the pump pulse as closely as possible with the cavity axis. This will increase the probability that the slowest atoms along the cavity axis spontaneously emit, and decrease the probability for the fastest atoms.

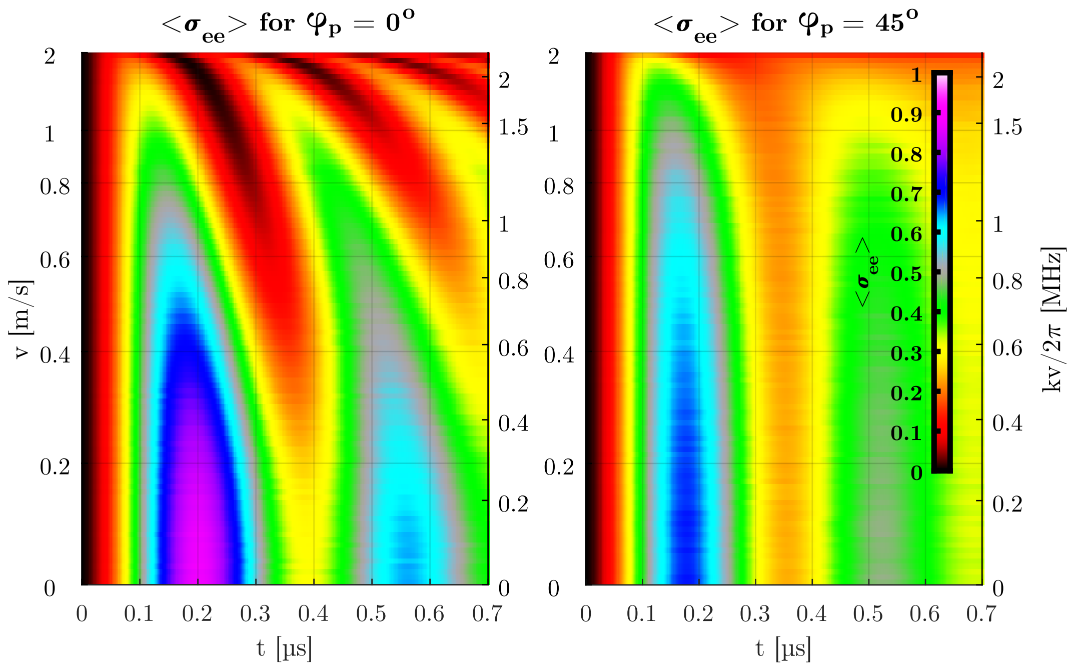

Figure 3.19: *Ensemble population dynamics during the pump pulse, for two pump beam angles ϕ_p with respect to the cavity axis. The y axes show the velocity along the cavity axis - the ensemble is divided into 100 velocity groups with an equal number of atoms, and the y axis is scaled so a certain range corresponds to a constant number of atoms within the range. If the pump pulse is aligned with the cavity axis one can preferentially excite the slow atoms along the axis.*

We also see in Fig. 3.19 that the pulse durations required to maximally excite atoms with a certain velocity varies, especially when ϕ_p is low. For $v_z = 0$, the maximum of 86.5 % excited atoms occurs after 209 ns, while for $v_z = 1$ m/s, the numbers are 36.4 % excited atoms after 135 ns. This is because the fast-moving atoms oscillate with a high generalized Rabi frequency, but the slow atoms will oscillate at a frequency near χ_p. To maximally excite the slowest atoms, rather than simply the whole ensemble or intra-cavity atoms, one would therefore need to apply a pulse that is longer than either t_π^{ens} or t_π^W respectively.

It should be noted that experimentally, the cavity mirrors would make it impossible to realize $\phi_p = 0°$ with the pump beam we are using. Exciting the ensemble with the seed laser (for an arbitrary power) would create an intra-cavity field with dynamics on the timescale of κ, which would be much longer than required to realize an ensemble π pulse. This would make it unrealistic to gain an inversion within the ensemble, and for our system to act as a master laser. The main point for the experiment is that ϕ_p should be minimized. Some windows in the vacuum chamber may enable $\phi_p \approx 25°$ - otherwise the vacuum chamber would have to be modified, which is of course not a simple task experimentally.

3.2.9 Decoherence

Spontaneous emission leads to decoherence at a rate $\Gamma_{eg}/2$, but atomic collisions or scattering of remnant MOT laser light can increase the decoherence rate further. In the case of collisions, the increase in decoherence rate would depend on the density and velocities (and thus temperature), being highest in the center of the ensemble. If remnant MOT light has a significant effect, it will most likely be time-dependent and decay exponentially after the MOT lasers are turned off. If the decoherence rate is significantly higher than the rate due to spontaneous emission, the ensemble Rabi oscillations during the pump pulse will be damped faster.

3.2.10 The Number of Atoms

The dynamics of the pump pulse interaction does not depend on the number of atoms in the ensemble, because we look at fractional populations and because the pump pulse has been approximated by a classical field which is not affected by the atoms. For the same reason the number of atomic groups affects the statistical uncertainties in the simulations, but should not give rise to systematic bias. The number of atoms used for simulations in Section 3.2 is 70 million, and the number of simulated atomic groups is 70,000 (700,000 in Section 3.2.7 and 3.2.8). The reason why many figures showing dynamics of the atoms within the cavity waist tend to feature horizontal line artifacts is due to the 'low' number of atomic groups within the cavity waist, which give rise to variations depending on the random initial positions and velocities of the atoms.

3.3 Lasing Dynamics of the Ensemble

After the pump pulse excites a fraction of the ensemble, the atoms will start to decay, spontaneously emitting in all directions. A small fraction of this light may be emitted into the cavity mode. If more than 50 % of the atoms within the cavity mode are excited, the spontaneous emission may be stimulated rather than absorbed on average, so an intra-cavity field builds up - the atoms start lasing. This light leaks out of the cavity at the rate κ, and in the decay and stimulated emission processes, the atoms transition from the excited to the ground state. Thus the inversion only lasts for a short while before $\langle \sigma_{ee}^{W} \rangle$ is below 0.5 again, and absorption dominates. The result of these processes is a short pulse in the intra-cavity power, which can be observed in the cavity output power. For the experiment to work as stable frequency reference, the objective is for this pulse to always have the same frequency. Therefore we investigate the dynamics of the lasing pulse in this section. In Fig. 3.20 we give an overview of definitions that will be used extensively throughout this section and an example of the dynamics for the population within the cavity waist and the cavity output power. When we compare the influence of different parameters on the dynamics, we will use heat maps with colors representing the fractional excited population and output power. We will often align simulations along the time axis by the peak output power at t = 0, making it easier to compare the lasing dynamics while the lasing delay can still easily be read off the axis as a negative time.

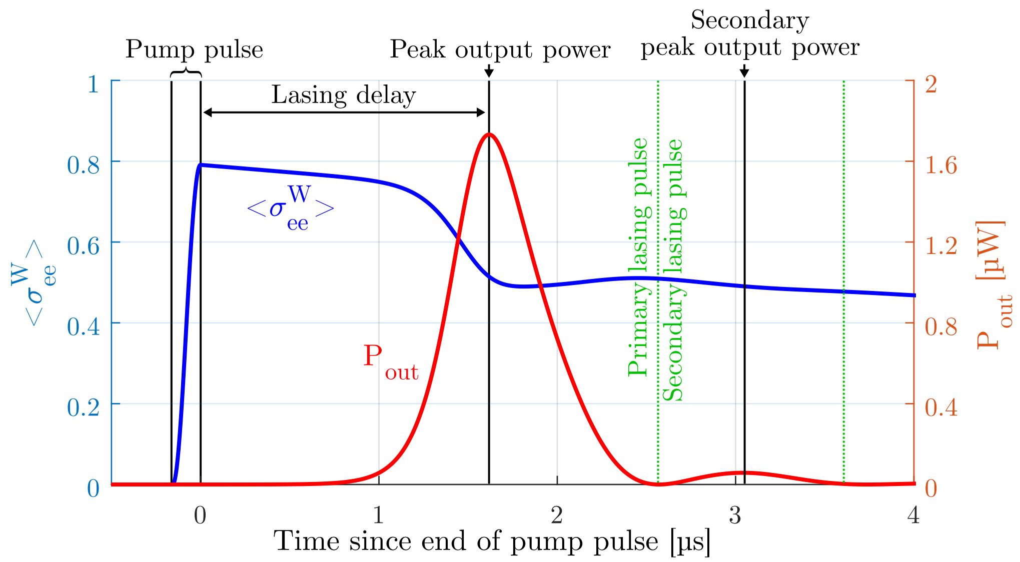

Figure 3.20: *Dynamics of the intra-waist population and the cavity output power during the pump pulse and lasing process, including relevant definitions.*

The model derived in Section 3.1 neglects spontaneous emission into the cavity mode, which may be a significant effect when the ensemble is excited but there is no cavity field. In the model, it is the coherence built up by the pump pulse which enables the ensemble to emit into an empty cavity mode. Spontaneous emission into the cavity mode could be implemented by including a white noise vacuum term for the intra-cavity field which corresponds to half a photon, or using a Heisenberg-Langevin approach [13, p. 121-124]. This limitation of the model means the initial field may be built up rather differently from how we expect it to happen experimentally. However, once a field has begun to build up, or if we drive the cavity with a seed laser, the dynamics of the model should capture the main physical effects of the experiment leading to the cavity pulse, namely stimulated emission and absorption.

Because we are now interested in the lasing dynamics, the following section will not use all the same standard parameters of Table 3.1. In general, the model predicts less cavity output power than we observe experimentally, if running simulations with the parameters we estimate are most likely. Many of the parameters are not known very accurately however - the temperature could be as low as 1-2 mK, or the ensemble size smaller, and vary between different experiments. The standard parameters for comparing the lasing dynamics are shown in Table 3.2. These are chosen as a compromise between using values that reproduce lasing with comparable intensity to what is observed as of May 2018, while also staying close to experimentally plausible values. Throughout this section (excluding 3.3.1), the pulse durations will be chosen as t_π^W, differing for each simulation, depending on the different parameters as found in Sec. 3.2. Note that the simulations in Section 3.3.1 use N = 10^8 and a fixed pump pulse duration of 118 ns.

Parameter	Symbol	Standard value
Pump pulse power	P_p	100 mW
Temperature	T	3 mK
Ensemble size	R	0.8 mm
Pulse waist	W_{xz}, W_y	2.5 mm, 2.5 mm
Magnetic field offset	y_{MOT}	4 mm
Number of atoms	N	$80 \cdot 10^6$

Table 3.2: *Standard parameters for investigating the ensemble dynamics during the lasing process.*

3.3.1 Pulse Variations and Simulation Uncertainties

We use a second order Runge-Kutta method to simulate the time evolution of the system. It is illustrated in Fig. 3.21 and is the second order Runge-Kutta method which minimizes the third order local truncation error [11, p. 1109]. Generally, the smaller the timestep dt, the more accurately the simulation replicates the dynamics, but the longer it also takes to simulate. Ideally we use a timestep that is high enough so we can run many simulations and obtain good statistics, but low enough as to not bias the results.

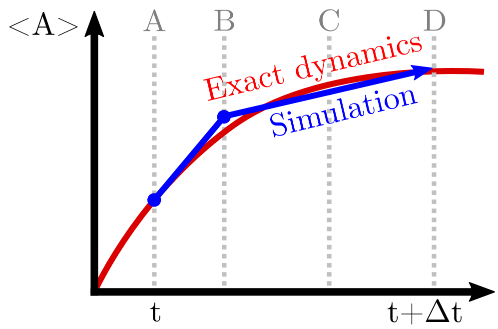

Figure 3.21: *The Runge-Kutta method used in this work to numertically integrate from t to $t+\Delta t$: One goes from A-B (1/4 of Δt) via the Euler method, and from B-D (3/4 of Δt) via the midpoint method, using the time derivative at C.*

Therefore we investigate the influence of the timestep on the primary characteristics of the lasing dynamics. The dt-dependence of the peak cavity output power and lasing delay is shown in Fig. 3.22. We see that the optimal timestep is about 1 ns - for longer timesteps the cavity output peaks become systematically biased towards higher power. For timesteps above 2 ns, the lasing delays also become systematically shorter. Based on these results the dynamics studied in the following sections are simulated with timesteps of 1 ns.

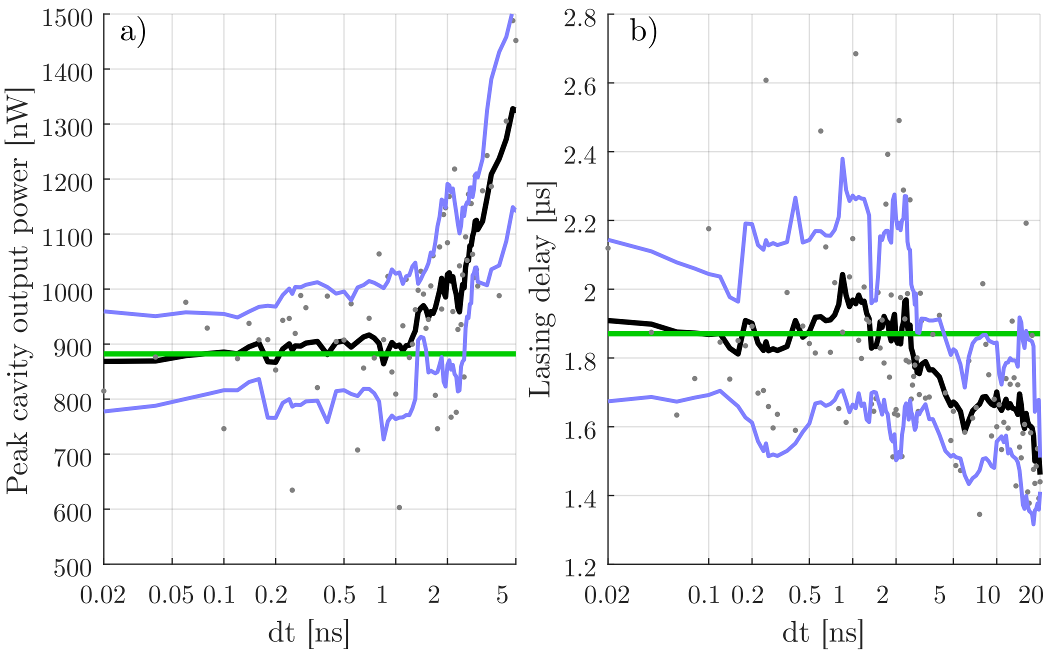

Figure 3.22: *Simulation results for the lasing pulse peak output power (a) and delay (b) for various timestep values dt. Black line: running mean, plus/minus running standard deviation (blue). Green: mean of the 10 simulations with lowest timestep. For timesteps longer than about 1 ns, the results become biased towards higher peak power, and for dt > 2 ns, shorter lasing delays.*

A second result which is apparent from Fig. 3.22 is that there is a large variation in the results between each individual simulation. The lasing process is inherently random and extremely sensitive to the initial conditions - the positions and velocities of each atom in the cavity. Recalling Section 2.4, we found that if the intra-cavity power is low, only atoms with a very narrow range of atoms interact strongly with the cavity field. Thus the random positions of just a few atoms may determine how soon the lasing sets in. In reality it is also random when a spontaneously emitted photon is emitted into the cavity mode and amplified. So even though our model does not include spontaneous emission into the cavity mode, we can expect the peak power and delays of the actual pulses to vary, but not necessarily by the same amount as predicted by the model.

Another important approximation is the atomic grouping. Ideally we want to include enough atom groups in the simulations so that the results are not biased by the approximation, but also few enough that we can obtain many results. Therefore we investigate how the primary simulation results vary depending on the number of atoms per group - the results are shown in Fig. 3.23. These have been studied[3] in two cases: One without truncating the ensemble, and another case where the ensemble was cut off at $x^2+y^2 = (1.5W)^2$ (we will soon return to this truncation). The cutoff enabled us to run simulations with smaller atomic groups than the simulations of the full ensemble. What we find is that for the range of atomic group sizes we have studied, there appears to be a bias in both the peak delay and power scaling roughly with the logarithm of the atomic group size, though the logarithmic fits appear to be slightly too pessimistic about the error, comparing the running mean for 5-20 atoms per group.

[3] In these simulations $W_{pxz} = 5$ mm, $W_{py} = 0.7$ mm, R = 1 mm, T = 4 mK and N = 10^8.

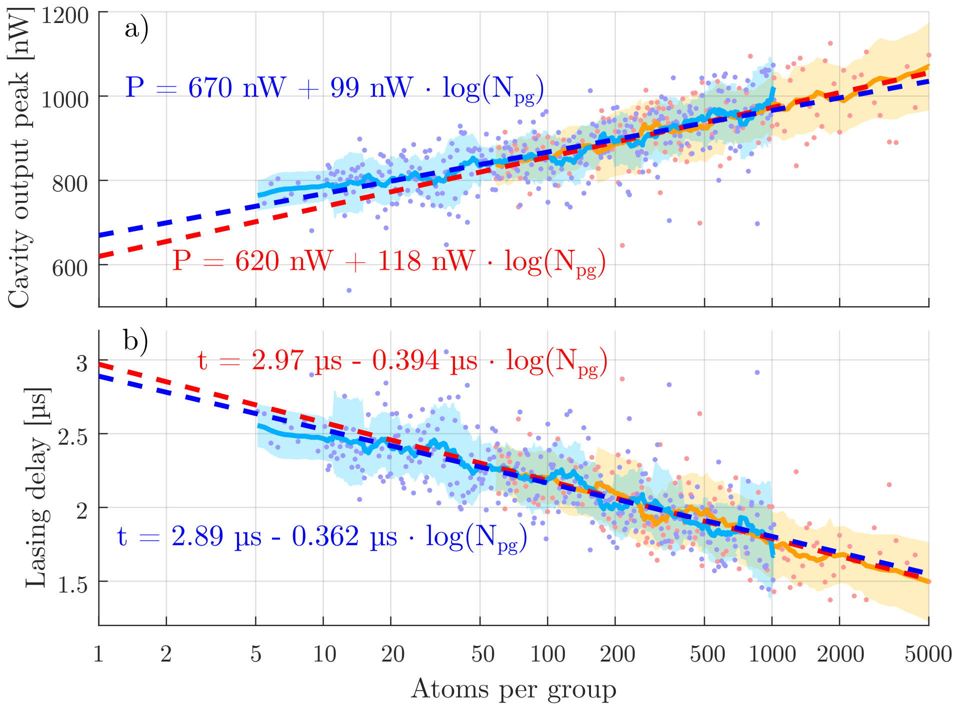

Figure 3.23: *Simulation results for the cavity output pulse peak power (a) and delay (b) for various atomic group sizes. Red: all atoms simulated, blue: ensemble truncated at 1.5W. Points: raw data. Lines: running mean with a span of 20 points, shaded areas: ± running standard deviation. Dashed lines: logarithmic fits.*

The physical reason for this bias could be that by replacing atoms by larger atomic groups, we effectively cluster many atoms together, which makes the ensemble interact more coherently with the cavity field than in reality, causing the process to run more quickly. In the interest of being able to obtain statistics on our results, we aim for a value of about 200 atoms per group for simulations, and note that the results may be systematically biased up to 35 %. When presenting dynamics of single simulations we will aim for 20 atoms per group, leading to < 20 % bias.

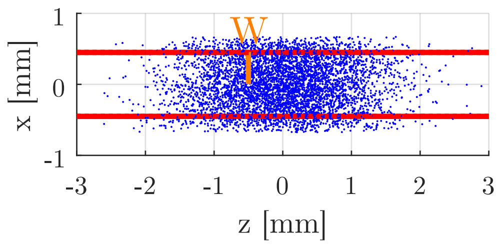

Figure 3.24: *A simulated R = 0.8 mm ensemble (blue) cut off at $x^2+y^2 > (1.5W)^2$, improving performance by a factor 3. The cavity beam waist is shown in red.*

Returning to the ensemble truncation - as illustrated on Fig. 3.1 a big part of the ensemble is far away from the cavity mode. If R = 0.8 mm, 70 % of the atoms are further than 1.5 · W from the cavity axis. Here the intensity is less than 0.3 % of the intensity at z = 0, so atoms further away might to a good approximation not contribute to the lasing process. As seen on e.g. Fig. 3.19, common thermal speeds are at most a few μm/μs. The pump and lasing dynamics together last on the order of 10 μs, much shorter than the 3W traversing timescale ≈ 1.4 ms, so we need not worry about a significant population of atoms crossing the demarcation. To make sure the results are not biased by the ensemble cutoff, we study the pulse peak power and delay for various cutoff values, shown in Fig. 3.25. It should be noted that the simulation renormalizes the number of atoms per group when cutting off the ensemble, so the varying number of atoms per group slightly affects the results. Since we know the approximate effect of this, the fit relations of Fig. 3.23 have been used to renormalize the running mean values.

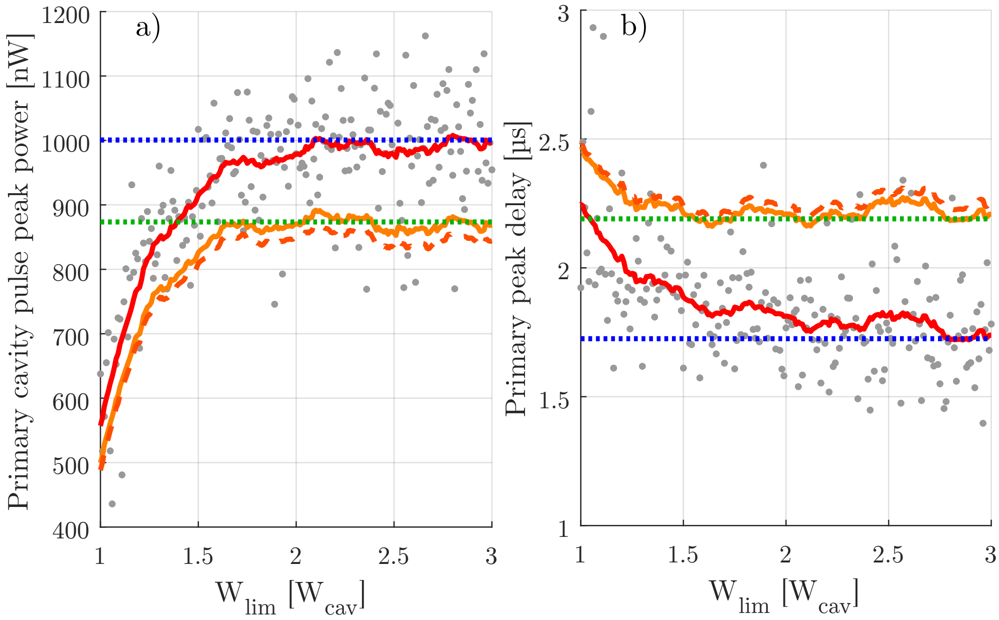

Figure 3.25: *Cavity output pulse peak power (a) and delay (b) for varying ensemble cutoff radii W_{lim}. Gray: Simulations. Red: Running mean with 30 point span. Blue: Mean of the 30 rightmost points. Orange/green: Running/rightmost means renormalized to minimize the influence of the varying number of atomic groups, based on fit relations (full line: Blue fits, dashed: Red fits) of Fig. 3.23. It is renormalized to correspond to 25 atoms per group. We see W_{lim} should be at least $1.7 \cdot W_{cav}$.*

If the ensemble is cut off at a too low radius from the cavity axis, atoms will be cut away which would have interacted with the cavity field and contributed to the lasing process, causing a bias towards lower peak power and a longer delay. We see that for cutoff radii smaller than 1.7 times the cavity waist, the peak power is biased after renormalizing, while for the lasing pulse delay, there is no clear bias for cutoff radii larger than 1.3W. Based on these results, a cutoff value of $x^2 + y^2 > (1.7W)^2$ is chosen.

3.3.2 The Lasing Process - Qualitative Expectations

In Section 2.4 we studied how a single atom interacts with the cavity mode, depending on its velocity along the cavity axis. Here the system was in equilibrium, where the cavity input power equals the output power. During the lasing process the output power has the same dependence on the intra-cavity power as in the steady-state case, and the intra-cavity power is all that matters for the atoms. Thus we can substitute the input power with the output power in e.g. Fig. 2.5 for comparing the steady state dynamics with the lasing process. The steady state excitation probability gives us a very rough idea of approximately which atoms will participate in the lasing process for a given output power - since it was derived in the steady state, it cannot be directly translated to the rapidly changing dynamics during the lasing process, but may still give us qualitative insight in the process. This is illustrated in Fig. 3.26.

When the cavity field is very weak at the beginning of the process (a), only the slowest atoms along the cavity axis (or atoms whose Doppler shift corresponds to the cavity detuning) interact with the cavity mode. As these atoms amplify the field (moving to higher P_{out} on the figure), power broadening enables atoms with an increasingly broad range of velocities to interact, further amplifying the field. At one point (b), the loss through the mirrors grows above the energy supplied by the atoms - the cavity output power reaches its peak value. At this point, the field intensity and power broadening starts to decrease again, so now the range of velocities interacting with the field starts to decrease again until the end of the pulse (c). During the later stages of the process, the excited population is lower, and if there is no longer any inversion, the interacting atoms will be absorbing rather than emitting.

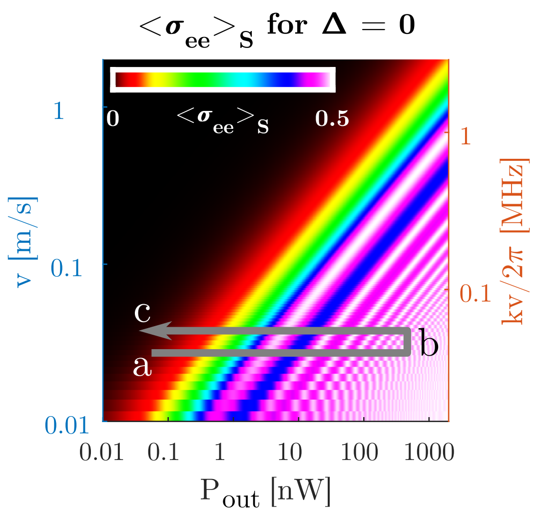

Figure 3.26: *Steady state excitation probability for an atom in a resonant cavity. This is compared to the cavity output dynamics during a lasing pulse, where the output power first grows from 0 (a) to a given peak value (b), then back to 0 (c).*

3.3.3 Dependence on Cavity Detuning

The simulated dynamics of the cavity output power and atomic populations are shown in Fig. 3.27 and 3.28. We see that as the cavity detuning is increased, the primary lasing pulse peak power decreases, but oscillations in the cavity output power become more prominent up to $\Delta = 1.3$ MHz. For even higher detuning there are increasingly few atoms with the corresponding Doppler shifts, so the lasing pulses do not build up to as high intensities.

On Fig. 3.28 we mark the end of the primary pulse. If there is a significant inversion at this time, it can lead to a secondary emission pulse, which can again be partially re-absorbed and emitted, in similar dynamics to a damped pendulum. This behavior has also been studied by R. Brecha et al. [15].

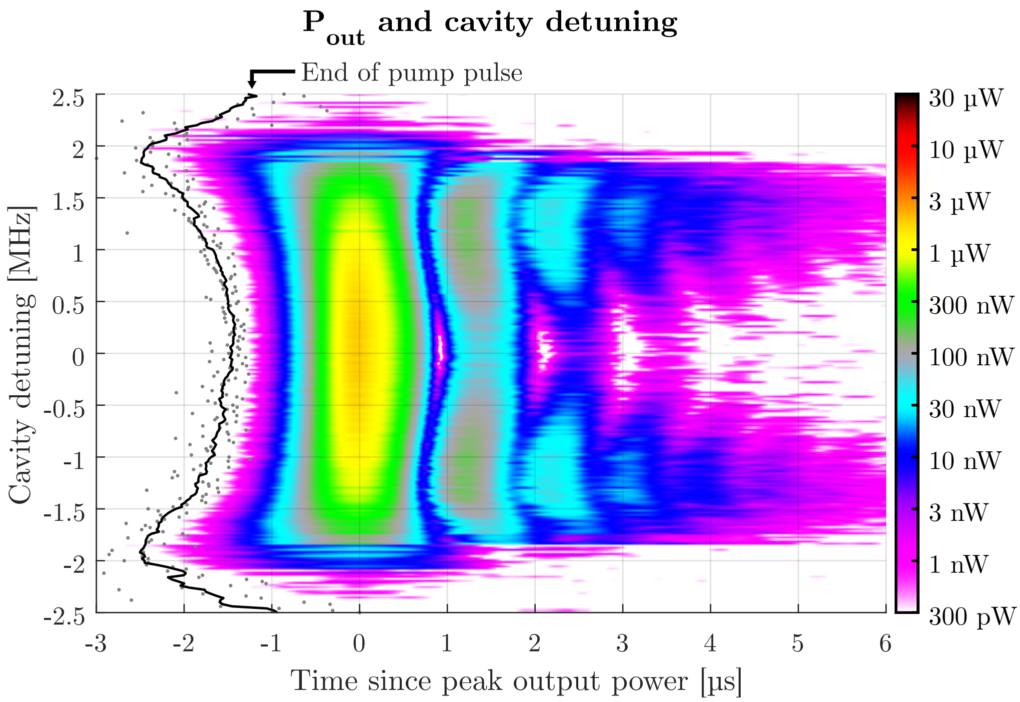

Figure 3.27: *Time evolution of the cavity output power for varying cavity detuning. Gray dots: end of pump pulse, black line: running mean. For a resonant cavity, the primary lasing pulse is intense, but later pulses are weaker. For a detuned cavity the primary lasing pulse is less intense, but oscillations in the output power are more prominent.*

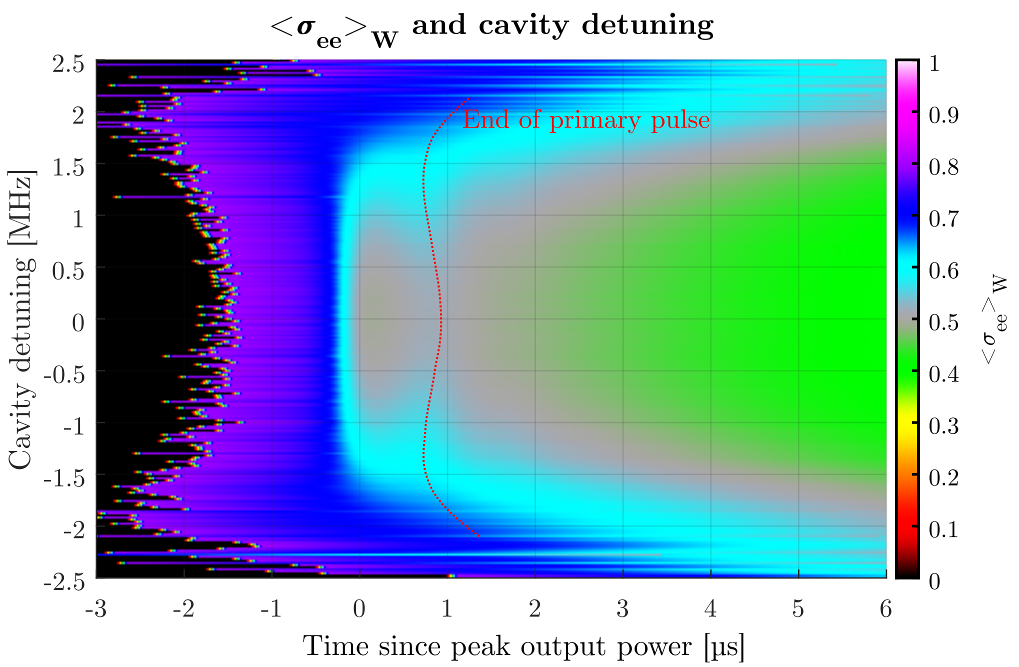

Figure 3.28: *Intra-waist population dynamics for a range of cavity detunings. For a detuned cavity the excited population at the beginning and end of the primary pulse is very similar, enabling multiple lasing pulses. For a cavity on resonance much of the energy leaks out of the system during the primary pulse, so $\langle \sigma_{ee}^{W} \rangle$ is not driven back up to as high values.*

The primary and secondary peak power as function of detuning are shown in Fig. 3.29. Since the cavity detuning determines which atomic velocity group initiates the lasing process and how strongly the atoms couple to the cavity field, we may use it to probe the temperature of the ensemble, since the velocities are thermally distributed. To investigate this possibility a one-dimensional Maxwell-Boltzmann distribution is shown Fig. 3.29, representing the distribution of Doppler shifts along the cavity axis given a temperature of 3 mK. We see that the width of the primary peak power distribution is similar to the Boltzmann distribution, but the peak power distribution is somewhat different - once the process is initiated, many different factors determine the peak power. Simply fitting a Maxwell-Boltzmann distribution to the peak power distribution would yield a temperature of 4.3 mK for a simulated temperature of 3 mK. Thus it might serve as an order of magnitude estimate of the temperature, but is not an accurate method to determine it.

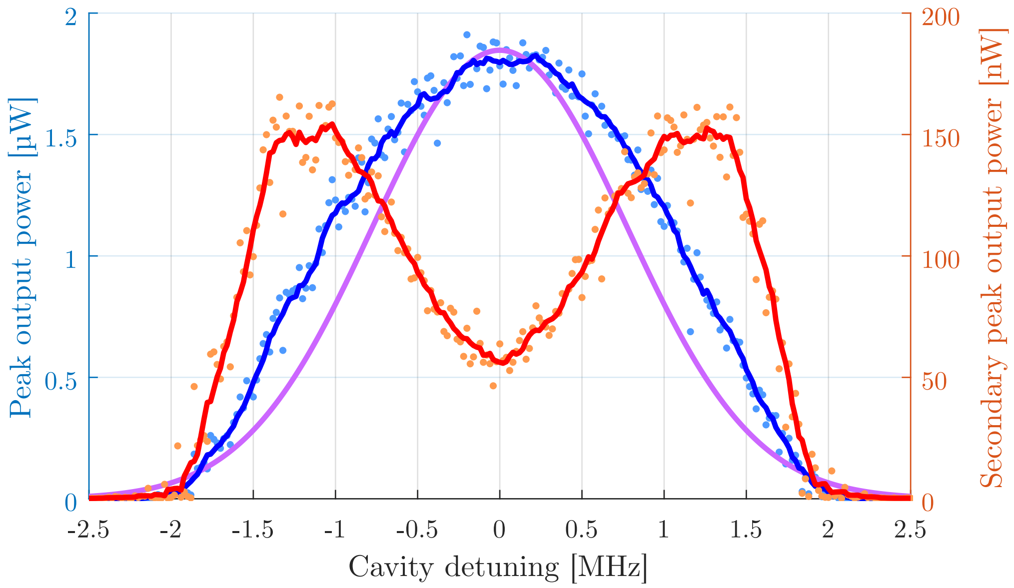

Figure 3.29: *Left axis (blue): peak output power, depending on the cavity detuning. Right axis (red): peak power of the secondary pulse. Points: simulations, lines: running mean. Purple: 1D Boltzmann distribution for 3 mK. We see the primary lasing pulse peaks have a similar width as the Boltzmann distribution, but a somewhat different shape. For certain detunings the secondary pulse peaks are more prominent.*

3.3.4 Velocity-dependent Dynamics

We saw in Section 3.3.3 that the lasing pulse dynamics showed prominent oscillations for a detuned cavity. Here we will study the lasing process in velocity space, where a notable difference between the resonant and detuned cavity dynamics is revealed. We divide the ensemble into 100 velocity groups with an equal number of atoms, and for each velocity group, we look at how the atoms interact with the cavity field. The term in the equations of motion for the ensemble (Eq. 3.5) describing the change in the atomic state due to emission/absorption of the cavity field is given by:

$$\left\langle \dot{\sigma}_{ee}^{i,cav} \right\rangle = i \sum_{i=1}^{N_g} \left(g_i \left\langle a^\dagger \right\rangle \left\langle \sigma_{ge}^i \right\rangle - g_i \left\langle a \right\rangle \left\langle \sigma_{eg}^i \right\rangle \right) \tag{3.9}$$

It equivalently describes the change in the cavity field: If one atom changes from excited to ground state, the photon population of the cavity field increases by one.

By looking at how this term changes after the lasing pulse for each velocity group we can see how atoms with different velocities emit and absorb cavity photons as a function of time. The results from simulations are shown in Fig. 3.30 for the cavity on resonance, and 3.31 for a cavity detuning of 1.3 MHz where the secondary output power peaks are most prominent.

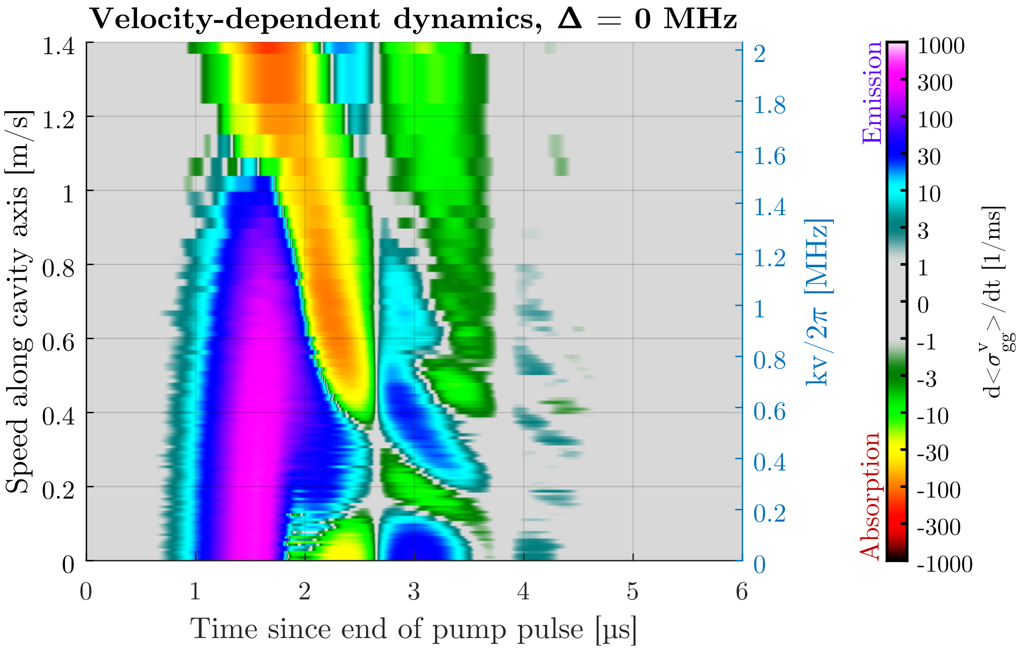

Figure 3.30: *Atomic emission (blue-purple) and absorption (green-red) of cavity photons during the lasing process for different velocity classes in a resonant cavity. The structure is disordered - different velocity classes emit and absorb photons at the same time throughout the process. Note the color scale is logarithmic.*

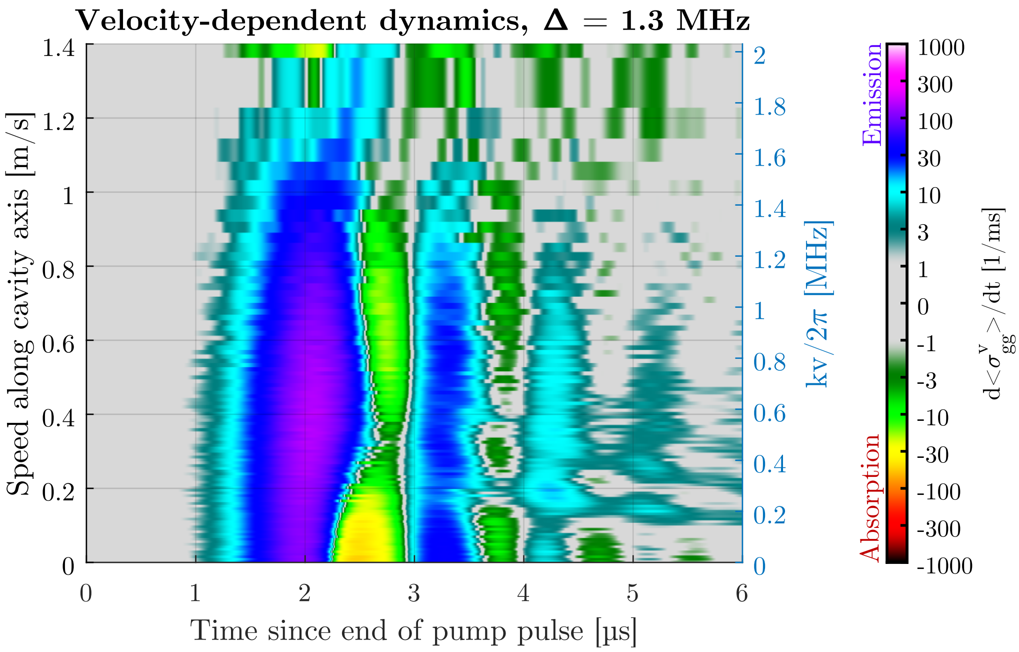

Figure 3.31: *Atomic emission and absorption of cavity photons during the lasing process for different velocity classes in a detuned cavity. The structure is much more ordered across the velocity classes than for the resonant cavity: During the process, most atoms either emit or absorb at the same time, which may promote oscillatory behavior.*

Note the quantities for $d\left\langle\sigma_{gg}^{v}\right\rangle/dt$ shown in Fig. 3.30 and 3.31 are the mean for a given velocity group within the ensemble cutoff at 1.7 times the cavity waist. Therefore the exact values are not so representative for the atoms interacting strongly with the field, but the relative difference between them is the main quantity of importance. Secondly, there are many more slow than fast atoms due to the thermal velocities, therefore the velocity bins cover a smaller range for the slow atoms, as they contain equal numbers of atoms.

The first result from these simulations is that it is not very clear exactly which velocity class dominates in initiating the lasing process. Based on the theory for the single atoms, we would expect it to be the atoms with Doppler shift $\mathrm{kv}/2\pi = 0$ for the resonant cavity, and $\mathrm{kv}/2\pi = 1.3$ MHz for the detuned cavity. However it appears that all the velocity classes become involved in the lasing process very quickly - the single-atom results derived in the steady state limit may not be very applicable for this rapid process. The corresponding Doppler shifts to the range of velocities quickly taking part in the process is on the MHz scale, larger than $\kappa = 2\pi \cdot 620$ kHz, thus one can probably not consider the system in the bad cavity regime at $\mathrm{T} = 3$ mK.

A second thing to note is that the excitation probability after the pump pulse varies across the velocity groups, and this has an influence on which atoms emit or absorb at a given time. As we saw in Fig. 3.19, there will be a gradient in the excitation probability after a pump pulse - it will be highest for the slowest atoms, and lowest for the fast atoms. This gradient can be changed by detuning the pump pulse or as shown in Section 3.2.8. However in this case where the pump pulse is on resonance, it means the fast atoms will initially tend to absorb rather than emit into the cavity mode. As the process evolves, the excitation probability rises for the fast atoms as they absorb, and it decreases for the slower atoms which are emitting. Once there is an inversion within the fastest velocity groups at $\mathrm{t} = 2.2$ μs, they start emitting rather than absorbing, and vice versa for the slowest atoms at $\mathrm{t} = 1.9$ μs. However the excitation probabilities are also spatially dependent. The intensity is highest at $\mathrm{x} = \mathrm{y} = 0$, so atoms here will oscillate with a higher Rabi frequency than atoms further from the center. In the case of the resonant cavity we may expect that atoms at larger distances from the center contribute to the process due to the higher intensity achieved, compared to the detuned cavity. The spatial dependence means the excitation probabilities vary locally and this also has an influence on which velocity groups tend to emit or absorb at a given time.

3.3.5 Spatially-dependent Dynamics

There are two main factors which lead to macroscopic spatially-dependent dynamics in the ensemble during the lasing process. The first is the cavity waist radius of 0.45 mm, which means the intensity of the intra-cavity field decreases exponentially with increasing distance from the cavity axis at any given time, leading to a large variation in the coupling parameters g_i. The second factor is the gradient in the excitation probability following the end of the pump pulse due to the finite waist size of the pump beam. The first effect is symmetric around the cavity axis, while the second effect has a symmetry axis along the pump beam. Since we are generally interested in pump beams that have large waists compared to the cavity mode and especially along the cavity axis, the first factor is often dominant and we will study how the dynamics depend on the radial distance from the axis.

As in Section 3.3.4 we study the evolution of the terms in Eq. 3.9 for the ensemble, now divided into 100 groups depending on their radial distance from the cavity axis. Since the atoms move, some of the atoms will move between different classes during the lasing process, but the effect of this is small due to the low thermal velocities of $\approx 1\ \mu$m/μs compared to the mm dimensions of the cavity waist and μs timescale of the lasing process.

The absorption and emission dynamics depending on the radial distances are shown in Fig. 3.32 for the resonant and detuned cavity examples of Section 3.3.3 and 3.3.4. First note that the resolution is more coarse for the low distances from the cavity axis because most atoms are further away from the cavity axis. The position grouping is based on 100 cylinder shells containing (initially) an equal number of atoms, and the inner cylinders must have larger radii to have a big enough volume to contain as many atoms as the outer shells. There is a notable behavior for the atoms closest to the cavity axis for the resonant cavity. We see during the primary lasing pulse, lasting from t = 0.7 μs to 2.5 μs, the atoms within 0.1 mm of the cavity axis are repeatedly emitting and absorbing. These atoms are undergoing two ensemble Rabi oscillations during the primary lasing pulse (see population dynamics in Fig. 3.33) because the intensity grows larger than it does during the process for the detuned cavity. As all the atoms have different velocities, any Rabi oscillations will be damped and the intra-waist fractional excited population will (neglecting spontaneous emission and cavity decay on the lasing pulse timescale) decay towards 0.5. This is also a factor that can contribute to reducing the secondary lasing pulse compared to the situation for a detuned cavity, where $\langle \sigma_{ee}^{W} \rangle$ after the primary lasing pulse is closer to 0.6.

The higher intensity within the cavity in the resonant case also leads atoms further away from the cavity axis to interact more strongly with the field, and as a result we see that for the resonant cavity, atoms between 0 and 0.5 mm from the cavity axis end up reabsorbing photons during the primary lasing pulse. For the detuned cavity, the reabsorbing atoms are located between 0 and 0.4 mm only. This means more energy from the primary lasing pulse is deposited in atoms further away from the center for the resonant cavity compared to the detuned cavity. For the secondary and higher order lasing pulses to build up, a high fractional excited population is required for the position groups close to the cavity axis. If the intensity during the secondary pulse does not grow high enough to drive the reabsorbing atoms to emit again, this re-absorption of the outer atoms during the primary pulse acts as a dissipation mechanism for the lasing process - this energy will eventually be spontaneously emitted rather than contribute to lasing. This is another factor which can promote the damping of the cavity output power oscillations in the resonant case.

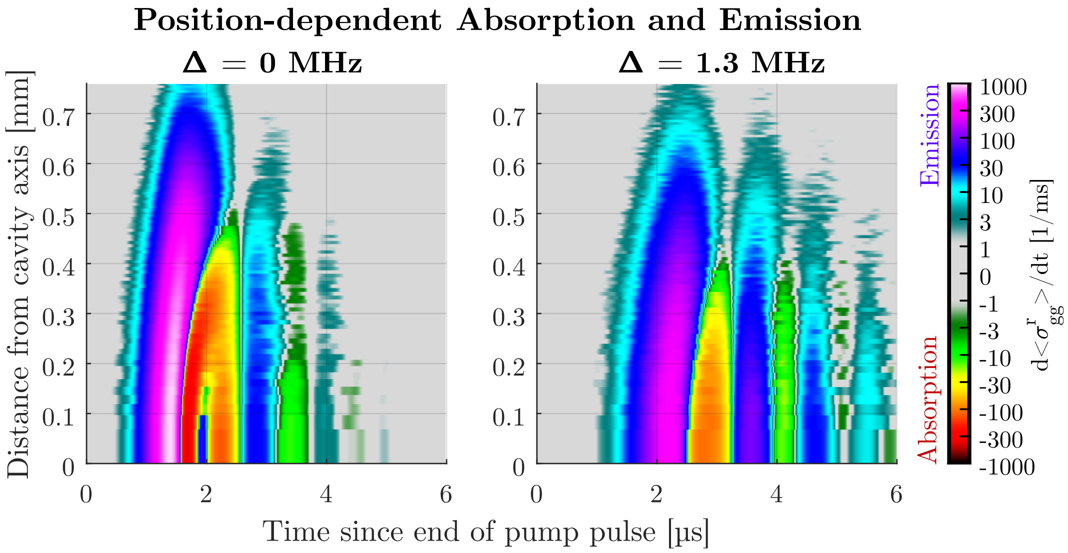

Figure 3.32: *Atomic emission and absorption of cavity photons during the lasing process for 100 position classes. For the resonant cavity (left), the atoms closest to the cavity axis undergo two Rabi oscillations during the primary lasing pulse between $t = 0$ and 2.5 µs.*

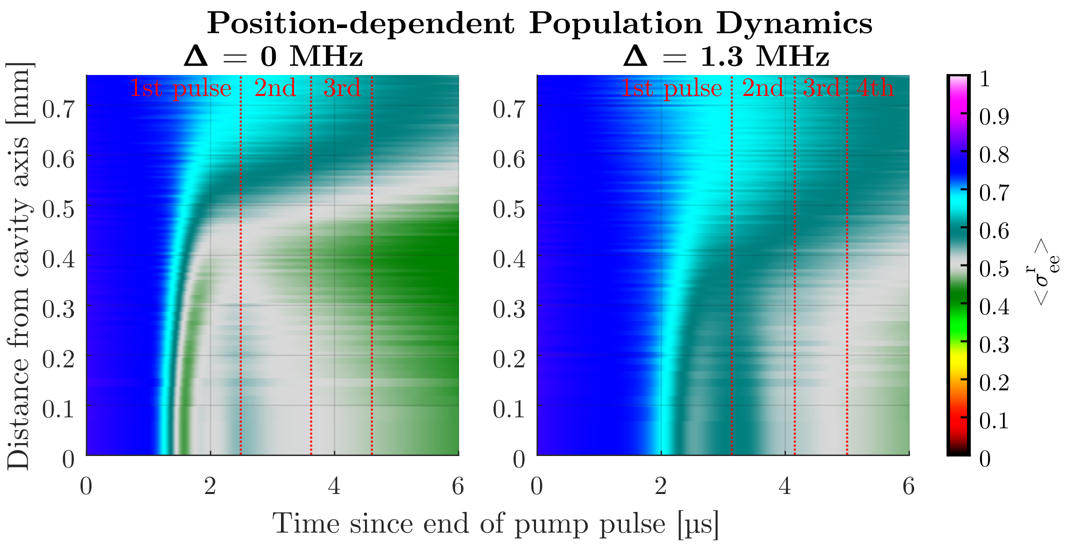

Figure 3.33: *Atomic population dynamics during the lasing process for 100 position classes. The mean fractional excited population is close to 0.5 following the primary lasing pulse for the atoms close to the cavity axis in the $\Delta = 0$ case, leading to less emission in the higher order pulses than for $\Delta = 1.3$ MHz.*

For an elongated pump pulse the spatial dependence of the population dynamics becomes more pronounced. If the pump pulse waist in the y direction is reduced to 0.5 mm, the excitation probability will vary from 90 % for the position groups within 0.2 mm of the cavity axis, to 40 % near 0.7 mm from the axis. Because of this, the atoms close to the cavity axis will emit more intensely into the cavity mode during the lasing pulse, but the atoms further than 0.6 mm from the cavity axis will absorb light during the primary lasing pulse. These dynamics can be seen in Fig. 3.34.

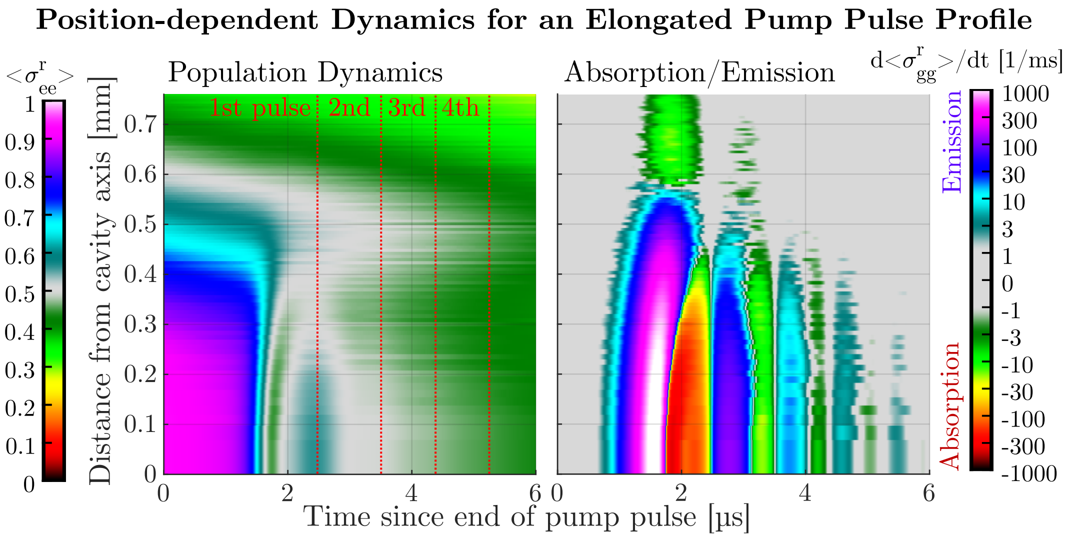

Figure 3.34: *Dynamics during the lasing process for 100 position classes with a pump pulse waist W_{py} = 0.5 mm. The gradient in excitation probability leads atoms further than 0.6 mm from the cavity axis to absorp photons during the primary lasing pulse.*

3.3.6 Optimal Pump Pulse Waists for Peak Output Power

In Section 3.2.5 we found the optimal pump pulse waist sizes for maximally exciting the whole ensemble ($W_{py} = W_{pxz} \approx 2.4$ mm) or the intra-waist population ($W_{py} \approx 0.75$ mm, $W_{pxz} \approx 2.3$ mm) for R = 1.0 mm. We saw in Section 3.3.5 that a highly elongated pump pulse could also lead atoms far from the cavity axis to absorb photons during the process, possibly reducing the cavity output signal. Thus the most robust way to determine the optimal pump pulse waists is to determine how the peak cavity output power depends on the waists. These results, now for R = 0.8 mm, are shown in Fig. 3.35.

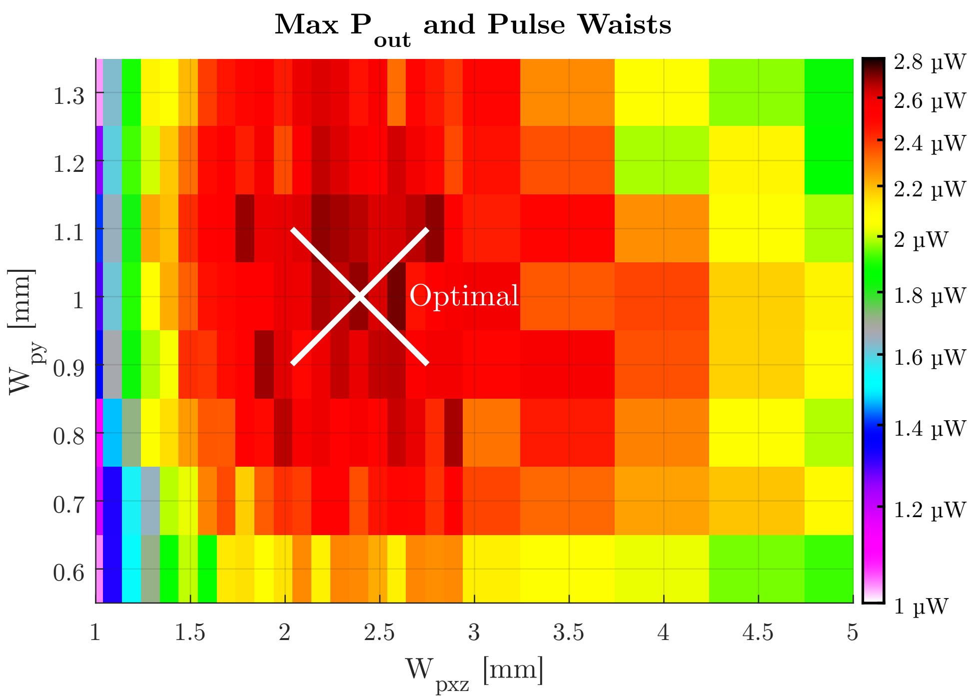

Figure 3.35: *Primary flash peak values depending on the pump pulse waist sizes. The optimal pump pulse for intense lasing pulses has $W_{py} \approx$ 1.0 mm and $W_{pxz} \approx$ 2.4 mm. Note the color scale differs from other figures.*

Here we find the optimal waist dimensions to be $W_{py} \approx 1.0$ mm and $W_{pxz} \approx 2.4$ mm. These yield a peak output power of up to 2.7 mW, an increase of 50 % compared to the 1.8 mW obtained with the standard parameters. We also see that the optimal pump beam profile for gaining an intense lasing pulse is indeed elongated along the cavity axis, but with slightly larger W_{py} than predicted when optimizing for maximally exciting the intra-waist population, despite R being lower. Thus the picture of looking at the intra-waist population was probably too narrow, and looking at the population within e.g. $1.5 \cdot \mathrm{W}$ may be more relevant for predicting the peak cavity output power based on the fractional excited population, which would be a significant advantage as it requires much less computing power than simulating the output peak power. However the optimal waists will also depend on the intra-cavity power - if for example, the MOT lasers were optimized after the pump pulse waists and we increase the number of atoms in the cavity mode, this leads to a higher intensity during the primary lasing pulse, so atoms further from the cavity axis will be driven significantly during the lasing process. Based on the results of Section 3.3.5 may expect increasing absorption for the outermost atoms to limit the output power somewhat, unless W_{py} is further increased. Thus the optimal W_{py} will generally increase for increasing intra-cavity power during the lasing process.

3.3.7 Dependence on the Number of Atoms

Intuitively, the higher the number of atoms, the higher intensity can build up during the lasing process. Since the pump pulse intensity is high, doubling the ensemble population also doubles the number of excited atoms after a pump pulse, so twice as much energy is pumped into the system. Based on this we may expect a linear relation between the energy of output pulse and the number of atoms. The simulated dynamics during the pumping process and lasing pulse are shown in Fig. 3.36 (the cavity output power) and 3.37 (population dynamics for atoms within the cavity waist). The output power and atomic populations are roughly related by $P_{out} \propto -d\left\langle \sigma_{ee} \right\rangle/dt$, neglecting spontaneous emission.

We find that for a low number of atoms (< 40 million), the output pulses are very faint (< 300 nW), but last a long time (≈ 3 μs) and also feature a long delay (≈ 3 μs) with respect to the pump pulse. For these values the population dynamics show that a part of the ensemble is transferred from the excited to the ground state during the emission process - but for 20 million atoms, the fractional excited population ends near 0.6, while for 40 million, it ends near 0.4. Thus the efficiency of the lasing process increases with the number of atoms within this range - for a very low number of atoms, the intra-cavity field is simply not intense enough that a significant fraction of the ensemble will couple to it and contribute to the process.

For a moderate number of atoms, e.g. 80 million, we see that during the process, the intra-waist fractional excited population oscillates from 70 % to 45 % and then back up to 55 % during the primary emission pulse; the atoms emit light into the cavity field, and while it leaks, also re-absorb part of it. As the number of atoms is further increased beyond 120 million, the intra-cavity field becomes so intense during the primary pulse that the atoms within half the cavity axis undergo multiple Rabi oscillations. These differ for each atom, depending on position and velocity, so when looking at the average of the intra-waist population, the oscillations are not very visible.

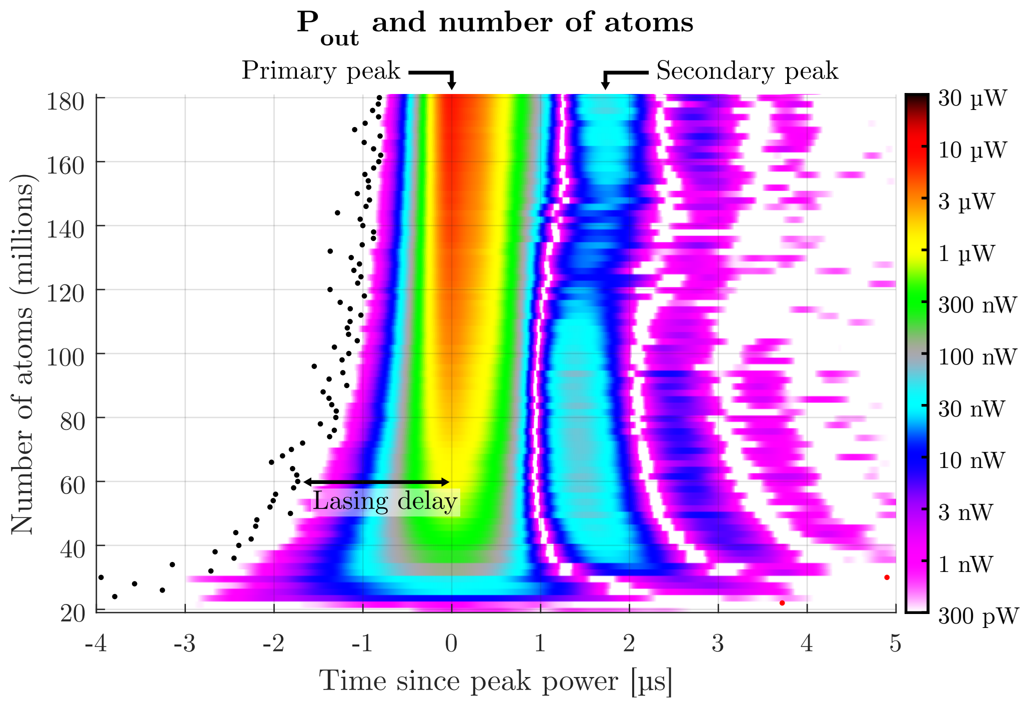

Figure 3.36: *The cavity output power as a function of time for different numbers of atoms in the ensemble. The simulation data are aligned so that the time of the peak output power coincide at $t = 0$. Black dots: End of pump pulse. The more atoms in the ensemble, the higher the peak output power and the shorter is the delay between pump pulse and peak power.*

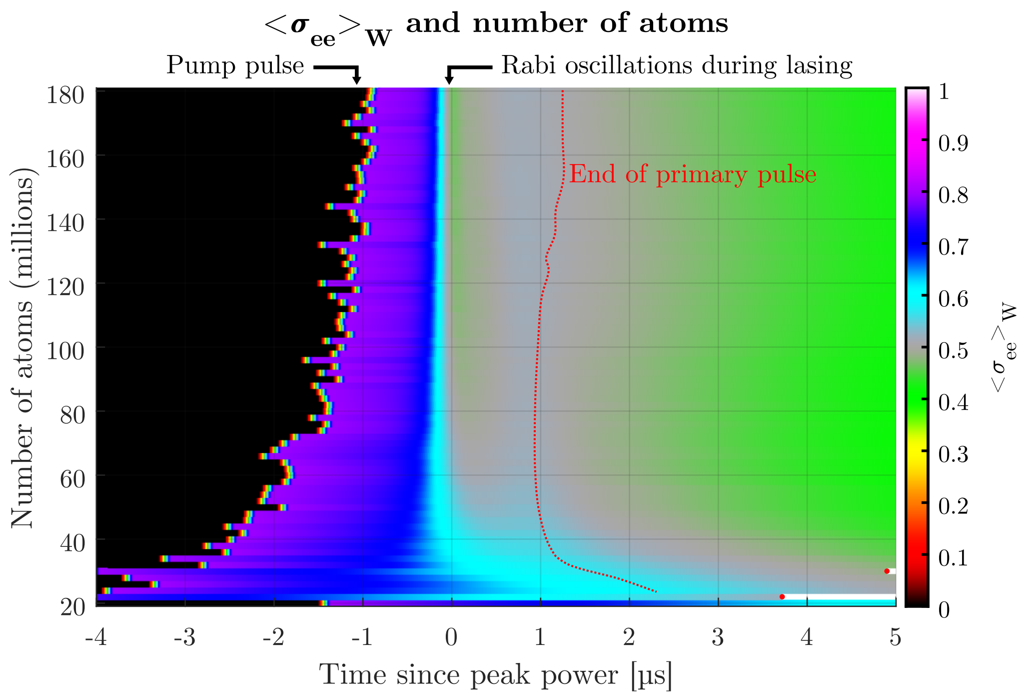

Figure 3.37: *Intra-waist population dynamics after a pump pulse, for different numbers of atoms in the ensemble. During the primary lasing pulse the atoms undergo Rabi oscillations, depending on the dynamics of the intra-cavity field. The secondary lasing pulse strongly depends on the resulting fractional excited population at the end of the primary pulse. The time axis refers to Fig. 3.36.*

The relation between peak output power and number of atoms is shown in Fig. 3.38. As argued, the emitted energy should scale linearly with the number of atoms in the high-N regime, and since we see the pulse process duration is relatively constant in this regime, the peak power should also scale linearly with N. This is indeed what is found in the simulation, while for less than about 80 million atoms, the lasing efficiency decreases and the relation is no longer linear. The peak output power of the secondary pulse is also shown. This relation is more complicated but, as found in Section 3.3.3-3.3.5, should be due to the Rabi oscillations of the ensemble during the primary pulse - especially the excitation probability of slow atoms near the cavity center at the end of the primary pulse. If that is the case, the ranges of N which yield intense or faint secondary pulses could be shifted if other parameters are varied which also affect the ensemble Rabi oscillations, such as the temperature.

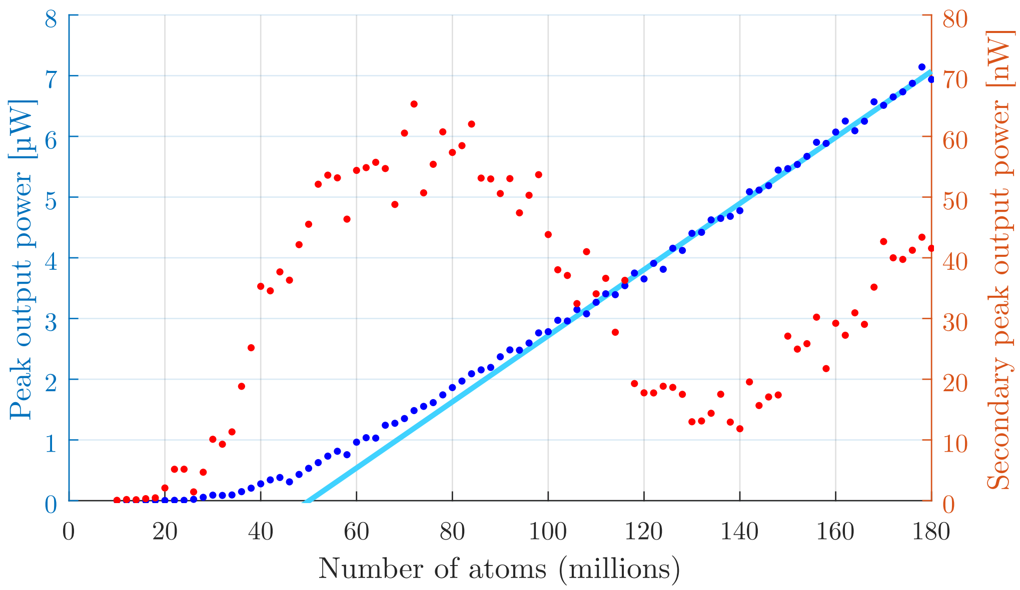

Figure 3.38: *Left axis: peak output power, depending on the number of atoms. Blue dots: simulations, line: linear fit for N > 100 million. Right axis, red dots: secondary peak output power. A higher number of atoms leads to increased peak output power, but the secondary peak depends on Rabi oscillations during the lasing process.*

The simulated relation between the number of atoms and the delay of the primary lasing pulse is shown in Fig. 3.39. Intuitively, if the number of atoms is doubled, twice as many atoms have a probability of initiating the lasing process in a given timeframe, and there will be twice as many atoms at a given time to amplify the field. Based on this a higher number of atoms should result in a shorter delay. This is also what we find for simulation data with $N \geq 20$ million, as seen in the fit in Fig. 3.39. For lower N the dynamics become much more random because very few atoms contribute to the process, so these results are excluded from the fit.

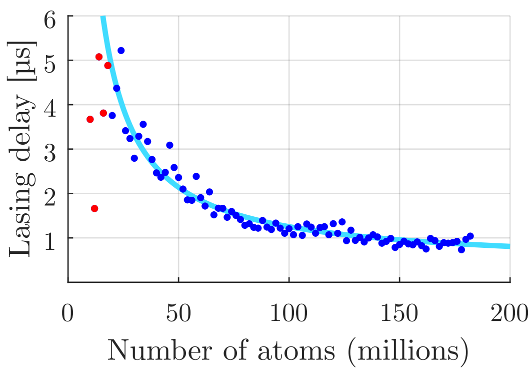

Figure 3.39: *Relation between number of atoms and the lasing pulse delay. Points: simulations. Line: fit ($a/x+b$). Blue/red: included/excluded in fit.*

The scaling with the number of atoms is characteristic for different processes. One process is Dicke superradiance (SR), where an ensemble of two-level systems is confined on the scale of a wavelength and whose dipoles are synchronized. For this system the emitted intensity scales with the square of the number of dipoles [16]. Atomic clock designs utilizing ensembles in this regime are under development, including ^{87}Sr [17]. While our model neglects SR effects due to factorizing the expectation values from eq. 2.18-2.20, other models have included subradiant and SR effects by a spin model using Green's functions and eliminating the cavity field as a degree of freedom [18], however on a scale of 20 atoms in one dimension. Another approach has accounted for SR effects in a 3D ensemble of 400 atoms by accounting for the interference effects of spontaneous emission on the atoms in pairs [19]. Yet another approach based on the full quantum master equation exploits symmetries to reduce the computational complexity from scaling exponentially with the number of atoms to N^2 [20, chap. 3]. This may be one of the most applicable approaches to our system if superradiant effects cannot be neglected, though still vastly more problematic computationally compared to the linear scaling of our semiclassical model, for an ensemble of our size. However for our ensemble the density near the ensemble center is only about 0.03 atoms/λ^3, so SR effects are unlikely to play a role, but could be identified if P_{out} is found to deviate from a linear dependence on N. These could become significant if the density were increased, for example if a second-stage MOT were installed.

Another process is superfluorescence (SF) - here the ensemble is not initially correlated, but spontaneous emission by one atom is amplified and leads to macroscopic correlation of the dipoles. In the case a high degree of coherence is established ('pure' SF), the emitted intensity scales as N^2, the pulse duration as 1/N [21] and the process can leave the entire population in the ground state [22, p. 4153]. However, the intensity can also scale with N for 'non-pure' SF, with a gradual transition to the regime of amplified spontaneous emission (ASE) [22], where spontaneous emission is amplified but does not lead to macroscopic correlation. With these conditions the simulations are in agreement with non-pure SF or ASE, but we will simply refer to the process as lasing.

3.3.8 Dependence on Temperature

The temperature determines the velocity distribution, so this has big consequences for the dynamics. If the temperature is too high, there will be few atoms with a Doppler detuning corresponding to the cavity resonance, so the ensemble will not be able to initiate the lasing process. If the temperature is sufficiently low, the ensemble will be able to build up a cavity field intense enough that the majority of the atoms will interact with it during the lasing pulse, and the lasing efficiency will be optimal. Between these two cases there is a range of temperatures where the output power increases for a lower temperature. Of special interest to our system is also the μK range of temperatures, which can be achieved with second-stage cooling on the $^1S_0$ - $^3P_1$ transition [23, p. 3], however this would also change parameters such as N and R. Therefore the potential of second-stage cooling is investigated separately in Section 6.2.

The dynamics of the cavity output power and intra-waist population obtained from simulations with varying temperature are shown in Fig. 3.40 and 3.41.

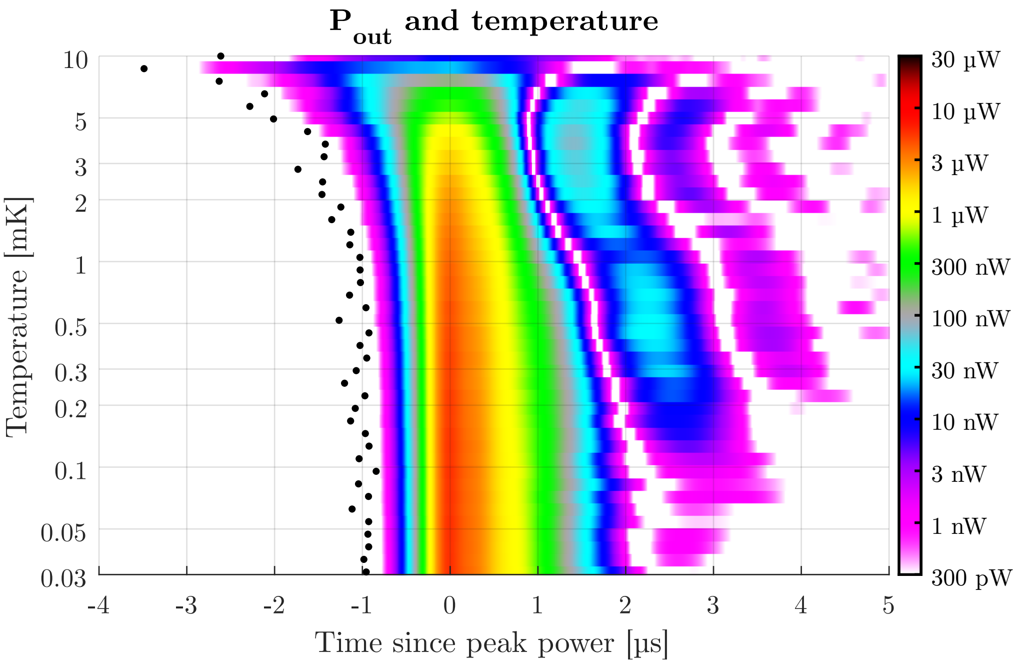

Figure 3.40: *Time evolution of the cavity output power for different temperatures. Black dots: end of pump pulse. The peak output power increases for lower temperatures. Ringings in the cavity output power are prominent for two temperature ranges (2-5 mK and 0.3-1 mK).*

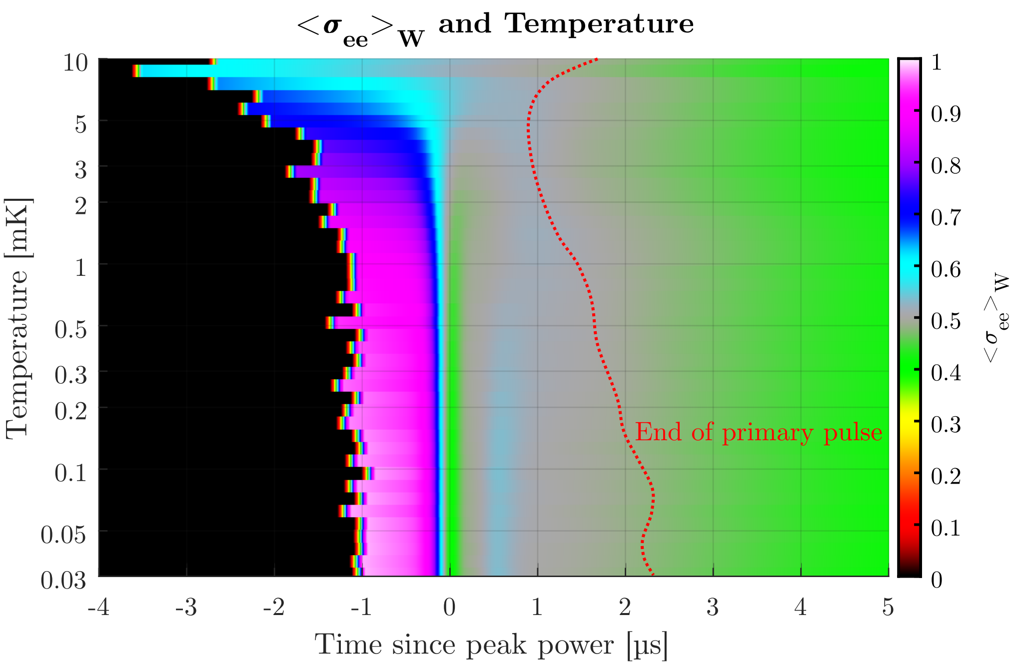

Figure 3.41: *Intra-waist population dynamics for different ensemble temperatures. Higher fractional excited population is obtained after the pump pulse for lower temperatures, and multiple Rabi oscillations become prominent during the lasing process.*

We find that the output power is indeed higher for lower temperatures, as expected based on having a more narrow velocity distribution, enabling more atoms to interact with the cavity field. However a part of the reason is also that the obtained fractional excited population after the pump pulse is higher for lower temperatures - for example increasing $\langle\sigma_{ee}\rangle$ by 0.1 has a similar effect to increasing the number of atoms by 10 %, neglecting the effects of absorption. We also see that for temperatures below 0.5 mK, the intra-cavity population will undergo more than a full Rabi oscillation during the primary pulse process. Similarly as we saw for the dependence on the number of atoms, we see there are two temperature ranges where ringings in the cavity output power are more prominent: From 2 to 5 mK and from 0.3 to 1 mK, and again they appear to be correlated with the Rabi oscillations seen in intra-waist population during the primary lasing pulse - the higher the fractional excited population is at the end of the primary pulse, the larger the secondary lasing pulse generally is. The dependence of the primary and secondary peak output power on the temperature are shown in Fig. 3.42.

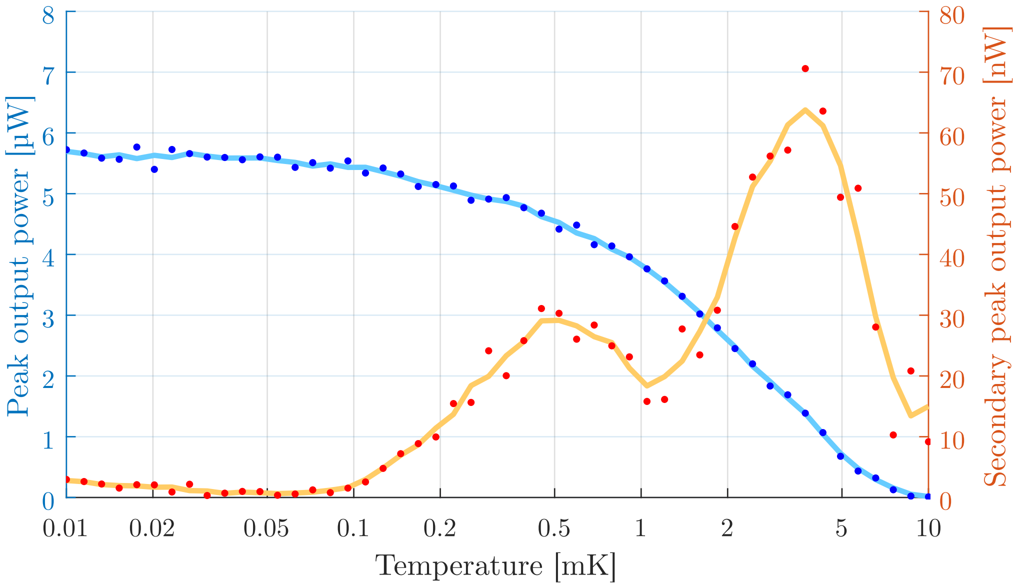

Figure 3.42: *Left axis: peak output power, depending on the temperature (blue). Right axis: peak power of the secondary pulse (red). Points: simulations, lines: running mean. We see that for lower temperatures, the peak output power increases until the point where even the fastest atoms are able to interact with the field. The secondary peak power depends on the ensemble Rabi oscillations during the primary lasing pulse.*

3.3.9 Dynamics With a Seed Laser

We found in Section 3.2.3 that if the seed laser is on, the intra-waist excitation probability will generally be lower after a pump pulse. In Figure 3.43 and 3.44 we show the simulated dynamics of the cavity output power and atomic populations depending on the seed laser power. In these simulations the ensemble starts in the ground state and evolves for 30 μs only with the seed laser on. Then the intra-waist atoms are maximally excited by a t_{π}^{W} pump pulse, and we investigate the lasing dynamics. Since the origin of the cavity field is the seed laser, the system will act as a slave laser in this case, and the cavity output will inherit the frequency of the seed laser.

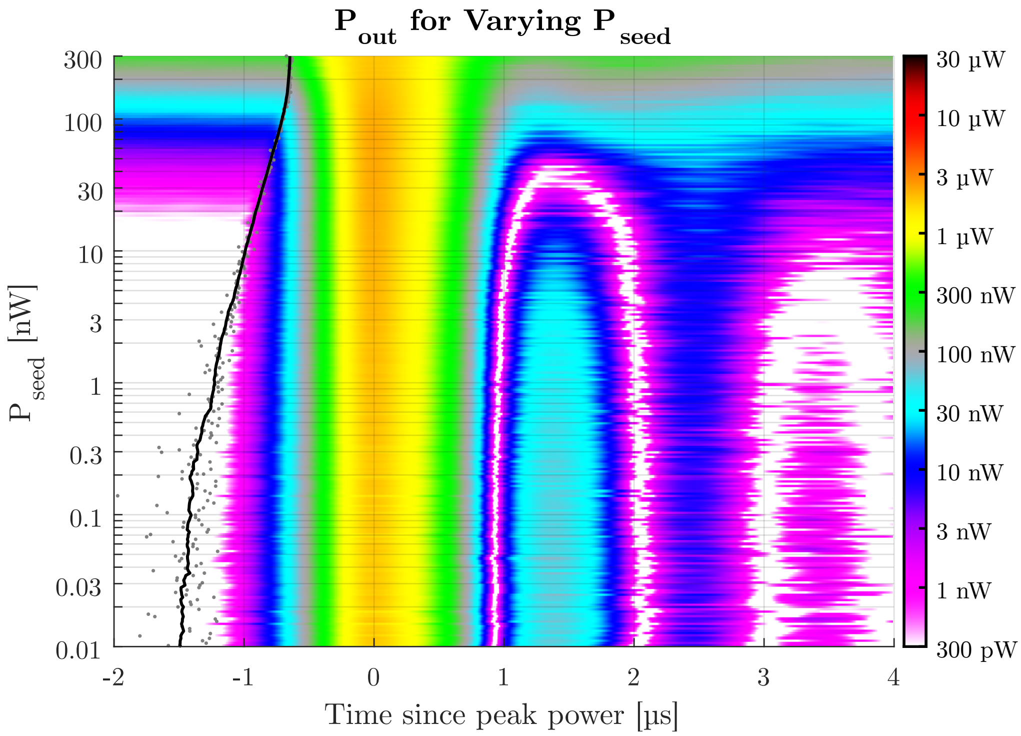

Figure 3.43: *Time evolution of the cavity output power for varying seed laser power. The ensemble evolves for 30 μs before the pump pulse is turned on. A higher seed laser power leads to a shorter delay before the lasing process begins, and a higher peak output power for $P_{seed} < 50\,nW$.*

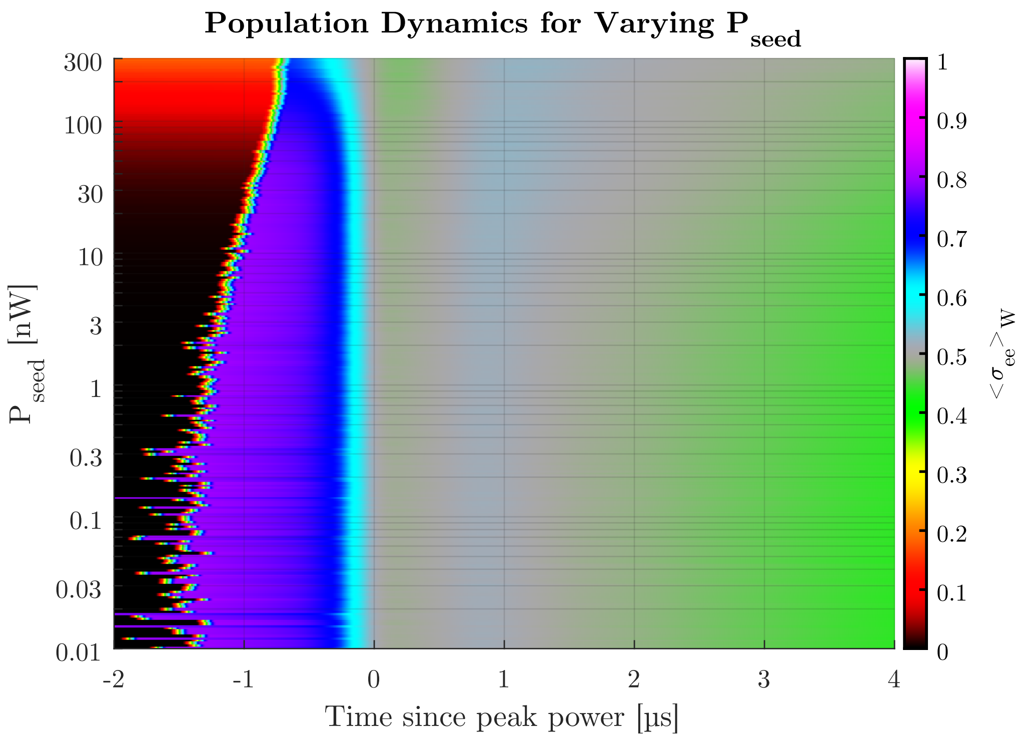

Figure 3.44: *Intra-waist population dynamics for varying seed laser power. For higher seed laser power, a lower fractional excited population is obtained after the pump pulse ends, and we see fewer atoms contribute to the lasing process - the transition from high to low $\langle \sigma_{ee}^W \rangle$ is more gradual during lasing.*

In Fig. 3.45 we show the relations between the primary and secondary peak cavity output power, and the delay between the pump pulse and primary lasing pulse peak power.

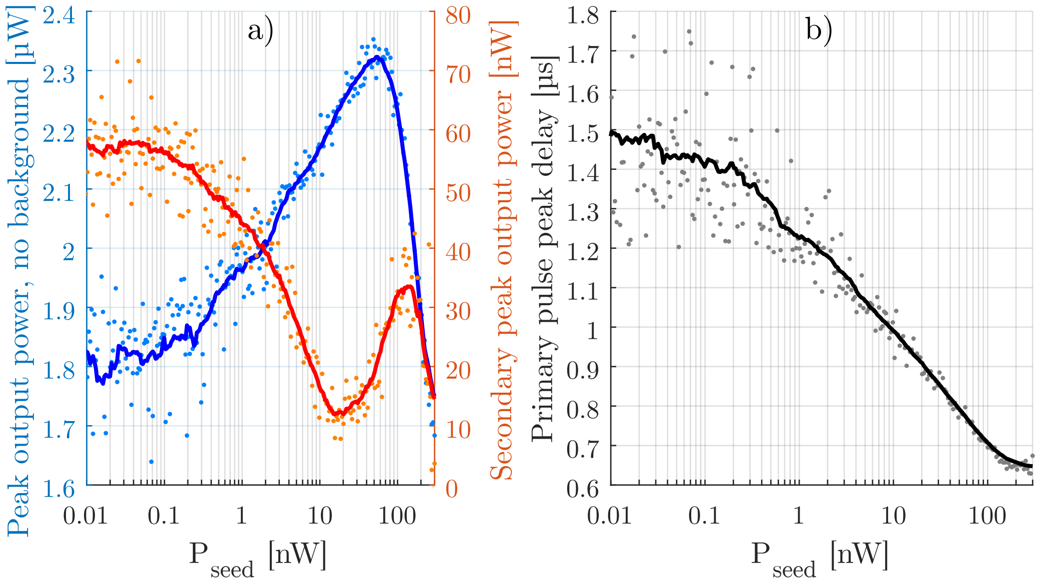

Figure 3.45: ***a)*** *The peak output power (left axis, blue) and secondary peak output power (right axis, red) depending on the seed laser power. The background P_{out} at the time of the pump pulse has been subtracted. For a seed laser power above 50 nW the primary peak decreases due to lower excitation probabilities.* ***b)*** *The relation between seed laser power and the delay of the primary lasing pulse. Even very low power levels cause the lasing pulse to build up significantly faster.*

For a seed laser power up to 50 nW, the lasing pulse peak power increases as the intra-cavity field enables the excited atoms to couple to the field, helping the lasing process to start. For a power above 50 nW, we see on Fig. 3.44 that the fractional excited population within the cavity waist is significantly reduced after the pump pulse, which explains why the lasing peak power decreases for a seed laser power above 50 nW when subtracting the background.

The exact value where the lasing peak output power is maximized depends on many parameters. The fact that we chose 30 μs as the time between the start of the simulation and the pump pulse has an influence because of atom-cavity field dynamics on this timescale. For a high seed laser power, the atoms, initially in the ground state, will initially absorb many of the seed laser photons entering the cavity mode. As more and more atoms are driven to the excited state, stimulated emission becomes more common versus absorption, and the intra-cavity field can intensify until it reaches an equilibrium with the atoms. This timescale varies, depending on the number of atoms and the seed laser power. Generally, the lower the seed laser power is, and/or the higher the number of atoms, the longer it will take for the cavity field to reach an equilibrium with the atomic population, with an upper bound of these timescales being on the order of $1/\Gamma$. If the seed laser power (and thus number of photons) is sufficiently low compared to the number of atoms, the atoms will tend to spontaneously emit any photon they absorb before they encounter a new one, which means $P_{out} < P_{in}$ in the steady state. Then the fractional excited population is approximately constant at 0, which means the equilibrium timescale lowers to the order of κ. These effects could possibly be used to estimate the number of atoms within the cavity waist experimentally. The result can be seen in Fig. 3.43 in that the output power is not equal to the seed laser power at the time of the pump pulse, especially for lower seed laser power. Therefore if the delay between the end of the MOT lasers and the time of the pump pulse is increased, the optimal seed laser power will generally be lowered for maximizing the lasing pulse peak power.

We see that the lower the seed laser power, the longer is the delay between the pump pulse and the peak output power. This is because for higher seed laser power, the intra-cavity field driven by the laser stimulates emission as soon as the ensemble is excited by the pump pulse, so the lasing pulse builds up more quickly. Recalling Fig. 3.26, we can think of the lasing process starting somewhere between point a and b, where a significant number of atoms already couple to the field, and skipping the part of the process to the left of this starting point. As the seed laser power approaches 0.01 nW, the behavior starts to resemble that without a seed laser, with delays of 1.5 μs and peak output power of 1.8 μW. A P_{seed} of 0.01 nW corresponds to an intra-cavity field of just 9 photons in a steady state where spontaneous emission is neglected. Spontaneous emission from absorbing atoms leads to dissipation of the intra-cavity field in the steady state, and in the simulations accounting for this we find that the mean number of photons is on the order of 0.1 present in the cavity mode at the time of the pump pulse.

3.4 The MOT Beam Interaction

For a more complete description of the ensemble dynamics, the interactions with the MOT beams could also be included. The MOT beams couple the $^1S_0$ and $^1P_1$ levels. The Hamiltonian describing the interaction between the atoms and the six MOT beams is given by:

$$H_{ic} = \sum_{i=1}^{Ng} \sum_{b=1}^{6} \hbar \frac{\chi_c^{b,i}}{2} \left(\sigma_{gc}^i + \sigma_{cg}^i\right) \left(e^{i\vec{k}_c^b \cdot \vec{r}_i - i\omega_c^b t} + e^{-i\vec{k}_c^b \cdot \vec{r}_i + i\omega_c^b t}\right) \tag{3.10}$$

Where we have now a sum over the atomic groups and a sum with terms for each MOT laser. The beams may again modeled as classical fields due to their high intensity in the mW range. The primary effect of this interaction on the ensemble is that it introduces decoherence. Furthermore we know the decay rate Γ_{cg} is very high compared to the ns to μs timescales we are interested in. This justifies that we run simulations with the ensemble starting fully in the ground state and without any coherence after the MOT lasers are turned off.

3.5 Summary of Simulated Dynamics

We have investigated the effects of different parameters on the ensemble dynamics during the pump pulse process. Notable results include that we need on the order of 100 mW of pump pulse power to obtain a fractional excited population above 0.7 within the cavity waist and that creating a significant inversion is unfeasible with the 20 mW of our setup of 2016. We have seen how the temperature strongly affects the population dynamics in the range of 1-10 mK, but that we can excite almost 100 % of the atoms if we can reduce the temperatures below 0.1 mK. We have also shown how the beam profile of the pump pulse can be elongated along the cavity axis to optimize the fractional excited population to about 83 % within the cavity waist, with $W_{py} \approx 0.75$ mm and $W_{pxz} \approx 2.3$ mm. This demands very short pump pulses which are experimentally challenging, and we have investigated the effects of the transient behavior of the AOM which the pump beam passes through, concluding that the most feasible experimental solution is to use slightly larger waists than optimal for the pump pulse. We have also investigated how a pump pulse aligned closer to the cavity axis can preferentially excite the atoms moving slowly along the cavity axis, which may be an advantage to obtain a more stable frequency.

In studying the lasing dynamics of the ensemble we saw how different approximations can improve performance but bias the results, of which especially the atomic group approximation proves to be problematic. In this work we have run simulations with 20-200 atomic groups due to limited computational resources, which may bias the cavity peak output power and delay by up to 50 % in the worst case scenario. Regarding the lasing dynamics, we have studied the influence of the cavity detuning on the dynamics in detail to gain insight into the process. This includes how the Rabi oscillations during the primary lasing pulse influence the secondary and higher order pulses, and how a detuned cavity can lead to more synchronized oscillations among atoms with different velocities along the cavity axis, which can promote higher order pulses. We have also studied how the dynamics depend on the spatial distribution of the atoms, and the influence which an elongated pump pulse can have on the lasing process, leading to absorption in the atoms furthest from the cavity axis. We have used the model to predict the optimal pump pulse waists for optimizing the lasing pulse peak power, finding $W_{py} \approx 1.0$ mm and $W_{pxz} \approx 2.4$ mm for an ensemble radius R = 0.8 mm, slightly larger than predicted for exciting the cavity waist population for R = 1.0 mm. Using this elliptical beam profile elongated along the cavity axis, the peak power of the primary lasing pulse may be increased by up to 50 % compared to a circular beam profile.

We have studied how the number of atoms in the ensemble influences the lasing dynamics. There is a threshold population of about 20 million atoms required in order for the process to begin, and for a low number of atoms, a big fraction will not participate in the process, as the cavity field does not become sufficiently intense for all the velocity classes and atoms far from the cavity axis to interact with the field. If the number of atoms is above 100 million, the lasing process is optimal and the peak output power depends linearly on the number of atoms. We also find that the output power strongly depends on the temperature, with a factor $\sim$3 increase if the atoms can be cooled below 0.1 mK, and little to gain at lower temperatures. Finally we studied how a seed laser influences the lasing dynamics - shortening the delay before the lasing process begins and affecting the peak output power. We predict an optimal $P_{seed} \approx 40$ nW to maximize the peak output power due to how the pump pulse affects the atoms being driven by the intra-cavity field by the seed laser.

CHAPTER 4

Upgrading the Pump Pulse

In Sec. 3.2.1 we found that the pump pulse must have a high intensity in order for us to obtain an inversion in the ensemble. Our experimental setup of 2016 was only capable of supplying 20 mW pump pulses, however. As a result, we observed ensemble fractional excited populations of up to 28 % in our experiments at the time, and a seed laser was required to drive the cavity in order to observe lasing. The two most viable ways to improve the setup and obtain higher fractional excited populations both required more power: Either by simply amplifying the existing pump pulse power, or by further reducing the ensemble temperature by installing a second MOT for cooling on the $^1S_0$ - $^3P_1$ transition (a red MOT). The red MOT would then also require power in competition with the pump pulse. Therefore we set up a tapered amplifier, upgrading the available pump pulse power to above 100 mW. This section describes the changes to the setup that were made while upgrading the pump pulse power.

4.1 Overview of the Pump Pulse Setup

An overview of the upgraded setup for the pump pulse is shown in Fig. 4.1. Here Slave Diode 2 is injected using light from Slave Diode 1, and the output beam shape from Slave 2 is then optimized for maximum gain in the tapered amplifier using a cylinder telescope and an aspherical lens. An aspherical lens at the TA output side reduces the divergence and collimates the beam horizontally - the vertical beam axis is then collimated using a cylinder telescope, which also ensures similar beam waists along both axes.

Since retroreflected light can damage the TA, the lenses are set up with a slight angle to redirect reflected light away from the gain medium, and an optical isolator is installed after the beam collimation lenses. A half-wave plate and polarizing beam spliter (PBS) allows us to control the distribution of power between the pump pulse and a beam reserved for a future red MOT, which is the component reflected by the PBS. Since the red MOT has not been built, we run experiments with maximal transmission through the PBS. For the pump beam, an acousto-optical modulator (AOM) divides the beam into different orders when a radio frequency (RF) signal is applied. The n = -1 order has the correct frequency to interact with the atoms, and we use this for the pump pulse. A telescope is built around the AOM to minimize the beam waist within it. Finally, a telescope enlarges the beam waists before reaching the ensemble. A translation state is set up for a beam profiler so that when a mirror is flipped, the beam is reflected onto the beam profiler to measure the waists.

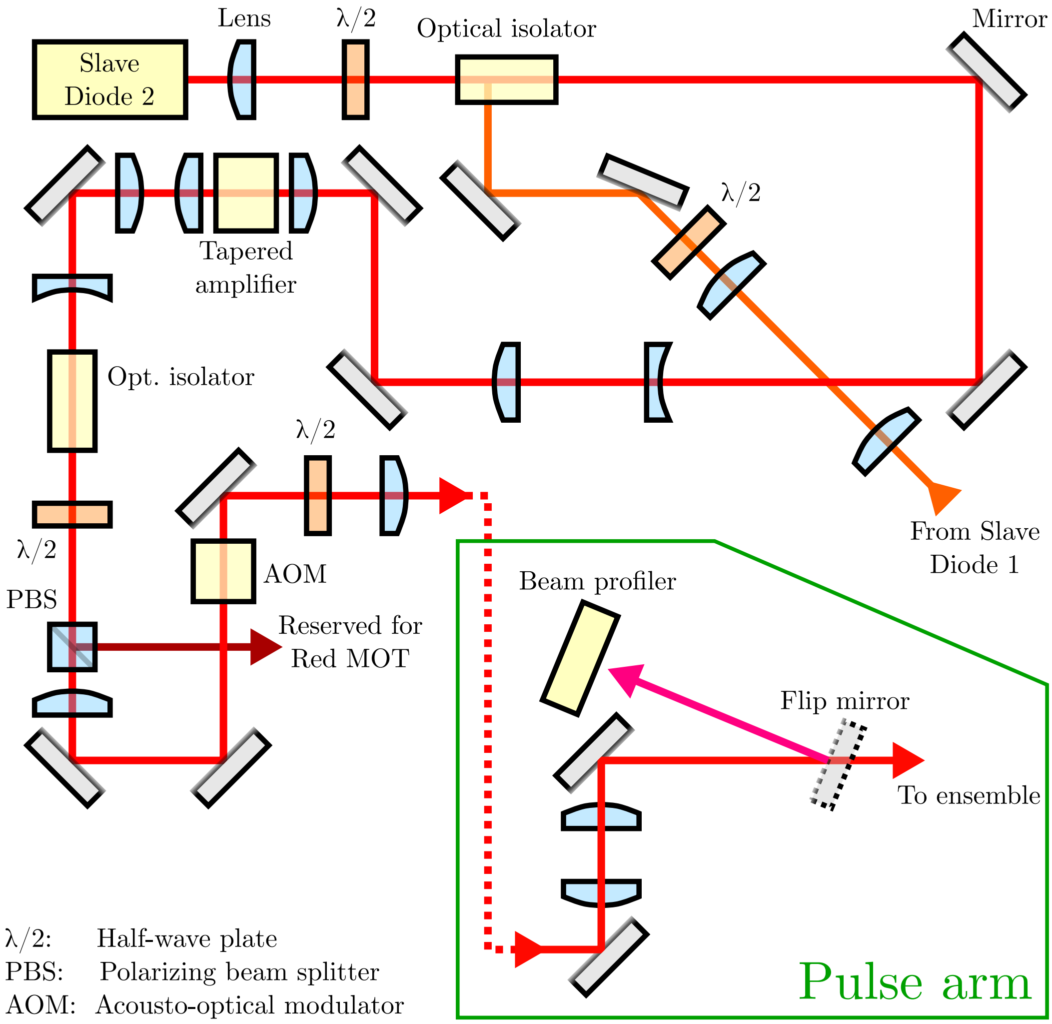

Figure 4.1: *Overview of the part of the experimental setup used for the pump pulse.*

4.2 Injecting the Slave Diode

Our reference laser cannot supply enough power for all of our experiment. Therefore it is amplified by two slave diodes: First Slave 1, and then Slave 2, which amplifies some of the light from Slave 1. The tapered amplifier then further amplifies the light from Slave 2. In order for the light to have the same frequency as the reference laser, the slave diodes must be injected by sending a faint beam into them with the reference laser frequency. This light is then amplified by stimulated emission. Furthermore there is a narrow range of parameters where the diode will be injected, depending on the diode current and temperature. To determine the best diode current for stable injection one can modulate the diode current by a sawtooth

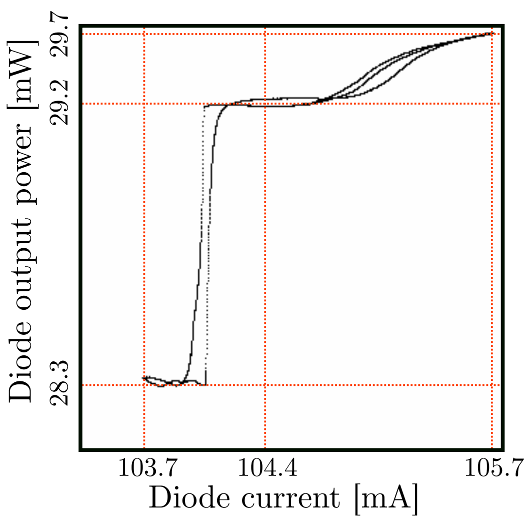

Figure 4.2: *The output power of Slave 2 as a function of the diode current. The diode is injected for currents close to 104.4 mA.*

voltage signal. This makes the diode current increase and decrease linearly in time between two values. By measuring the output power of the diode as a function of the voltage signal representing the diode current, we obtain a plot such as that of Fig. 4.2. When the diode is not injected, the output power will rise linearly with current, but when it is injected, it forms a plateau, as seen around 104.4 mA. We run the experiments with the diode injected near 104 mA, giving about 29 mW of power from the diode. There is a second plateau at 96 mA which yields 23 mW output power, but which is more stable and was used prior to setting up the TA.

4.3 The Tapered Amplifier

The tapered amplifier we use is an Eagleyard EYP-TPA-0690-00500-2003-CMT02-0000 [24], which requires 10-50 mW of input power and is capable of delivering up to 600 mW output given a current of 1.2 mA and an optimal input beam profile. However, for high currents a lot of heat will be deposited in the TA, causing its performance to degrade over time. For this reason we decided to use an operating current of 800 mA. To limit the degradation from heat we installed a heat sink connected to a peltier element at the TA and stabilized the temperature to the optimum of 25° C, for which three bachelor students deserve credit - Mikkel Ibsen, Mads Tønnes and Christian Bærentsen. They also set up the wiring for controlling the TA and peltier currents.

The TA is a tiny chip with a gain medium, tapered on the exit side. The input aperture size is only 3 μm, and to amplify the light from Slave 2, the beam of Slave 2 must be focused into the aperture with the right divergence. The method for optimizing the input beam for the TA is to turn on a small current - this makes the gain medium amplify any spontaneous emission within it, known as ASE. Then the task is to make the beam into the TA overlap as precisely as possible with the ASE out of the input end of the TA - ideally having the same divergence and beam profile. For this we use the optics shown in Fig. 4.1 between the optical isolator protecting Slave 2 and the TA: a cylinder telescope and an aspherical lens for focusing the input beam into the aperture. Two mirrors are set up as close as possible to the TA to provide two degrees of freedom for alignment.

4.3.1 Performance

The performance of the tapered amplifier varies strongly with temperature and the input beam profile, and also depends on the injection of Slave 2 - when injected, the TA performance is reduced on the order of 5 %. Even though the temperature is stabilized, there is a thermal transient behavior on the scale of minutes affecting the efficiency - the copper block beneath the TA may change density as it heats up when the TA is turned on, moving the TA slightly, which becomes significant due to the μm precision required for the input beam. The performance for 18 mW of input power is shown in Fig. 4.3. In these measurements, Slave 2 was not injected, and the measurements were taken at the beginning of the thermal transient behavior. The output power was not far below the specifications for the given input power, but the input beam profile could possibly be optimized further. For this reason a large amount of space for additional optics has been left in the setup between Slave 2 and the tapered amplifier. With Slave 2 injected and 26±3 mW of input power a steady state output power of (330±30) mW has been obtained at the beginning of operation in March 2018.

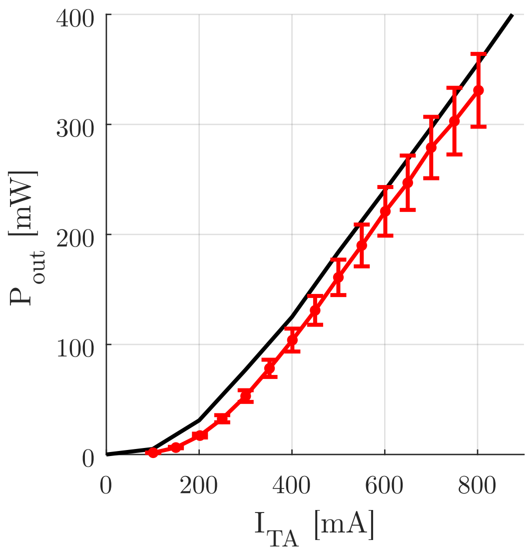

Figure 4.3: *Performance measurements of the tapered amplifier. Black: Specifications for 25° C, 18 mW input. Red: Measured output power for 18±2 mW input.*

An optical isolator has been installed to protect the TA from back-reflected light. The specified transmitted power is 88.8 % and isolation (39±1) dB, while the measured transmission and isolation are (91.8±0.01) % and (44±1) dB, respectively. The AOM further reduces the amount of power available for the pump pulse: The specified deflection efficiency is 70 to 90 %, depending on the beam waist size, and experimental efficiencies of about 75 % have been measured. Generally a smaller waist leads to a lower deflection efficiency.

4.4 Transient Behavior of the AOM

An acousto-optical modulator (AOM) uses a radio-frequency (RF) signal to control a piezoelectric transducer, which generates sound waves in the material which the laser beam passes through. These sound/density waves periodically modulate the index of refraction in the material, scattering the laser beam into different orders n with frequencies shifted by $n \cdot \nu_{RF}$, depending on the beam angle and the applied frequency ν_{RF}, which we control. The way we turn the pulse on or off in the experimental cycle is by turning the RF signal applied to the AOM on or off. When the signal is off, the AOM does not scatter light into higher orders, so there is no light at a frequency the atoms can interact with. When the RF signal is on, some of the light is scattered into the order n = -1, which we use for the pulse. Changing the sound waves within the material is not an instant process, and this gives rise to the transient behavior when we turn the pump pulse on and off.

The AOM used in this part of our setup is an ISOMET Model 1201E-1 [25], with a specified rise time of 46 ns for a Gaussian beam with a diameter of 0.25 mm. The rise time is defined as the time it takes for the sound wave to propagate 0.65 times the $1/e^2$ beam diameter [26, p. 5]. The smaller the beam waist is within the AOM, the less the sound waves will vary over the beam path, and the faster the deflected beam components can be switched on/off. Ideally the beam divergence is also low, so the beam width does not change size within the AOM. To minimize the transient effects, we built a 1:1 telescope around the AOM, which reduced τ from 29^{+1}_{-2} ns to 11^{+3}_{-2} ns. Measurements of the transient behavior after optimization can be seen in Fig. 4.4. There is a notable spike in power before the turn-off, which is not included in our model, and means that the closing time is faster than the opening time. We obtain the value for τ by a fit using Eq. 4.1 (previously described in Section 3.2.6), and the uncertainty on τ by the difference to the τ values obtained if fitting to either the opening or closing transient individually. The photodetector voltages (representing intensity) have been normalized to the values at the plateau in order to fit the functions.

$$P_p(t) = P_p^0 \cdot \frac{1}{1+\exp\left[(t_O - t)/\tau\right]} \cdot \frac{1}{1+\exp\left[-(t_C - t)/\tau\right]} \tag{4.1}$$

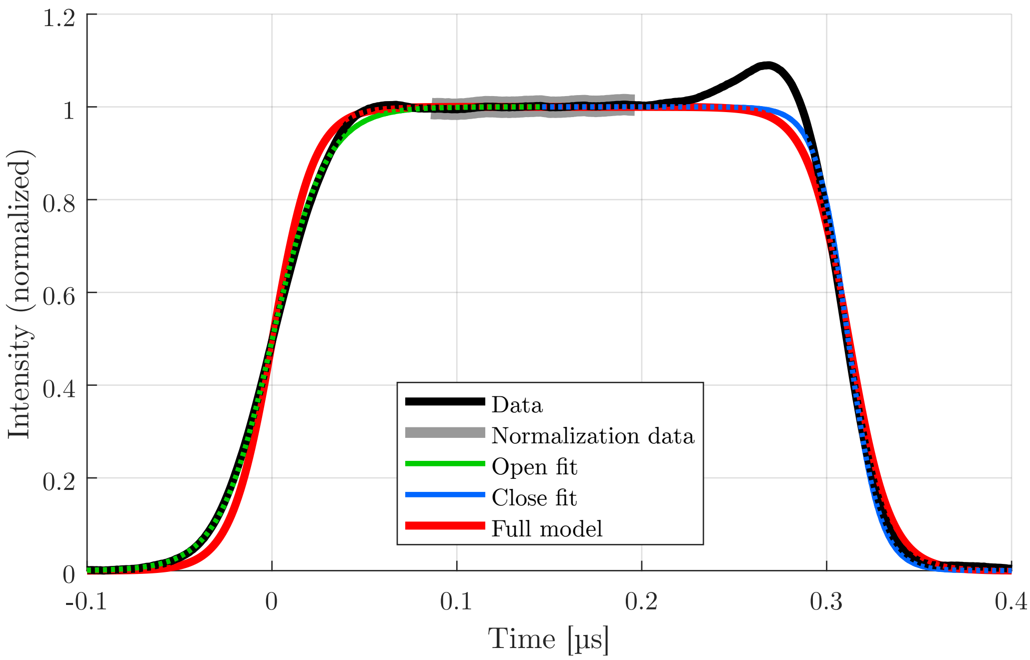

Figure 4.4: *A measurement of the power out of the AOM after optimizing the transient time τ to 11^{+3}_{-2} ns, here fitted for the opening and closing transients separately, and with a full, combined model. The full model is given by Eq. 3.6, while the open/close fits use only one of the logistic terms.*

CHAPTER 5

Experimental Results

In this section we present the experimental results related to the model. First we describe how some of the different parameters of the model were determined, and finally compare the simulation results to the experimental results. Many parameters vary between the different experimental realizations - for example, the ensemble size, temperature or position may differ based on the exact alignment and intensities of the MOT lasers. Therefore we will group the experiments based on the date they were conducted. An overview of the experimental results are shown in Table 5.1. Note the measurements of τ were described in Sec. 4.4.

Experiment	Date	Parameters determined
E1	2018-03-09	$\langle\sigma_{ee}(t)\rangle$, W_p
E2	2018-03-13	$\langle\sigma_{ee}(t)\rangle$, W_p
E3	2018-03-21	τ, W_p, R
E4	2018-03-28	N, $P_L(N, P_{seed})$, W_p, κ
E5	2018-04-13	$P_L(\Delta)$

Table 5.1: *Overview of parameters and experimental results. $\langle\sigma_{ee}(t)\rangle$ are measurements of Rabi oscillations during the pump pulse. $P_L(A)$ are measurements of the lasing pulse properties as function of variable A.*

5.1 Determining Model Parameters

5.1.1 The Number of Ensemble Atoms

To determine the number of atoms in the ensemble we apply a laser cycle as shown in Fig. 5.1, part of experiment E4. The MOT lasers are turned on shortly after the pump pulse is turned off, before the cavity field pulse builds up. When the MOT lasers are on, the fluorescence signal is proportional to the number of atoms in state $^1P_1$ and $^1S_0$, so by monitoring the fluorescence at the same time as the cavity output power (see Fig. 5.2), we can infer both what fraction of the total population changes state, and how many atoms must change state in order to produce a cavity output pulse with the detected energy. By integrating the area between the cavity

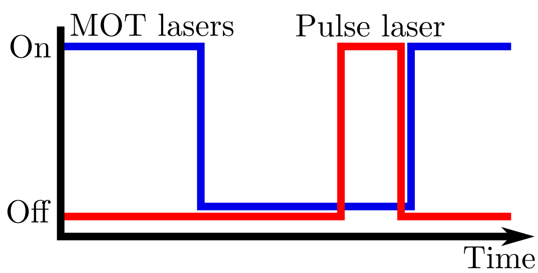

Figure 5.1: *Laser sequence for determining the number of atoms - the seed laser is on during the entire sequence. By turning on the MOT lasers before we observe the emitted pulse from the cavity, we can monitor the $^3P_1$ population at the same time as the cavity output power.*

output power and the background due to the input field, we can find the energy E emitted by the atoms into the cavity mode. Based on this, we find the observed number of emitted photons n into the cavity mode:

$$n = E/\hbar\omega = 1.41 \cdot 10^6 \tag{5.1}$$

Which corresponds to an equivalent 1.4 million atoms changing state due to the lasing process.

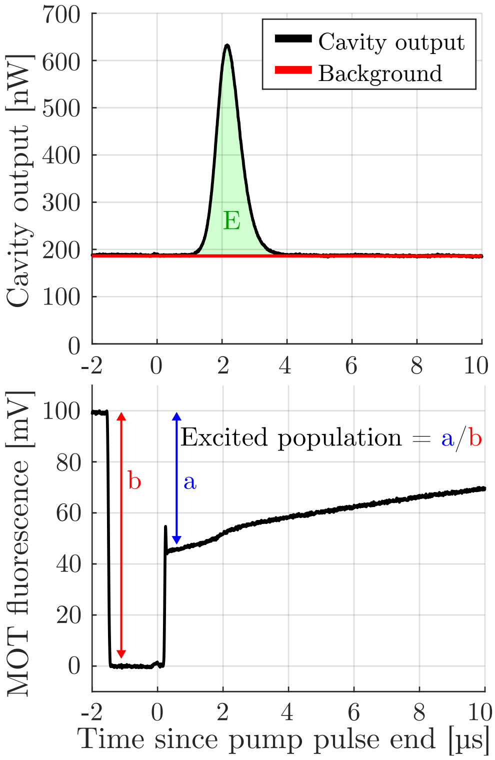

Figure 5.2: *The data from the cavity transmission (converted to power) and MOT fluorescence signals.*

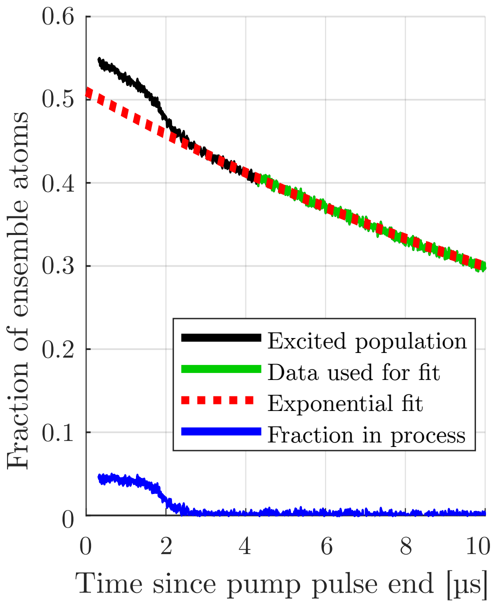

Figure 5.3: *The excited population (black) after the MOT lasers are turned on again, and exponential fit (red) to the green segment. Subtracting the fit from the excited population yields the component of the population that changes due to the lasing process (blue).*

In Fig. 5.3 we illustrate how to determine the fraction of the ensemble that participates in the lasing process. The fraction of ensemble atoms in the excited state (black) is calculated based on the method illustrated in Fig. 5.2 (lower). To find out which fraction of the total number of atoms the 1.4 million corresponds to, an exponential decay (red) is fitted to the MOT fluorescence data after the cavity pulse has ended (green). The exponential decay is due to spontaneous emission, so by subtracting this from the fluorescence signal we are left with the component of the signal (blue) that is due to the emission into the cavity mode.

There are still some fluctuations remaining after subtracting the fit (see ρ_{gg} in Fig. 5.4), which may be damped Rabi oscillations due to MOT light. The fluorescence level of 100 mV (b in Fig. 5.2) serves as reference for all atoms being in the ground state, and this is from long after any Rabi oscillations have died out. Therefore we need to also avoid that the Rabi oscillations bias our reference value for the excited population when the process begins. Based on this we use the mean excited population of the 20 data points between t = 0.76 μs and 0.91 μs in Fig. 5.3 as reference value - this yields $\rho = (4.2 \pm 0.2)$ % as the fraction of the total population that participates in the lasing process. The standard deviation is used as uncertainty due to the systematic variations. From this we find the number of atoms in the ensemble N with an uncertainty σ_N:

$$N = \frac{2n}{\rho} = \frac{2 \cdot 1.41 \cdot 10^6}{0.0423} = 66.7 \cdot 10^6 \tag{5.2}$$

$$\sigma_N = \sqrt{\left(\frac{\sigma_n}{\rho}\right)^2 + \left(\frac{n\sigma_\rho}{\rho^2}\right)^2} \tag{5.3}$$

The factor 2 stems from the fact that we only detect the output on one side of the cavity, and the atomic emission is assumed to leak equally from both mirrors. With the uncertainty on the initial population of $\sigma_\rho = 0.2$ and an uncertainty on n assumed to be dominated by a powermeter calibration uncertainty of about 10 %, the final result for the number of MOT atoms is $N = (67 \pm 8) \cdot 10^6$. However there may also be systematic uncertainties because we averaged over 1024 experimental cycles in order to reduce the signal to noise ratio. During each cycle the output pulse will occur at different times, and the power will also vary. Finally, there may be a systematic uncertainty of about 2 % due to the fact that the seed laser keeps a constant fraction of the ensemble excited, including when the MOT light is on. This would cause us to estimate a slightly too low number of atoms.

We see similar dynamics for the sum of photons emitted in the lasing process as function of time (minus the background) in Fig. 5.2, versus the participating fraction of atoms in the ground state: The photons from the process are detected with a delay of about 280 ns after the atoms participating in the process change state (see Fig. 5.4) - this is close to the cavity lifetime $\kappa^{-1} = 257$ ns.

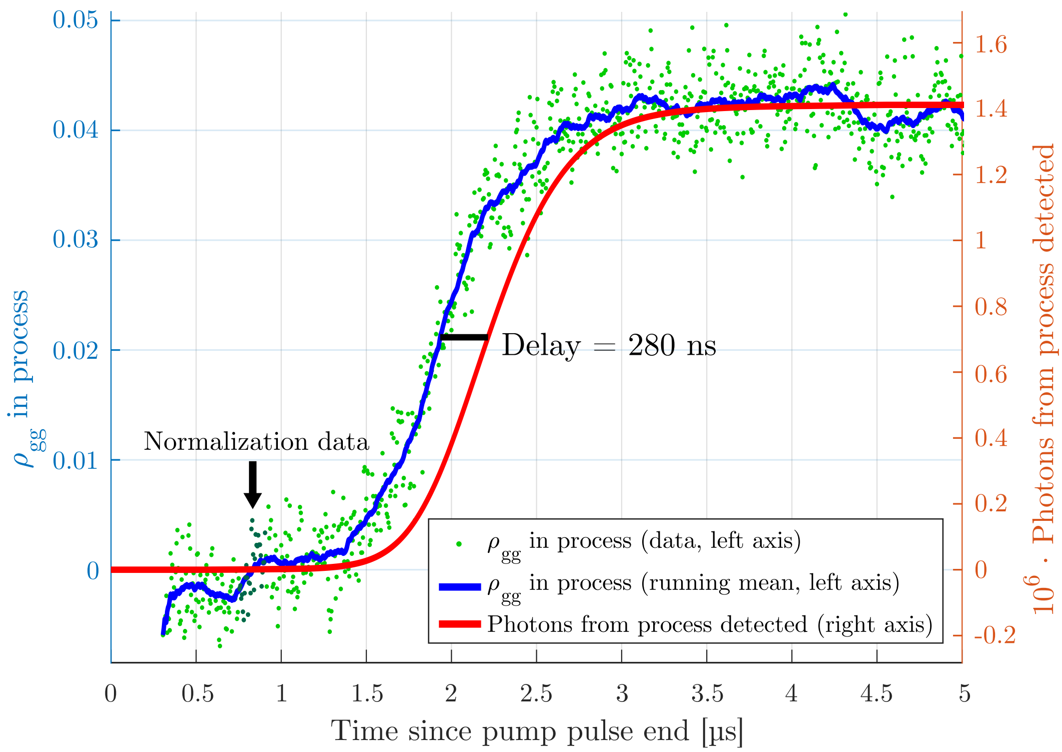

Figure 5.4: *The observed population dynamics due to the lasing pulse process are shown. About 4.2% of the ensemble population participates in the process and start in the excited state. As they build up the cavity pulse, they change state and ρ_{gg} increases (blue), as does the total number of photons emitted by the cavity (red).*

5.1.2 The Pump Pulse Beam Waists

In order to determine the waists of the pulse beam we built a setup with a translation stage and a flip mirror near the MOT chamber. The mirror can be flipped to reflect the pulse beam onto a beam profiler mounted on the translation stage. The distance between the flip mirror and the beam profiler is chosen to be approximately equal to the distance from the flip mirror to the atoms, so the error due to any beam divergence is minimized. With the translation stage, the beam profiler can be moved around on a plane perpendicular to the beam propagation direction, to measure beam waists that are big compared to the active area of the detector. Data from the beam profiler is then fitted with an elliptical Gaussian. An example of this from experiment E3 can be seen in Fig. 5.5, using an f100 lens in the telescope in the pulse arm. In E4 we obtained $W_{p1} = 2.13$ mm, $W_{p2} = 1.36$ mm and $\theta_p = 39.2\ °$.

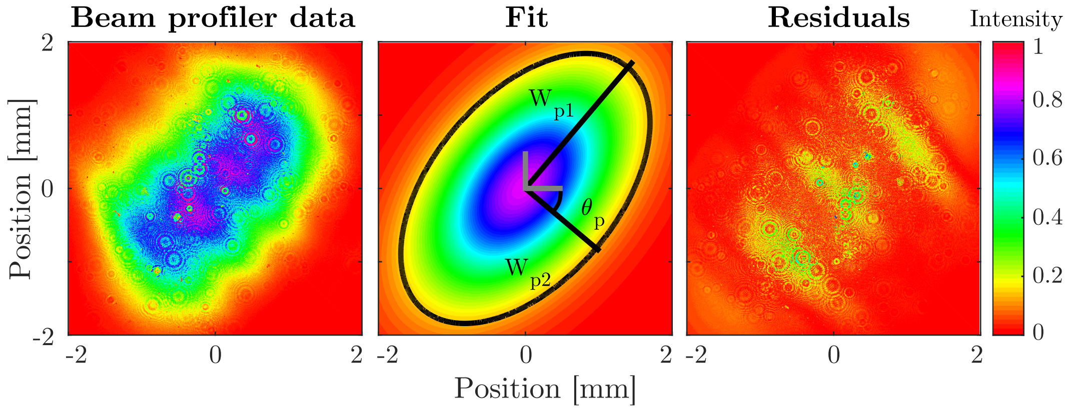

Figure 5.5: *Example of a fit to beam profiler data from experiment E3. The intensity is normalized by the peak value. $W_{p1} = 2.27$ mm and $W_{p2} = 1.33$ mm are the obtained waists, and $\theta_p = 40.2°$ the angle with respect to the y- and xz-axes, shown in gray. The residuals show the absolute difference between data and fit - circular artifacts are due to ND filter impurities.*

5.1.3 The Cavity Linewidth

The cavity linewidth represents the range of frequencies the cavity supports for each standing wave mode. It is related to the finesse and the mirror reflectivity - the higher the reflectivity, the more times a photon will statistically be reflected within the cavity before leaking (defining the finesse), and the lower the leak rate and spread in frequency - κ - is. To determine κ we measure the cavity transmission while varying the cavity length (with no ensemble present) around the resonance. We generate two sidebands at ±10 MHz the laser frequency. By looking at the cavity output power as a function of time as we scan the cavity, we can use these sidebands as rulers, as we know their peaks must be 10 MHz from the main peak. This enables us to rescale the time axis to a frequency axis and also to compensate for any linear drift in scan speed. After rescaling the axis to frequency, the linewidth is determined by fitting a function to the cavity output data. This includes a term for the background light and a sum of three Lorentzians, one for each peak:

$$P(\omega) = P_{BG} + P_0 \cdot \frac{(\kappa/2)^2}{(\omega - \omega_0)^2 + (\kappa/2)^2} + L_2 + L_3 \tag{5.4}$$

Where L_2 and L_3 represent the sideband Lorentzians. One data sample and a fit is shown in Fig. 5.6, obtained by averaging over 1024 samples on the oscilloscope.

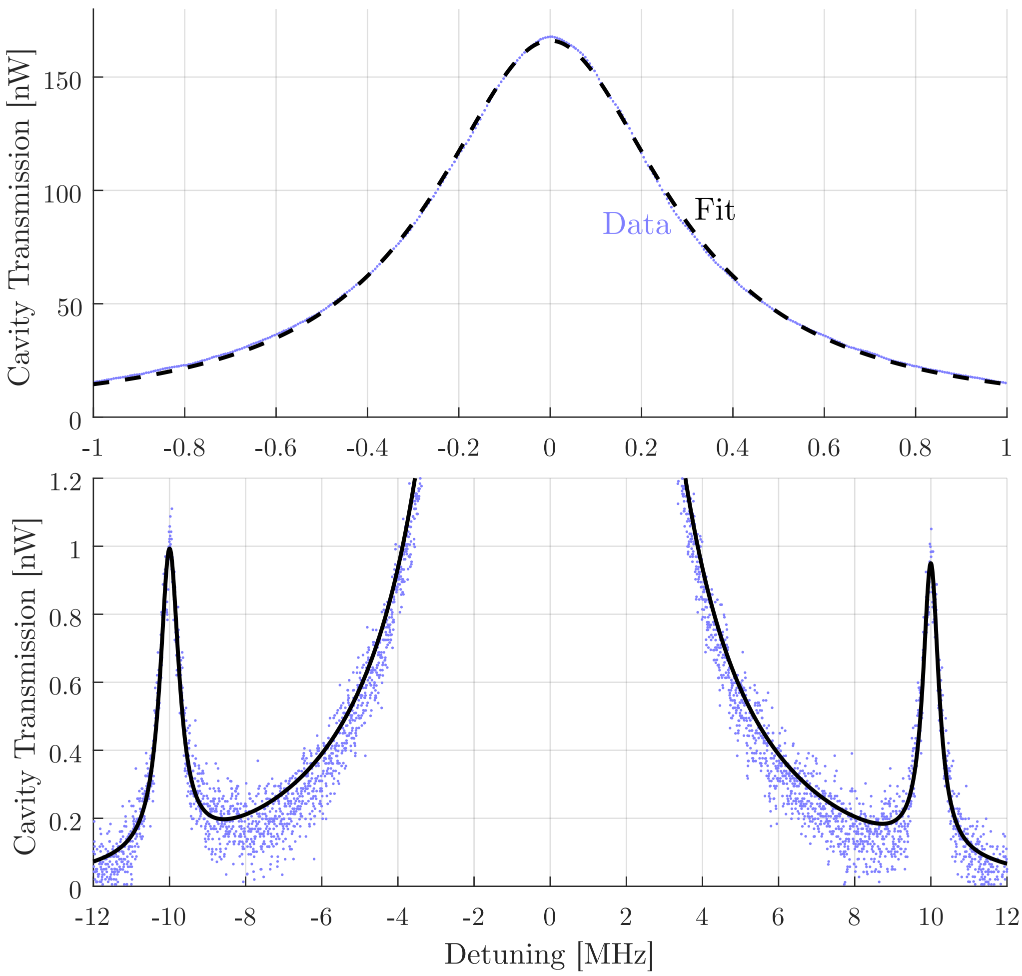

Figure 5.6: *One sample of data and a Lorentzian fit used to determine the cavity linewidth κ. This fit yields $\kappa = 2\pi\cdot$ (619.9 $\pm$ 0.8) kHz. The x axis is calibrated using the two sidebands at $\pm$10 MHz.*

Based on combining the values from fits to two different data samples from experiment E4, we obtain $\kappa = 2\pi \cdot (620.3 \pm 0.4)$ kHz.

5.1.4 The Ensemble Density Profile

We use a camera (Casio EX-ZR100 [27]) to determine the density profile of the ensemble, using the Zerodur cavity spacer dimensions [28, p. 119] for calibrating from pixels to distances. The ensemble is located near the center between the rods, so we define the uncertainty in the dimensions as half the difference between the calibrated distance based on the front and back rods. An example is shown in Fig. 5.7. We determine the density profile based on two axes on the photos, which we define as a and b. When the MOT lasers are on, the intensity of the fluorescent light emitted in all directions is proportional to the number of atoms, and if the density profile is Gaussian and the pixel values of the camera are proportional to the intensity, one can fit a Gaussian function to the pixel values. The standard deviation of the Gaussian is then equal to the density parameter R.

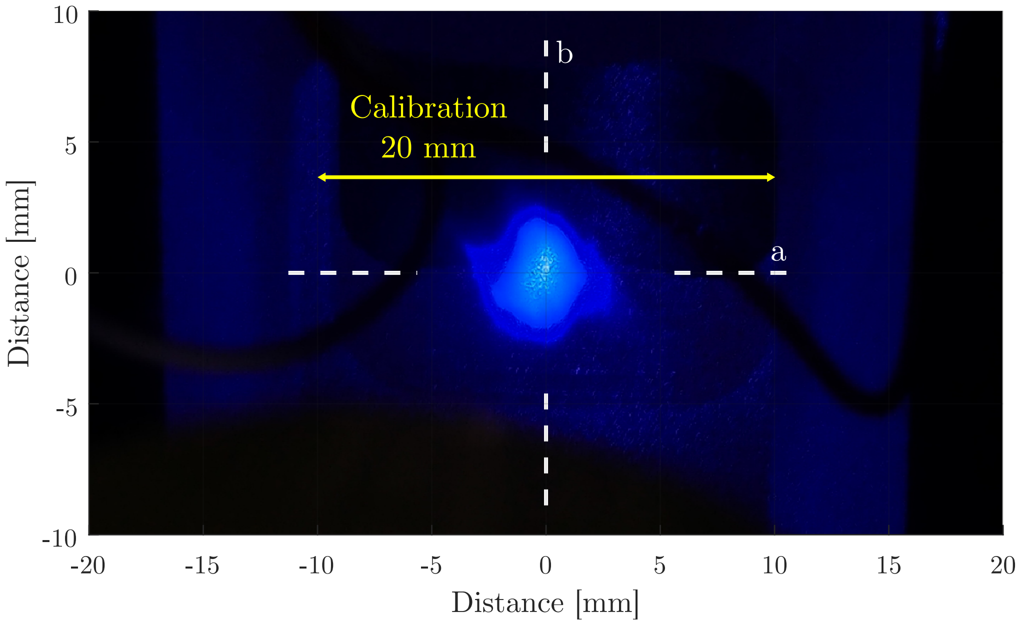

Figure 5.7: *One photo of the ensemble and part of the cavity spacer, which is used for distance calibration. The density profile is determined based on Gaussian fits to green pixel values along axis a and b.*

The blue channel tends to be saturated for exposure times that still enables us to see the rods used for distance calibration - furthermore, reflections from the rods near the ensemble create a background of blue light with pixel values about 90 in Fig. 5.7. The density profile of the most dense part of the MOT is also the most important part for the experiment, in case the outer parts may have different characteristics from the center. For these reasons we fit to the data from the green channel, shown in Fig. 5.8 for the photo of Fig. 5.7.

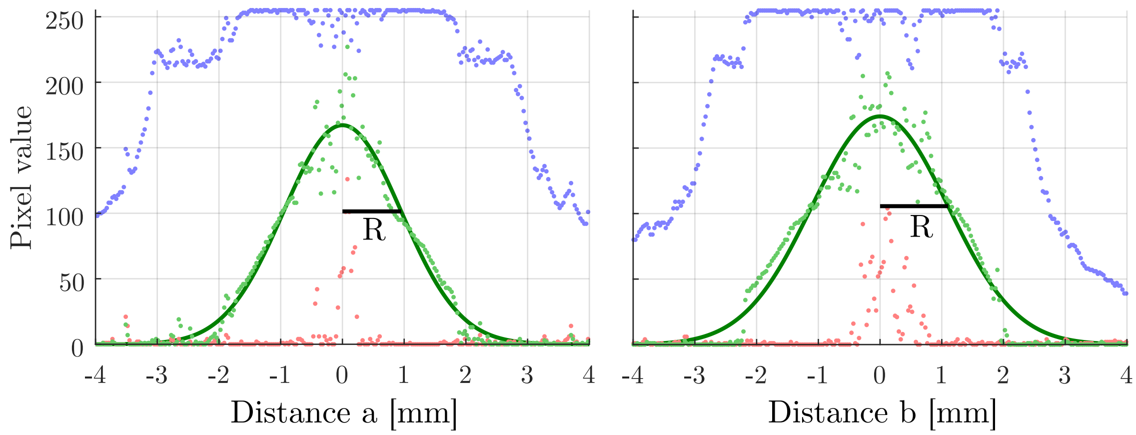

Figure 5.8: *Pixel data along axis a (left) and b (right) from part of the photo in Fig. 5.7 and Gaussian fits to the green channels. Along axis a we find R = (0.95±0.06) mm and along b we find R = (1.10±0.07) mm.*

Based on four fits using two photos, we obtain R = (1.0±0.1) mm, with the dominant uncertainty being the asymmetry of the ensemble. However, even though the approximately Gaussian profile of the pixel data suggests the pixel data does scale linearly with intensity, the camera specifications do not mention this, which adds an uncertainty. Another uncertainty is the possibility that the ensemble is out of focus on the images, which could cause our estimate of R to be too high.

5.1.5 The Temperature and Magnetic Field Offset

The two least well known parameters in the model are probably the temperature and y_{MOT}. For the temperature the Doppler cooling limit sets a definite lower bound. For the $^1S_0$ - $^1P_1$ transition it is given by [14, p. 802]:

$$T_D = \frac{\hbar\Gamma_{cg}}{2k_B} = 0.77mK \tag{5.5}$$

There are different methods to estimate the temperature which our model could also predict the outcome of. The first method is based on the time of flight: After the MOT lasers are turned off, the ensemble atoms will move in approximately ballistic paths, so the ensemble spreads out at a rate depending on the temperature. The MOT has dimensions of mm, so with m/s thermal velocities, the expansion dynamics occur on the ms timescale. When the MOT lasers are then turned on again after some milliseconds, the fluorescence signal is compared the initial fluorescence signal: Their ratio reveals how many atoms have been lost due to the expansion, and this can be compared to the simulated expansion of the ensemble for different temperatures.

PhD students in our group have previously estimated the temperature at 5 mK based on saturated spectroscopy measurements [29, p. 49], but the temperature can easily vary between different experiments depending on the MOT beam alignment and power. Other groups [30] have used a method based on probe beam absorption, which may be more accurate and is plausible if the ensemble size is well known.

Regarding y_{MOT} one can measure the energy splitting of the ^{1}S$_0$ - ^{3}P$_1$ $\Delta m = \pm 1$ transitions, which depend on the magnetic field due to the Zeeman shift. If one knows the magnetic field gradient, one can calculate the offset that the energy splitting corresponds to. This has yielded values of $y_{MOT} = 2.1$ mm, however based on year-old measurements, and the ensemble could have a different offset in our current experiments, although there should be a single value that yields optimal overlap with the cavity mode.

5.2 Pump Pulse Dynamics - Rabi Oscillations

In experiments E1 and E2 we measured the ensemble Rabi oscillations during the pump pulse. The motivation was to test the modeling of the pump pulse dynamics and to optimize the pump pulse beam profile to maximize the ensemble fractional excited population $\langle\sigma_{ee}\rangle$ based on the theory of Section 3.2.5. At this time we did not have the predictions of Section 3.3.6 and had not yet distinguished between the intra-waist population and the ensemble in the model. We calculate $\langle\sigma_{ee}\rangle$ based on measurements of the fluorescence signal as in Section 5.1.1, and by calculating $\langle\sigma_{ee}\rangle$ after the pump pulse for different pump pulse durations, the Rabi oscillations become clear. For each pump pulse duration, fluorescence data from 256-1024 experimental cycles were averaged on an oscilloscope (Rhode & Schwarz HMO3034) to reduce noise. Note this may bias the results, as coherent oscillations longer after the trigger signal (at the end of the pump pulse) are more likely to average out due to slight differences from cycle to cycle. The results are shown in Fig. 5.9.

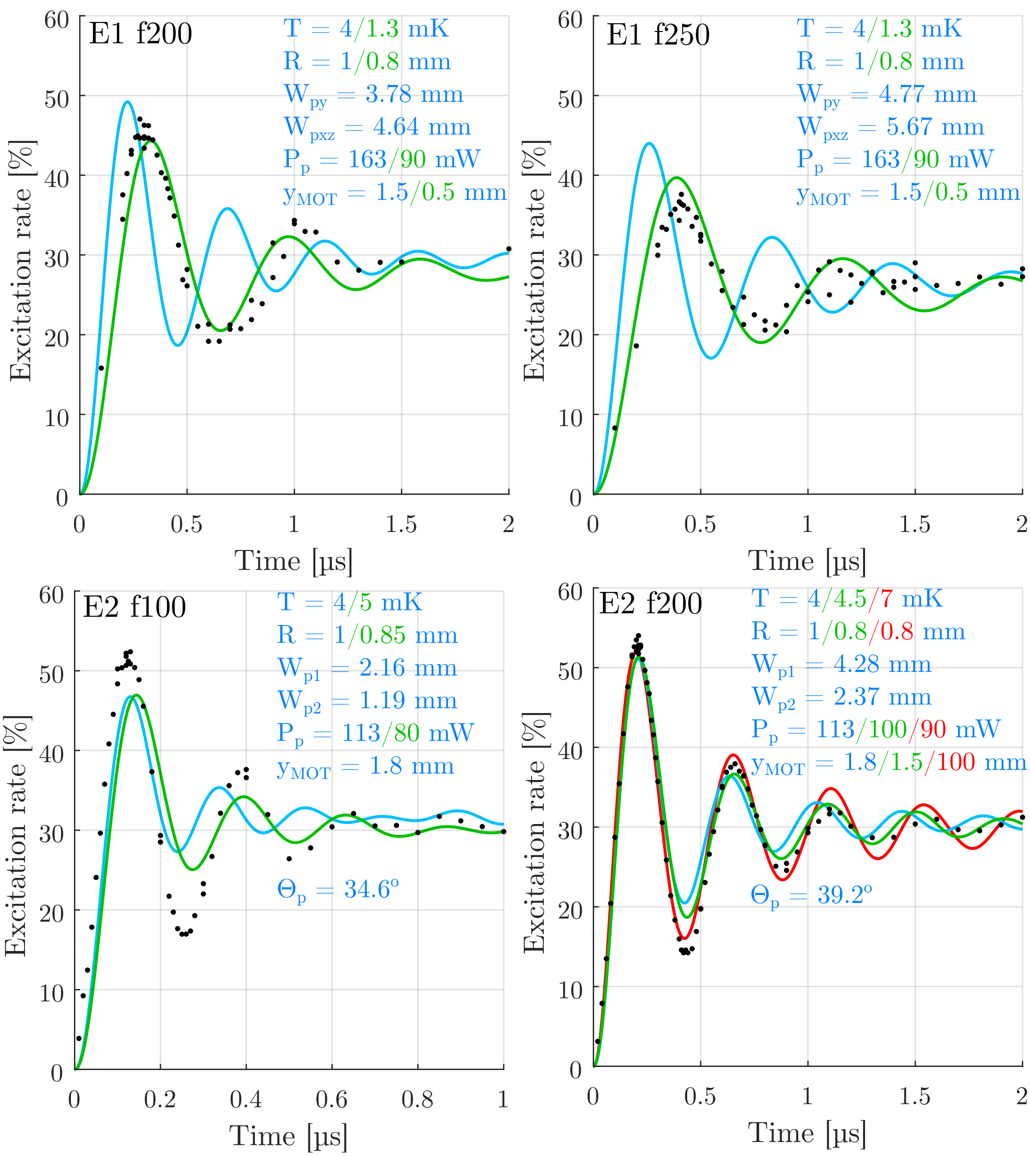

Figure 5.9: *Measurements of ensemble Rabi oscillations and comparison to simulations. The simulation parameters are shown on each figure. Blue: simulations based primarily on experimentally measured parameters, green: parameters fitted for better agreement with measurements, red: illustration of degeneracy, see main text.*

We show two simulations for each set of Rabi oscillation measurements: one set (blue) based on the experimentally measured values of all variables except T and y_{MOT} (which are not measured), and another set (green) where more parameters are varied, yielding better agreement with the Rabi oscillation measurements. The power used in the blue simulations is based on measuring the pump pulse power in front of and behind the vacuum chamber, assuming identical loss rates through the two chamber windows. The pump pulse waists and the density parameter R were determined using the methods described in Section 5.1.2 and 5.1.4 - for experiment E1 we only took measurements of the beam profile along the xz and y axes, which do not align with the beam ellipse, therefore the simulated beam shape is not as accurate in these cases. The parameters y_{MOT} and T are relatively unknown, so values were chosen which brought the simulations to closest agreement with the data. The characteristic timescales for the AOM, τ, were measured at 28 ns for E1 and 15 ns for E2, but this influence is small compared to other discrepancies and is therefore not included in the simulations.

Generally the blue simulations, except for E2 f200, do not agree very well with the observations. The biggest discrepancy for E1 is the power and/or beam waists, which the period of the Rabi oscillations primarily depends on. For E1 the Rabi oscillations cannot be brought into agreement with the theory assuming a powermeter calibration uncertainty of 10 %, as seen by the much lower power used in the green simulations. One possible explanation for the deviation is the beam profile, which was not very Gaussian due to the influence of the tapered amplifier (whose output profile approximately resembles a top hat) - this may have resulted in a lower power at the dense part of the ensemble than simulated with the Gaussian model. Another possibility could be instabilities in the output of the tapered amplifier/slave diode 2 - as mentioned in Section 4.2, the plateau at high current can be unstable, which may have caused modes with frequencies off the atomic resonance in these experiments, and a lower power for the mode on resonance than measured.

For E2 f100 both the simulations do not agree very well with the data. The observed amplitudes of the oscillations are notably larger and could suggest that the simulated waists are too small, the density parameter R is too big, or the beam profile is more uniform than the Gaussian model. However for E2 f200 the simulations are in relatively good agreement with the measurements, with the simulated parameters within plausible ranges. Here the remaining discrepancies could be due to effects such as the Gaussian beam approximation. However it is hard to put bounds on the experimental parameters due to them being degenerate. As an example we can consider the case if y_{MOT} were very large and the magnetic field had no effect on the dynamics. In this case there is still relatively good agreement between simulation and experiment (red curve in Fig. 5.9) for T = 7 mK and P_p = 90 mW when comparing the period and amplitude of the initial Rabi oscillations, though the damping of the ensemble Rabi oscillations would be slower than for a lower y_{MOT}, leading to larger discrepancies for t = 1-2 μs. For still higher temperatures one could lower R to compensate the effects on the dynamics somewhat, though this brings us further from the result of Section 5.1.4 and the discrepancies continue to increase. Thus 7 mK may be an approximate upper bound on the temperature in E2 based on the Rabi oscillations.

Regarding the lasing dynamics we found that the f100 setup of E2 yielded the most intense lasing pulses, probably due to a higher intra-waist excited population compared to the f200 setup. Therefore this setup (f25 and f100 lens in the pulse arm telescope) has been used in the experiments of Section 5.3 with some further optimizations of the MOT beams and pump pulse profile, leading to $\langle \sigma_{ee} \rangle$ of up to 0.6 observed.

5.3 Lasing Dynamics

In this section we will present results for some of the properties predicted for the lasing process in Section 3.3, starting with the dependence on the number of atoms, proceeding with how the dynamics depend on the seed laser power and finally how they depend on the cavity detuning.

5.3.1 Scaling with the Number of Atoms

In Section 3.3.7 we predicted how the lasing dynamics depend on the number of atoms. To investigate this we varied the number of atoms by adjusting the intensity of the Zeeman slower beam - for lower intensities, more atoms travel too fast to be trapped by the MOT beams, and we obtain an ensemble with fewer atoms.

We ran this experiment (which is part of E4) with 32 different approximate MOT fluorescence levels, which define 32 experimental data groups. For each group we gathered 50 data sets including MOT fluorescence and cavity output power data, so we obtained 32·50 = 1,600 data sets in total. The 32 approximate fluorescence levels were investigated in a randomly generated order to avoid systematic bias from e.g. slow drifts in MOT laser intensity. The majority of the cavity output data (limited by image resolution) is shown in Fig. 5.10, with a background of non-resonant light subtracted and the subsequent cavity output power multiplied by two due to us only detecting light from one side of the cavity. It is sorted by the number of atoms, which is calculated based on the MOT fluorescence as explained in Section 5.1.1.

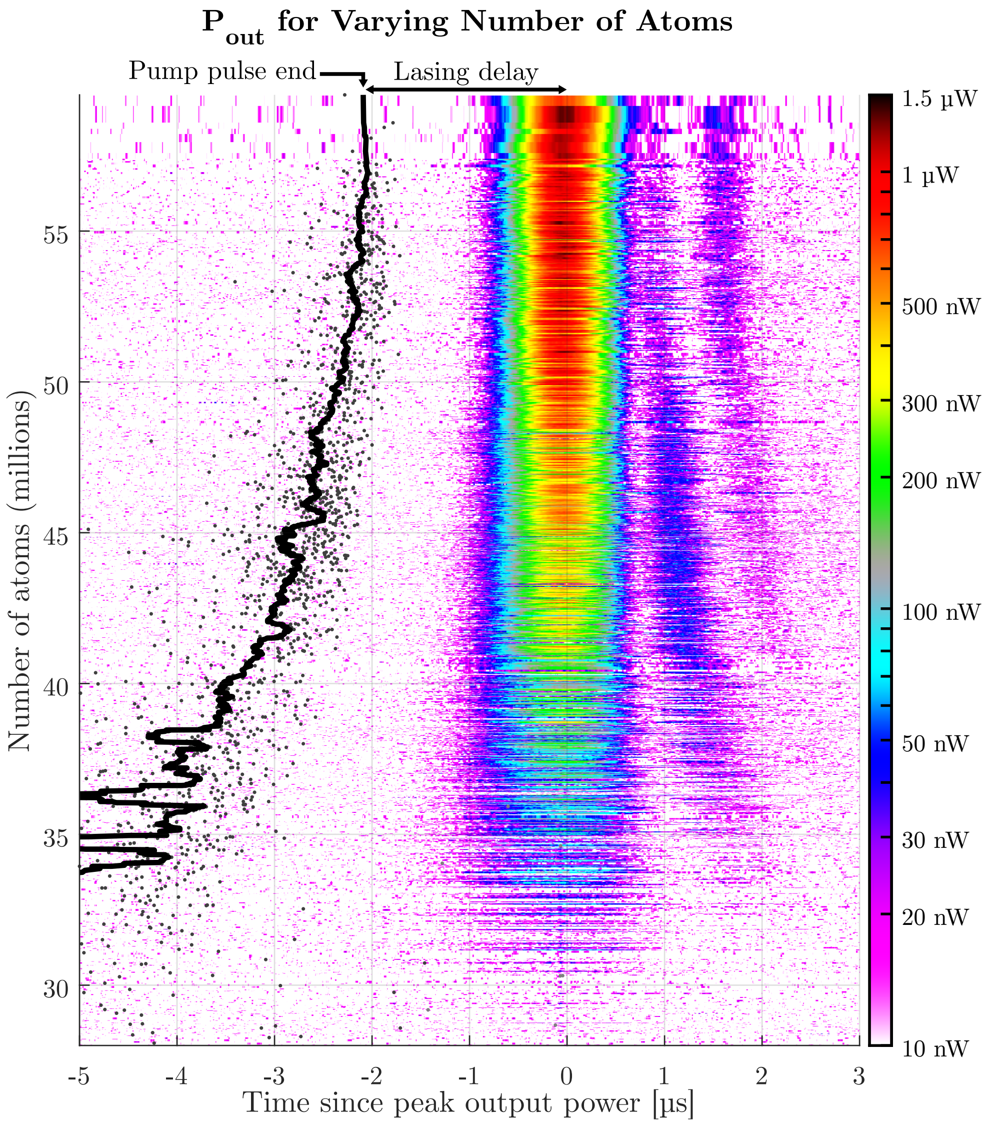

Figure 5.10: *Experimental data showing how the cavity output power during the lasing process depends on the number of ensemble atoms. Black dots: End of pump pulse, line: running mean. For a higher number of atoms, the peak output power increases, the lasing delay shortens, and we see intervals of N (40-50 million) where secondary lasing pulses are more prominent.*

Comparing the results in Fig. 5.10 qualitatively to Fig. 3.36 we see there are similar features. The lasing delay decreases as the number of atoms increases, and the peak output power increases for an increasing number of atoms. We also see an interval where secondary lasing pulses are more prominent (for N between 40-50 million). This could be an interval where the intra-waist Rabi oscillations during the primary lasing pulse end in such a way that many of the atoms closest to the cavity axis end in the excited state before the secondary pulse. We also see that the duration of the lasing pulse itself does not change significantly with the number of atoms, so based on the theory of Section 3.3.7 we may expect to find a regime for high N where the peak cavity output power depends linearly on N.

Thus to compare the results to the model more quantitatively, we look at how the primary pulse peak power and lasing delay scales with the number of atoms. To suppress the effect of noise in this data analysis, a running average function is applied to the fluorescence and cavity transmission data with a span of 20 data points. A number of data sets are then discarded from further analysis to avoid biased results due to noise: The standard deviation σ_I of the first 1,100 data points in the cavity transmission data is calculated for each data set, and if the peak cavity transmission in the set lies within $6\sigma_I$ of the early average, the entire data set is excluded. The full data sample contains 7.68 million data points, so with the $6\sigma_I$ condition, on the order of one point may make it past this filter due to noise fluctuations without being identified. In most cases this would be compared to much bigger signals due to actual lasing pulses, or would fall outside the region where a lasing pulse is plausible, so the risk of falsely identifying peaks due to noise is now very low. For the lasing pulses that are near the noise limit, many samples are discarded due to noise, and the results including only the rest could be biased towards higher intensity pulses than what is representative for a given number of atoms. Therefore if 5 out of 50 data sets in an experimental data group are discarded due to the $6\sigma_I$ condition, the entire group is discarded to avoid systematic bias.

The lasing delay is calculated by first defining the end time of the pump pulse. This is determined by using data from an avalanche photodetector (APD) detecting the power transmitted through the vacuum chamber from the pump pulse. In this data we find the point closest to half the peak value after the detected signal peak occurs. The lasing delay for a data set is then defined as the time between the pump pulse end and the peak in cavity transmission. The value of the cavity output peak power is then determined as the maximum value with the off-resonant background subtracted, defined as the mean value of the first 1,100 data points (when the MOT lasers are on).

The fluorescence signal scales linearly with the number of atoms, but varies a lot between individual cycles for a given Zeeman slower intensity. Therefore we bin the data samples by the average fluorescence signal values when the MOT lasers are on: Each bin contains the 15 most similar average fluorescence values. In the following sections we present the results obtained from this data analysis for the lasing pulse peak power and the delay, and finally compare the results to simulations.

5.3.2 Lasing Pulse Peak Power and the Number of Atoms

The results for the peak cavity output power as function of the number of atoms are shown in Fig. 5.11, note that we estimated a fractional uncertainty of about 12 % on the calibration of the number of atoms. Since we predicted a linear relation in the high-N regime in Section 3.3.7, we fit a linear function to the half of the sample with the highest number of atoms.

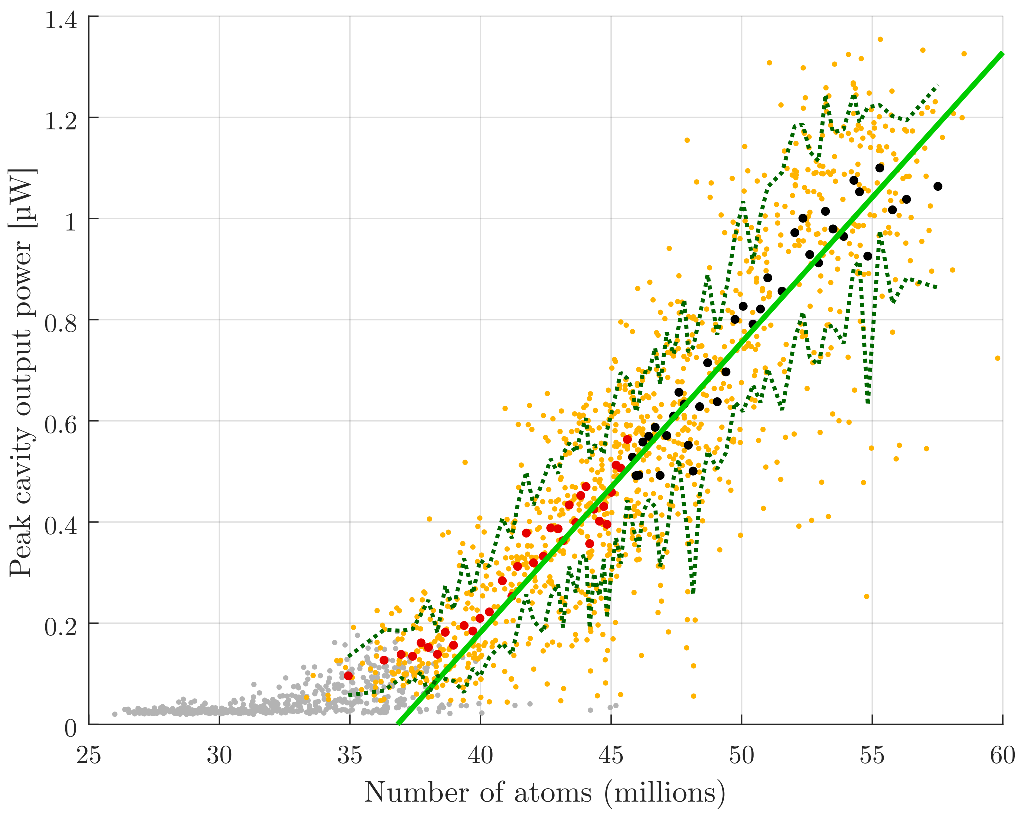

Figure 5.11: *Experimental data for how the peak cavity output power depends on the number of atoms. Gray: discarded based on noise criteria, orange: kept data, red/black: binned data (span: 15 samples), green line: linear fit to the black binned data, dotted lines: standard deviation of the kept data within each bin. For a high number of atoms the peak output power scales linearly with N.*

We see that the linear fit is in good agreement with the data for high N, but is outside the standard deviation for N $<$ (38±5) $\cdot 10^6$. The theory from Section 3.3.7 tells us that this deviation happens because for N near this value, the fraction of the atoms contributing to the lasing pulse depends strongly on N because of the spatially- and velocity-dependent couplings. For N $<$ (35±4) $\cdot 10^6$ the observed pulses become comparable to the noise level.

5.3.3 Lasing Pulse Delay and the Number of Atoms

The results for the dependence of the primary lasing pulse delay on the number of atoms are shown in Fig. 5.12. We fit a reciprocal function to the binned data as this relation was predicted from the simulations of Section 3.3.7. While the data is in agreement with the fit, the narrow region of N we had access to in the experiment does not reveal the curvature very well.

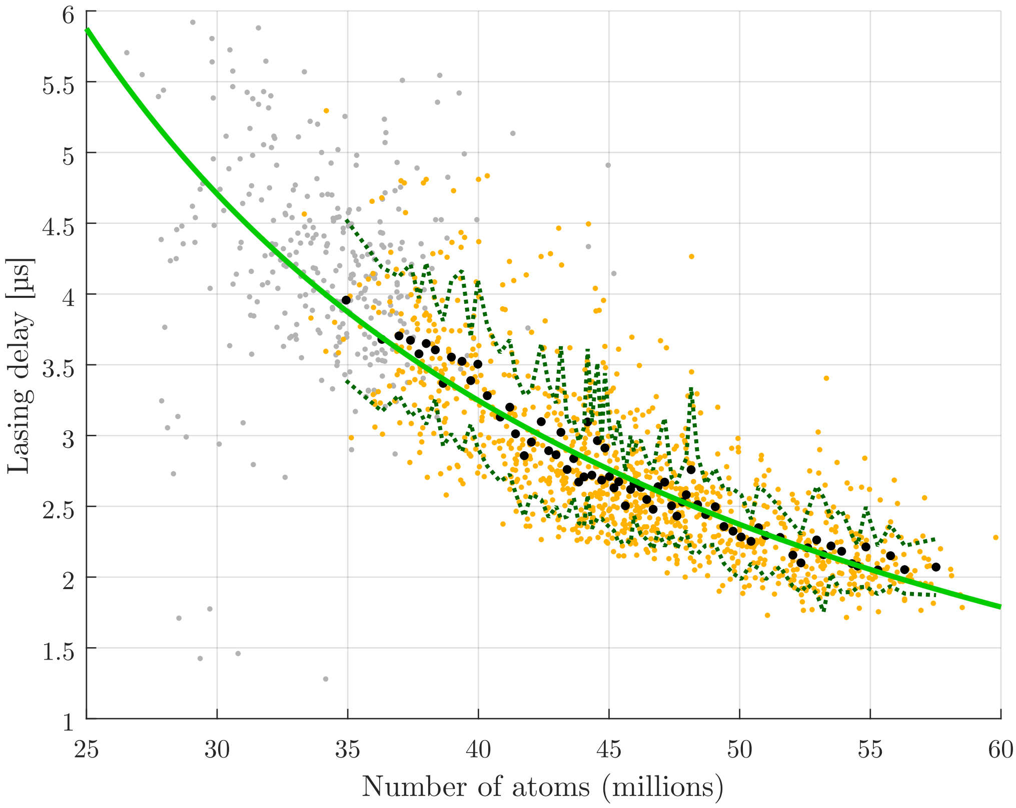

Figure 5.12: *Experimental results for how the lasing delay depends on the number of atoms. Gray: discarded based on noise criteria, orange: kept data, black: binned data (span: 15 samples), green line: reciprocal fit to binned data. Dotted lines: standard deviation of the kept data within each bin. The data is in agreement with the lasing delay scaling as 1/N.*

5.3.4 Scaling with N - Comparison of Simulations and Experiment

In Fig. 5.13 we compare simulations to the experimental data of Fig. 5.11 and 5.12. The parameters used in the simulations are: $P_p = 125$ mW (from on powermeter measurements), $y_{MOT} = 1.5$ mm and R = 0.8 mm (based on the Rabi oscillation simulations of E3), $W_{p1} = 1.36$ mm, $W_{p2} = 2.13$ mm, $\theta_p = 39.2\,°$ (from beam profiler measurements). We show simulations for a range of temperatures from 2 to 4.5 mK.

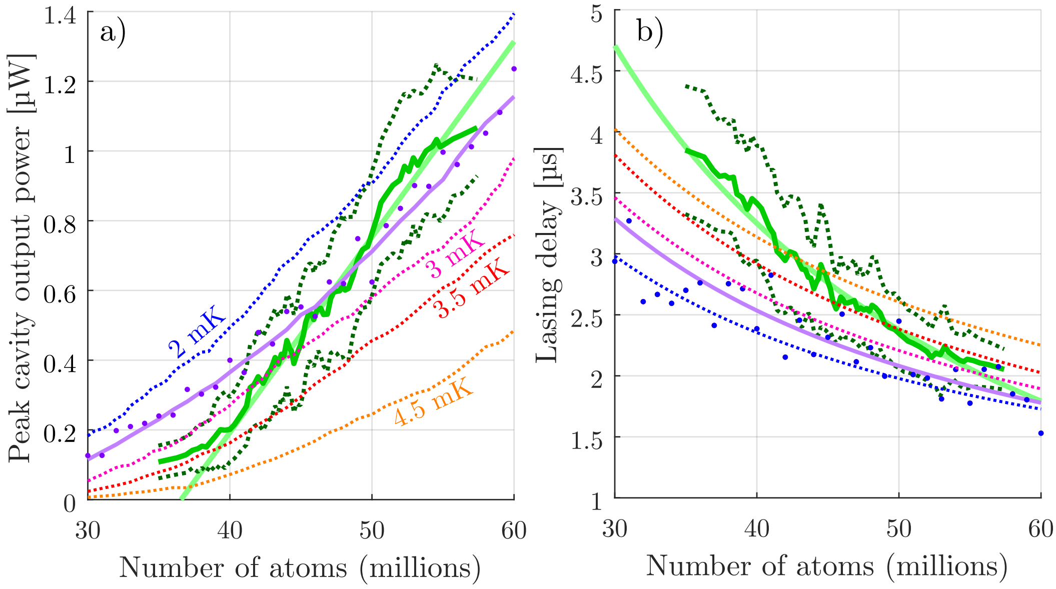

Figure 5.13: *The peak cavity output power (a) and lasing delay (b). We compare the experimental results (green, see details in Fig. 5.11-5.12) to simulations. Lines for simulations show a running mean (a) or reciprocal fit (b) for blue: T = 2 mK, purple: 2.5 mK, pink: 3 mK, red: 3.5 mK, orange: 4.5 mK. Points: Single simulations (shown only for T = 2.5 mK). In the experiments the peak output power and delays appear to scale more strongly with the number of atoms than in simulations.*

We see that in the experiments the peak cavity output power and the lasing delay scales more strongly with the number of atoms than the simulations shown. In addition, if we consider the T = 3 mK example, the simulated peak power is generally lower than found in the experiment, while the lasing delay is generally shorter. Since a higher peak output power is correlated with a shorter delay, this means if we e.g. increase the temperature to 3.5 mK, the lasing delays will be in better agreement with the experimental observations, but the peak output power will be in worse agreement, and vice versa if decreasing the temperature. This behavior may be expected as we found in Section 3.3.1 that the atomic group approximation may bias the output power to be up to 35 % too high, and the delay to be 20 % too short, however we have not investigated how this bias can scale for a varying number of atoms or other parameters. But it may suggest that we should look for simulations where the peak output power overshoots and the lasing delay undershoots the actual results, such as for T = 2 mK. So assuming the estimate of y_{MOT} is correct, this experiment suggests the temperature may be as low as 1-2 mK, while if y_{MOT} is estimated too low, the simulations would require higher temperatures to obtain similar results. There are also significant uncertainties in the calibration of the axis from MOT fluorescence to the number of atoms (estimated near 12 %), which could also help explain discrepancies in the slopes if the number of atoms is higher than what we estimated.

5.3.5 Lasing Driven by a Seed Laser

In Section 3.3.9 we predicted how the lasing process would be affected depending on the seed laser power, and we tested this experimentally in E4. The input field from the seed laser consists of three frequency components - a carrier and two sidebands shifted by 1 FSR with respect to the carrier. In this experiment one of the sidebands is on resonance with the atoms, and the power of this component constitutes the value P_{seed} we are interested in. We vary P_{seed} using an EOM, adjusting the relative amount of power in the carrier and the sidebands. To determine the relation between the experimental parameter we vary, given in dBm, and the variable P_{seed} we are interested in, we use calibration measurements taken by Stefan Alaric Schäffer from our group. To obtain an accurate calibration we choose a function purely on the basis of its high $R^2 = 0.9971$ (Eq. 5.6), including exponential terms to prevent polynomial terms from yielding unphysical, negative values for P_{seed} outside the range of the calibration measurements. These were limited by noise below -15 dBm, but the range investigated in the experiment covers -30 dBm to 5.3 dBm. Therefore it should be noted that the extrapolation below -15 dBm is more uncertain.

$$P_{sideband}/P_{out} = a \cdot \exp(b + c \cdot x) \cdot \left[1 + d(x-e) + f(x-g)^3 \cdot \exp(k \cdot x)\right] \tag{5.6}$$

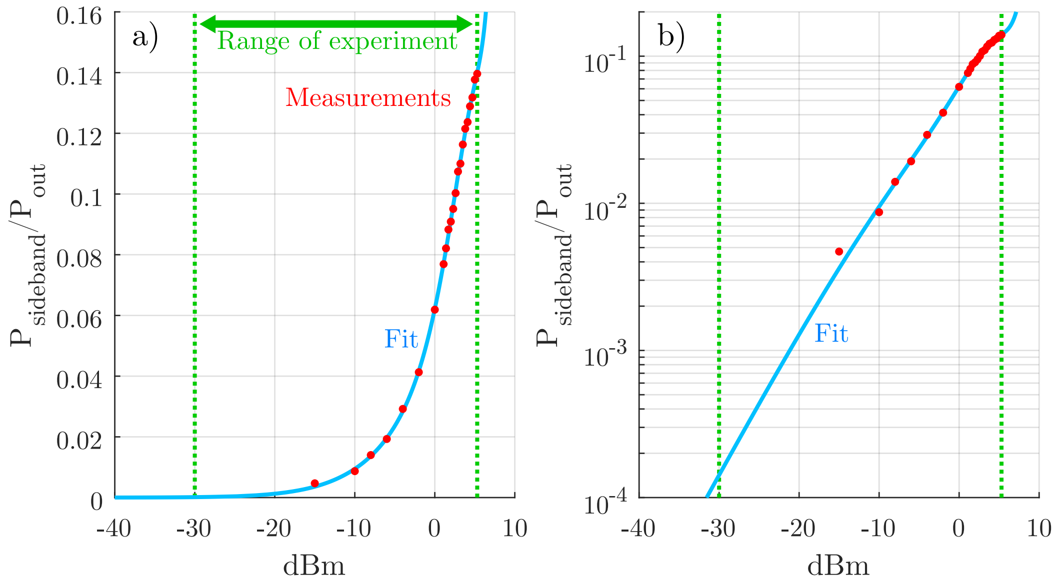

Figure 5.14: *Calibration measurements and fit to determine the seed laser power, a: linear scale, b: logarithmic scale. The estimated uncertainties are* ± 0.0002 *on* $P_{sideband}/P_{out}$*. The extrapolation below -15 dBm is associated with high uncertainty.*

During each operation cycle the MOT lasers are turned off 20 μs before the pump pulse is turned on. The observed cavity output power following the pump pulse is shown in Fig. 5.15, where a running mean with a span of 20 points (300 ns) has been applied to the signals to reduce noise, and the background due to the seed laser has been subtracted, as this also contains the components detuned by 1 FSR. We took 20 data samples for 21 different seed laser power levels, for clarity these are shifted slightly on the P_{seed} axis on the figure so that all of the data is visible. Note that the output power shown here is from only one side of the cavity.

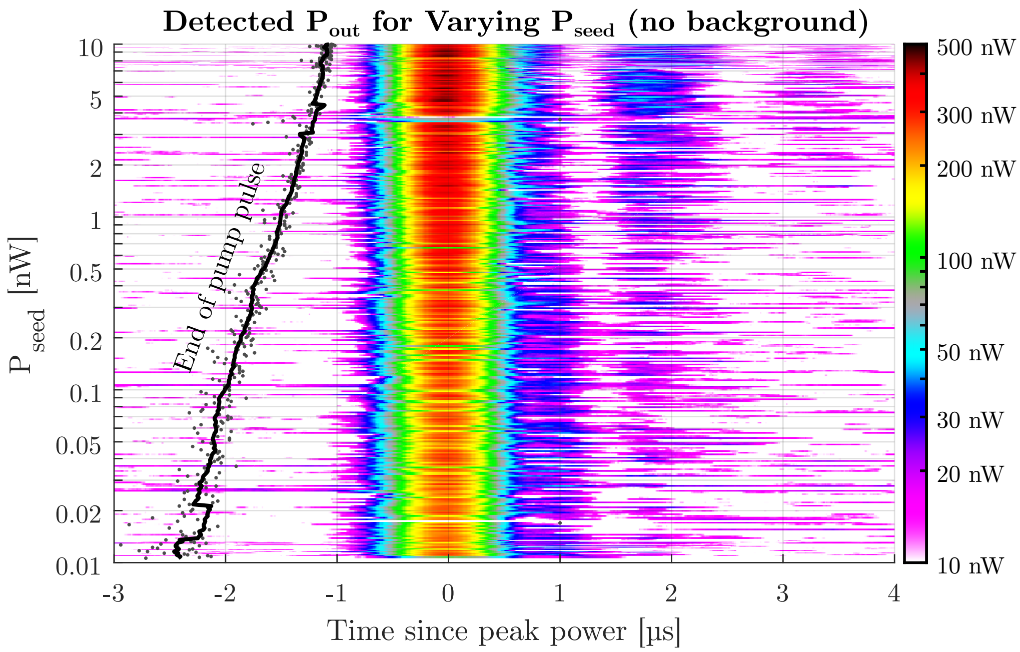

Figure 5.15: *Measured cavity output power for varying seed laser power, represented by dBm, with background subtracted. The peaks of the cavity output power are shifted to t = 0 and the black dots show the end of the pump pulse. We see that as P_{seed} increases, the lasing pulse delay decreases and the peak output power increases.*

We find the mean peak output power and peak delay with respect to the end of the pump pulse for each of the 21 seed laser power levels. These are shown in Fig. 5.16. One of the mean values has been identified as outlier - we see missing cavity output power signal for $P_{seed} \approx 3$ nW in Fig. 5.15.

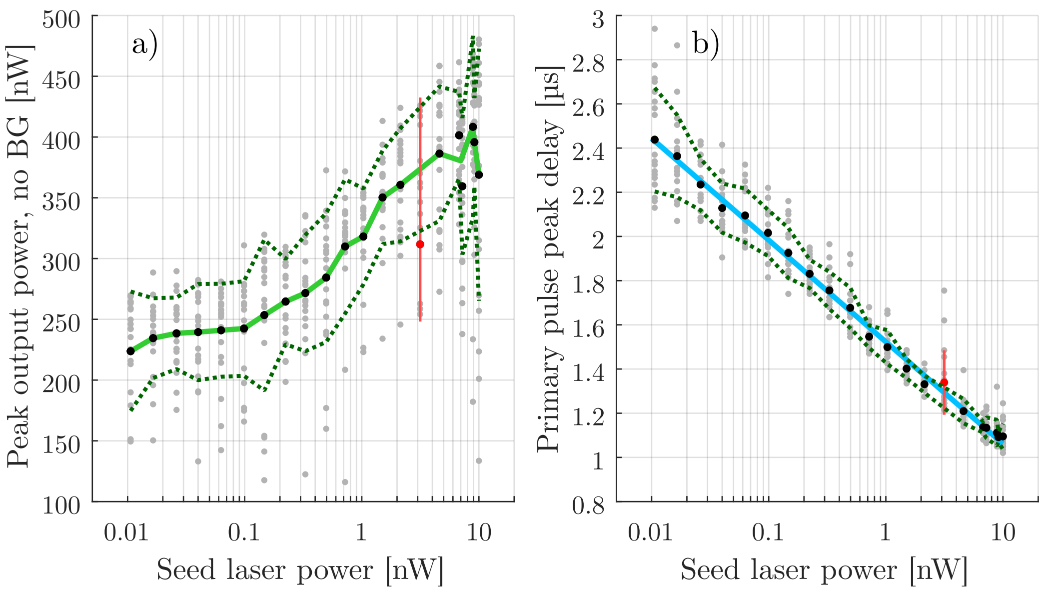

Figure 5.16: *Detected peak output power from one mirror with background subtracted (a) and peak delay with respect to the pump pulse (b), depending on the seed laser power. Gray: single cycle data. Black: mean of single scans, red: outlier (see Fig. 5.15). Dotted lines: standard deviation of each sample. A higher seed laser power leads to a shorter delay (blue fit: delay scales with* $\log(P_{seed})$*) and increased peak output power.*

The rest of the values show a clear trend that as the seed laser power is increased, the peak output power increases and the delay decreases, and for the highest power levels, we also see a kink towards lower peak output power. This only includes two data points, and the variances are large within each sample, so it could be random. However it could also be the feature predicted in Section 3.3.9 due to the intra-waist excited population being reduced after a pump pulse for high seed laser power. Within the experimental range we find that the peak output power delay scales as $\tau_{peak} = -0.46\ \mu\text{s}\cdot \log(P_{seed}) - 2.6\ \mu\text{s}$, shown as the blue fit.

To estimate the number of atoms in the ensemble during this experiment we again use the calibration relation found in Section 5.1.1 of 67 ± 8 million atoms per 100 mV fluorescence signal. In Fig. 5.17 we show how the MOT fluorescence signal varied throughout the experiment, with the corresponding number of atoms on the right axis. Here the gray points show the mean of the 500 initial data points (before the MOT lasers are turned off) from single experimental cycles, and the black points with error bars show the mean of these single cycles and the standard deviation. In this experiment we took all the measurements in order from high to low P_{seed}, which makes it more prone to systematic bias. As shown by the linear fit, the number of atoms is systematically about 5% lower for the lowest values of P_{seed} than for the highest values, which biases the results towards lower peak output power and longer peak delays for lower P_{seed}, amplifying the trends in Fig. 5.16. The average number of atoms during the experiment was 60 ± 7 million for all the cycles. For each sample with the same P_{seed} the standard deviation within the sample was 3.3 ± 0.4 million on average - the number of atoms varies about 6 % from cycle to cycle.

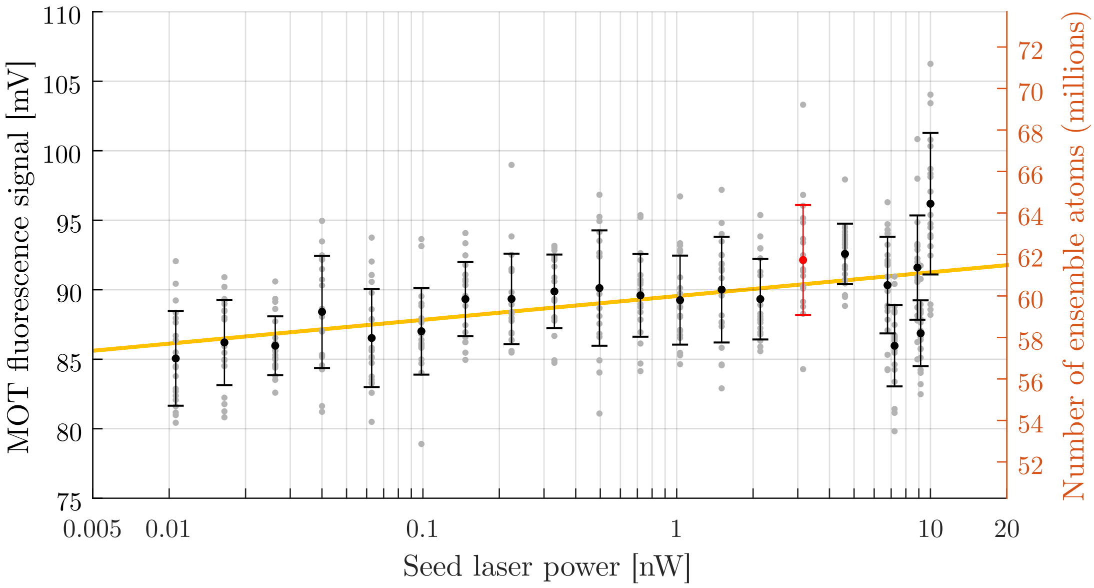

Figure 5.17: *Variation in MOT fluorescence (number of atoms: right axis) throughout the experiment for varying P_{seed}. Gray points: Single cycles, black: mean of 20 cycles for each P_{seed}, red: outlier. Line: fit shows a systematic bias in the number of atoms on the same order as the variation between individual cycles (error bars).*

Simulation results are shown in Fig. 5.18 (peak output power) and 5.18 (peak power delay) for the most plausible parameters investigated. The pump pulse parameters used here are $P_p = 125$ mW, $W_{p1} = 1.36$ mm, $W_{p2} = 2.13$ mm and $\theta_p = 39.2°$, which were all determined experimentally. The density parameter R = 0.8 mm was used since it was in good agreement with the Rabi oscillation results, and is still plausible considering the uncertainties of Section 5.1.4. T = 4.5 mK and y_{MOT} = 1.5 mm were used, since the Rabi oscillation results showed good agreement for these parameters. We show simulations for N = 57, 60 and 63 million atoms.

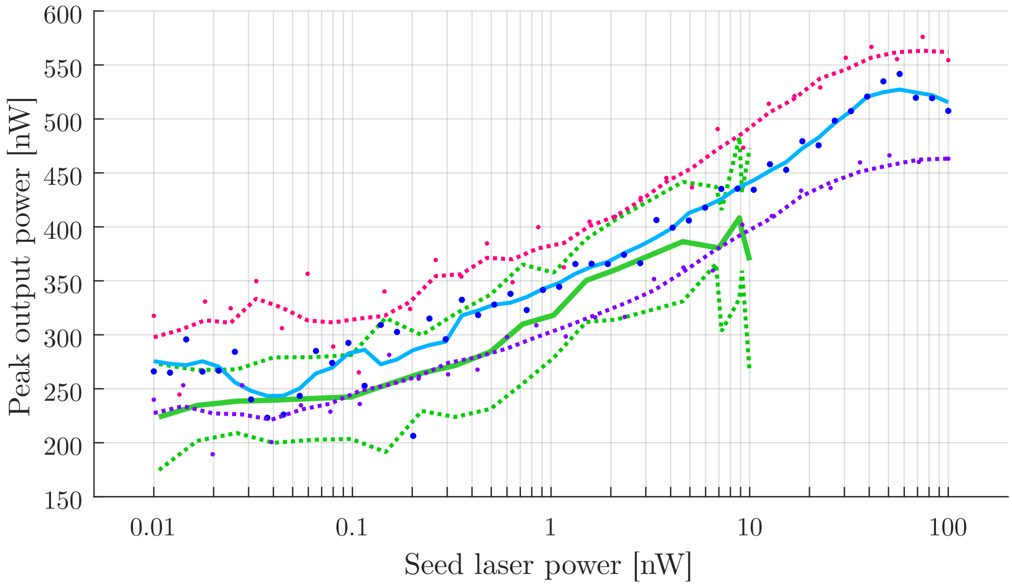

Figure 5.18: *The results (green) of Fig. 5.16a compared to simulations. Points: single simulations, lines: moving mean. Red: $N = 63 \cdot 10^6$, blue: $N = 60 \cdot 10^6$, purple: $N = 57 \cdot 10^6$. The differences between simulations and experimental data are well within the confidence bounds due to variations in the number of atoms.*

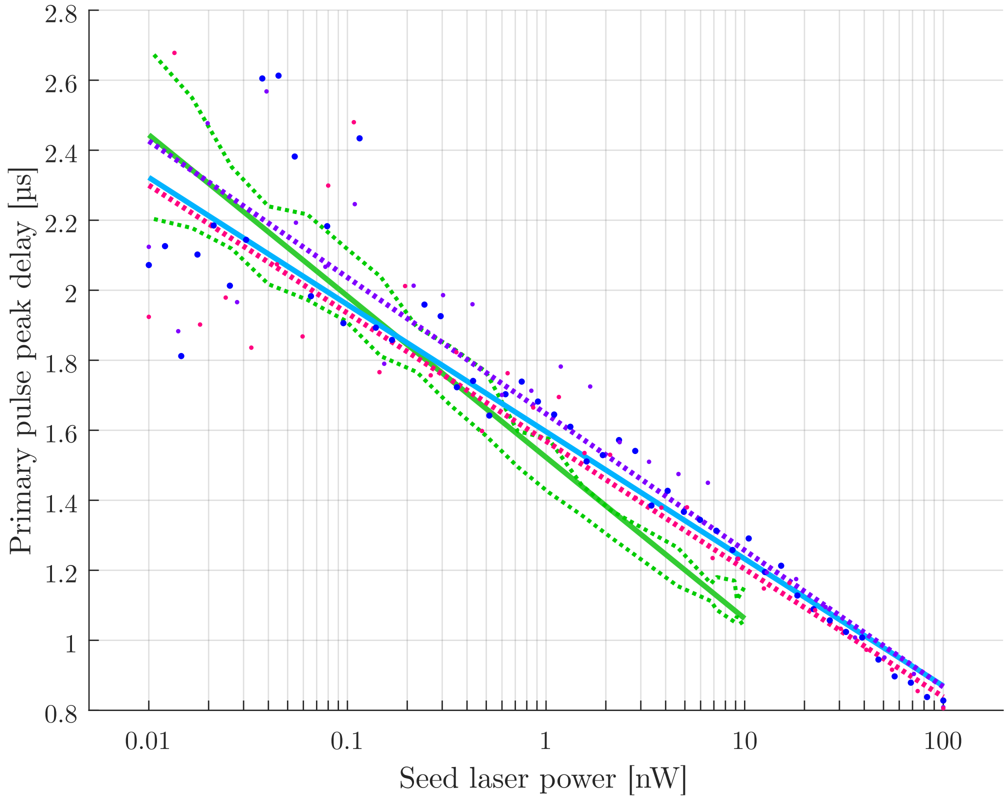

Figure 5.19: *The results (green) of Fig. 5.16b compared to simulations. Points: single simulations, lines: linear fits weighed by a moving standard deviation. Red: $N = 63 \cdot 10^6$, blue: $N = 60 \cdot 10^6$, purple: $N = 57 \cdot 10^6$. The slopes deviate from the experimental observations, and variations in the number of atoms seem to be an insufficient explanation.*

The simulations suggest that the kink observed in the peak output power near $P_{seed} = 10$ nW would be random - in the simulations it occurs at $P_{seed} = 50$ nW due to the population dynamics. The peak output power on Fig. 5.18 is in good agreement with the experimental results - fluctuations in the number of atoms on the order of 5 % can easily explain discrepancies, as illustrated by the two simulations for 57 and 63 million atoms, of which the value of 57 million appears to be in best agreement with the experiment. However we must remember the bias from the atomic group approximation found in Section 3.3.1, which we have not investigated the effect of in this regime, but if the bias towards higher peak output power is significant, we may have a higher number of atoms, lower temperature and/or higher y_{MOT} in the experiment than in these simulations.

The fits to the simulation results of the lasing delay yield $\tau_{peak} = -(0.36 \pm 0.02)\ \mu\text{s}\cdot \log(P_{seed}) - (1.7 \pm 0.2)\ \mu\text{s}$, and the systematic variation in the number of atoms is insufficient to explain the deviation from the experimental results. One effect which could affect the slope would be if the bias of the atomic group approximation varies with P_{seed}. If this is not the case, it suggests that the parameters of the simulation are not accurate. Simulations run when exploring the parameter space related to this experiment indeed show that a steeper slope in good agreement with the experiment is obtainable for temperatures of 3 mK and for both $y_{MOT} = 1.5$ mm and 4 mm (these simulations are shown in Appendix A.2). This temperature would also be more consistent with the findings in the experiment with varying number of atoms (Section 5.3.4), which was performed on the same day.

5.3.6 Lasing in a Detuned Cavity

In Section 3.3.3 we saw that the model predicts oscillatory behavior for the cavity output power when the cavity is detuned. We have tested this prediction in experiment E5. Here the Noise Immune Cavity Enhanced Optical Heterodyne Molecular Spectroscopy (NICE-OHMS) technique [31] becomes relevant. The basic idea behind the technique is that we generate sidebands offset by 1 FSR (781 MHz), and by detecting the relative phase between these sidebands (which do not interact with the atoms) and the resonant light which interacts with the atoms, we can generate an error signal used as feedback for the cavity mirror piezo. Thus we can lock the cavity to the atomic resonance, or detuned from it by setting an offset.

We vary the detuning over a range of about 2.8 MHz around the atomic resonance in steps of 0.1 MHz. For each detuning we save 100 single scans on the oscilloscope. These scans are shown on Fig. 5.20 in the heatmap format of Section 3.3, note however the different color scale and that it represents the output from one mirror only. The detuning increments are 0.1 MHz - samples with identical detuning are spread out over segments of 0.1 MHz, rather than varying continuously. The background light detuned by 1 FSR has been subtracted from the data.

Comparing this qualitatively to the simulations in Fig. 3.27 the overall structure is similar, but there are also some differences. On resonance, the duration of the lasing pulse is shorter than for higher detunings, unlike in the simulations. In addition we find that oscillations are very strongly suppressed when the cavity is on resonance.

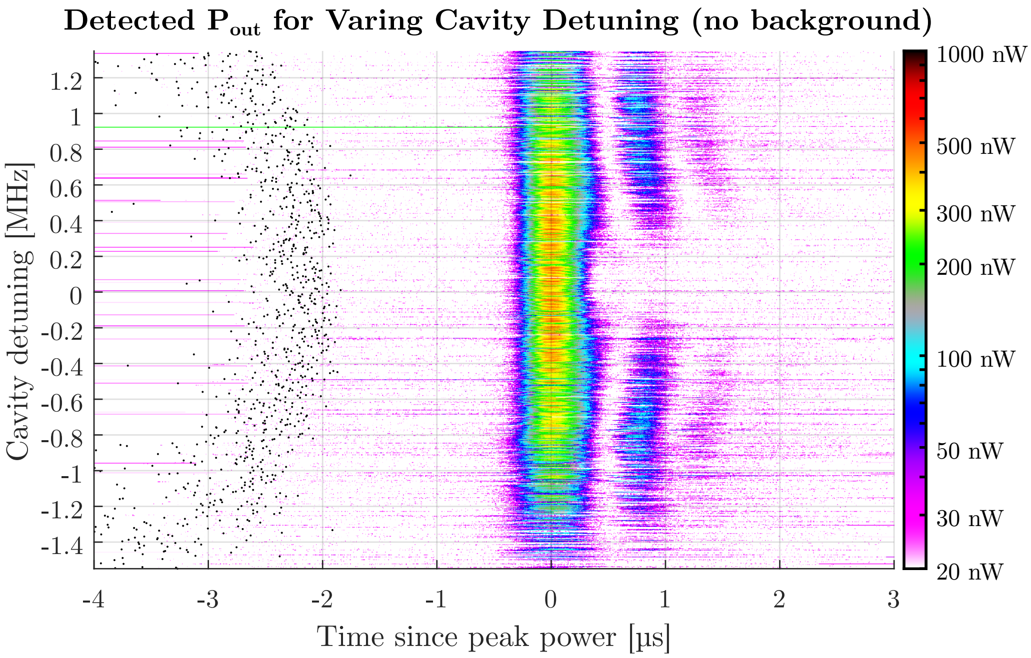

Figure 5.20: *Experimental cavity output power for varying cavity detuning, with far-detuned background light subtracted. Black dots mark the end of the pump pulse. We recognize that oscillatory dynamics are more prominent for a detuned cavity, and see they are highly suppressed when the cavity is on resonance.*

Two examples of the single scans are shown in Fig. 5.21: For a resonant cavity ($\Delta = 0$), and for a detuned cavity with $\Delta = 0.9$ MHz, where the secondary pulse peak power is highest.

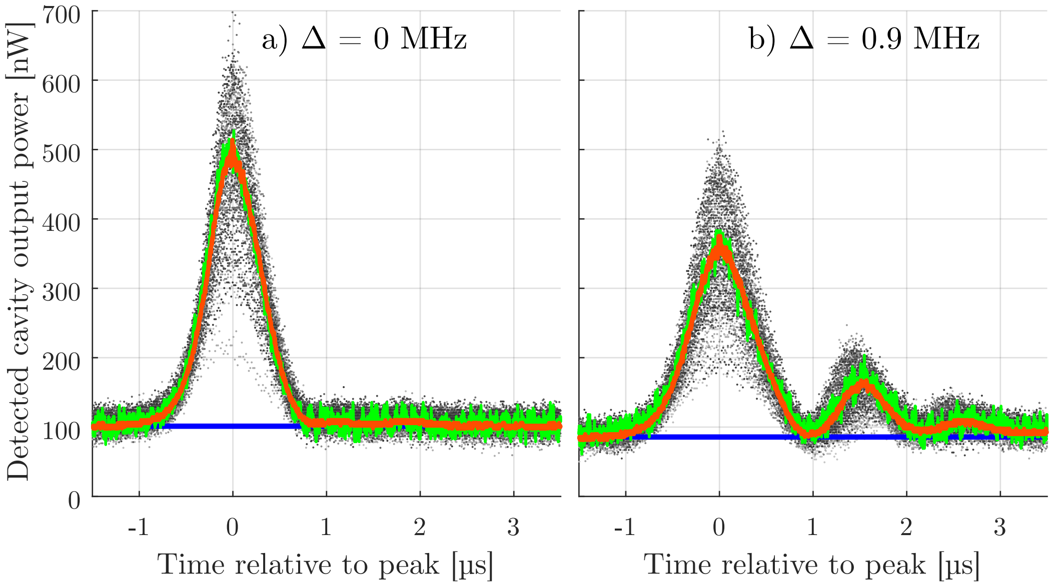

Figure 5.21: *Cavity output power for a lasing process with a resonant (a) and detuned (b) cavity. Gray: data from 98 (a)/88 (b) single experimental cycles offset in time for synchronized cavity output peak time. Blue: background due to off-resonant light for locking the cavity. Orange: median of the single cycle data. Green: the single scan within the sample most similar to the median. We see for a detuned cavity the primary pulse peak is lower and oscillations are prominent.*

In this and the further data analysis we discard scans with primary peak power below 180 nW as outliers as these are close to the noise level of the background. Based on the remaining single scans we find the most representative sample, whose data points have the minimum sum of absolute deviations from the median data points. We then find the primary and secondary peak power of the representative samples for each detuning, subtract the background signal used for locking the cavity, and multiply the resulting power by two to compensate for the leak through the mirror with no detector. The resulting cavity detuning-dependence of the primary and secondary peak output power is shown in Fig. 5.22.

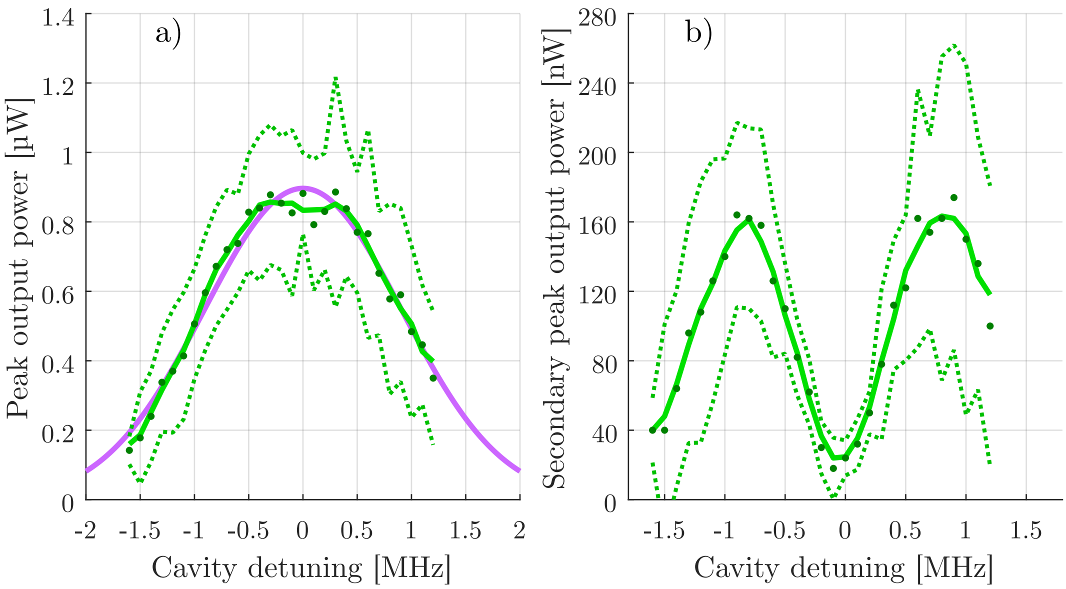

Figure 5.22: *Experimental results for how the primary (a) and secondary (b) peak cavity output power depends on the cavity detuning. Points: median peak of samples above noise criteria, dotted line: ± standard deviation, line: running mean. Purple: Gaussian fit with a width corresponding to $T = 4.2$ mK.*

We also show a fitted Gaussian function to the primary peaks. This corresponds to a one-dimensional Maxwell-Boltzmann distribution for a temperature of 4.2 mK. Recalling the simulation of Fig. 3.29, fitting a Gaussian yielded a temperature that was 43 % larger than the actual temperature, and we have no better indication of its accuracy in an experiment. Based on this we estimate the temperature at 3^{+3}_{-1} mK.

In Fig. 5.23 we show the MOT fluorescence and the corresponding estimated number of atoms for the different cycles throughout the experiment. The mean number of atoms is $(90 \pm 10) \cdot 10^6$, higher than in previous experiments, with a mean standard deviation of $(2.7 \pm 0.3) \cdot 10^6$ atoms from cycle to cycle. From the linear fit we see the systematic bias was on the order of $2 \cdot 10^6$, which is low compared to the total number of atoms and on the order of the random fluctuations from cycle to cycle, so this probably does not bias the results significantly.

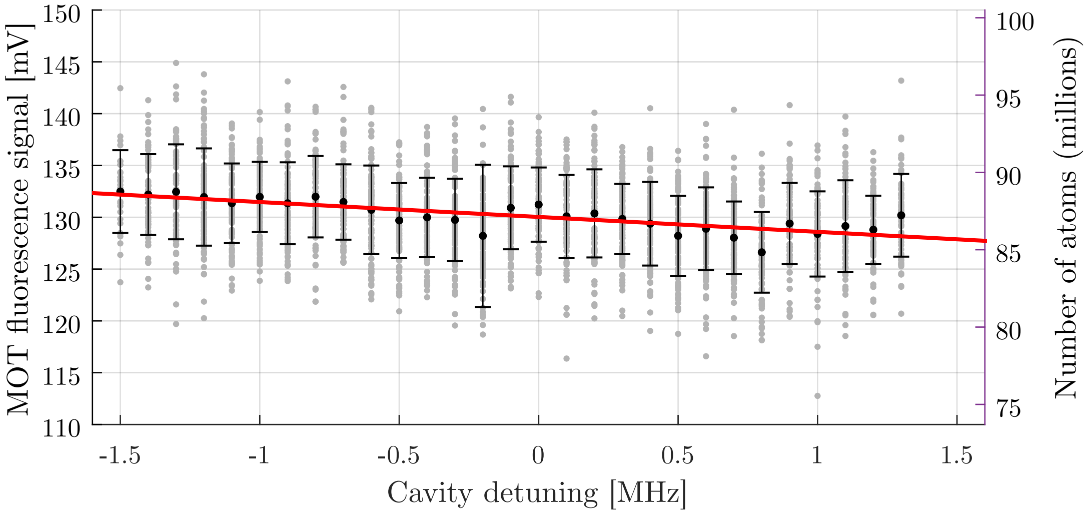

Figure 5.23: *Variation in MOT fluorescence (and number of atoms - right axis) throughout the experiment for varying cavity detuning. Gray points: Single cycle data, black: mean of non-discarded cycles. Line: linear fit shows there is little systematic bias in the number of atoms throughout the experiment.*

This experiment was carried out some weeks after the previous experiments we have studied, and since we have optimized the MOT alignment beams to obtain more atoms, this also means that parameters such as ensemble temperature, density and y_{MOT} may have varied since E1-E4. We have investigated several combinations of parameters but not found any combination that quantitatively replicates the experimental findings. Simulation examples for two combinations of parameters are shown in Fig. 5.24. In the first example (orange) we show results with the parameters of Section 3.3, in the second example we show results for the same parameters except that N $= 58 \cdot 10^6$.

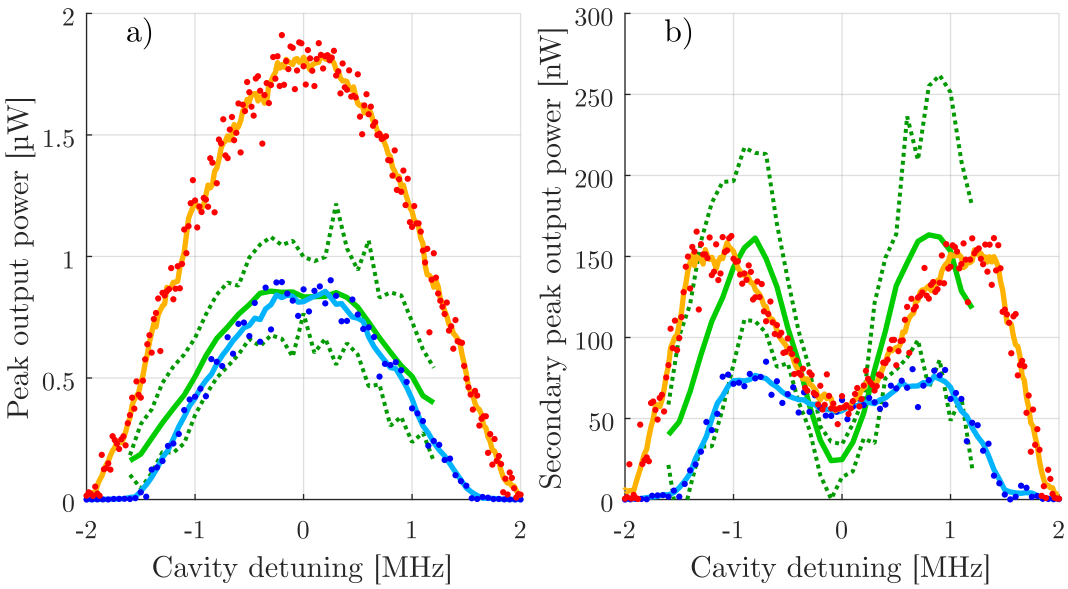

Figure 5.24: *The primary (a) and secondary (b) peak cavity output power due to the lasing process shown as function of cavity detuning. Green: experimental results of Fig. 5.22. Red: Simulations with parameters of Section 3.3. Blue: Simulations with 58 million atoms. The quantitative agreement is poor.*

These parameters yield some of the closest results to the experiment quantitatively, though the agreement is still poor when considering that both the primary and secondary peak features must be consistent. To compare the ability of simulations with different parameter combinations to replicate the main features of the results we choose three parameters to investigate: The peak output power on resonance (Z), the secondary peak output power on resonance (Y), and at the cavity detuning where it is highest (X). We normalize these by the experimental results, so the experiment has coordinates (X,Y,Z) = (1,1,1). This is shown in comparison to simulations for various parameter combinations in Fig. 5.25.

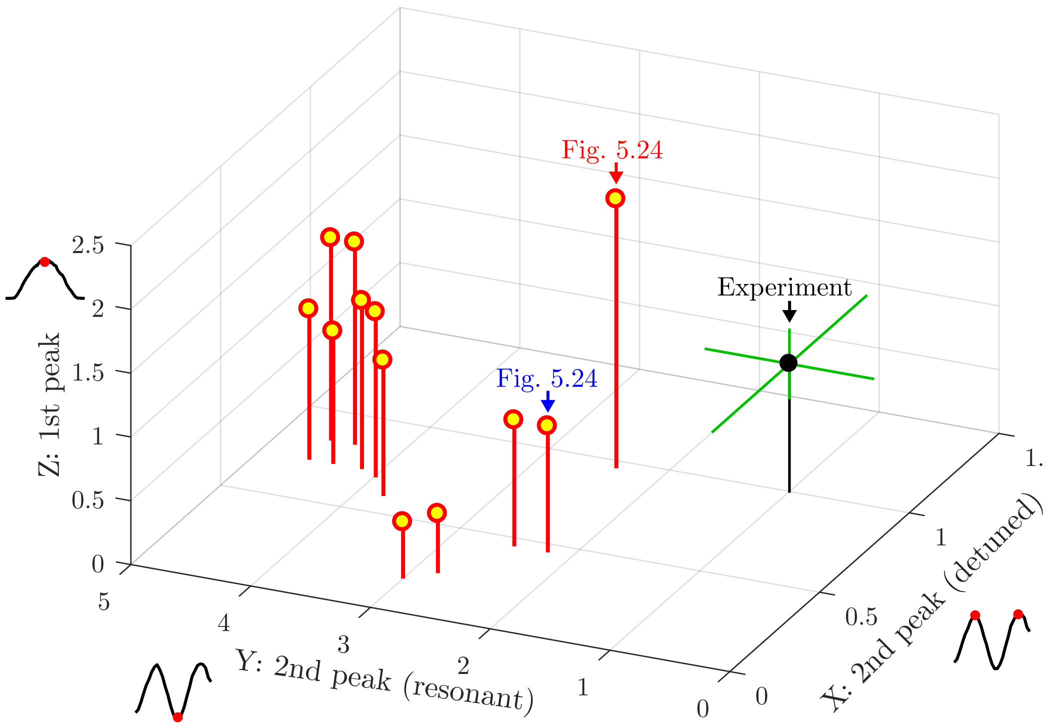

Figure 5.25: *Comparison of simulations with various parameters to experimental results (black, error bars in green) for three characteristic properties of the results. We have not found a combination of parameters yielding good quantitative agreement. In the experiment the secondary pulse peaks depend more strongly on the cavity detuning than in the simulations.*

Here we see that the simulations for 58 million atoms (blue in Fig. 5.24) are closest to quantitative agreement with the experiments when accounting for the error bars, but are still very far from it, and we also note that the beam profile and number of atoms used in these simulations are far from the independently estimated values for the experiment, with the beam profile expected to be approximately the same as in E4. A very notable feature in the experiment is that the secondary peaks in cavity output power are extremely low (< 40 nW) when the cavity is on resonance while featuring large (160 nW) secondary peaks for the detuning where they are maximal. Even though the feature is strongly visible in Fig. 3.29, the primary peak output power is also twice as high, ruling out this combination of parameters. For parameters where the primary output power is in good agreement with the experiment, the secondary peak output power distribution tends to resemble something closer to a top hat. In conclusion, it is unlikely that a combination of experimentally plausible parameters exists that yield good quantitative agreement with these results. This is so far the strongest experimental evidence that significant physical effects could be missing in the model.

5.4 Summary of Experimental Results

In our experimental work we have estimated important parameters for the model - the number of atoms at (67±8) million in experiment E3, the cavity linewidth $\kappa = 2\pi\cdot(620.3\pm0.4)$ kHz and the ensemble density parameter R = (1.0±0.1) mm. Comparing the model to different experiments suggests R may be closer to 0.8 mm, and we have estimated the temperature at 3^{+3}_{-1} mK in experiment E5. We have also optimized and measured the pump beam waist size, and found that $W_{p1} = 1.36$ mm, $W_{p2} = 2.13$ mm and $\theta_p = 39.2°$ yielded highest lasing output power of the ones we investigated, though we have not investigated the predicted optimal beam profile of $W_{py} = 1.0$ mm and $W_{pxz} = 2.4$ mm from Section 3.3.6.

We have also compared several of the model's predicted dynamics to experimental observations. In one experiment the Rabi oscillations agreed well with simulations for experimentally plausible parameters. In the others the simulations required implausibly low pump pulse power to be in agreement, possibly due to frequency instabilities in Slave Diode 2.

Finally we have investigated how the lasing process depends on the number of ensemble atoms, seed laser power and cavity detuning. In all cases we confirm qualitative predictions from the model, though we have also found quantitative discrepancies. Notably the peak cavity output power and lasing delay scale more strongly with the number of atoms than we find in simulations. The observed scaling of the lasing peak output power agrees well quantitatively with simulations, though the lasing delay scales more strongly with the seed laser power than in simulations. Additional simulations suggest these discrepancies can be due to the temperature being closer to 3 rather than 4.5 mK in the experiment, and that part of the deviation also stems from the atomic group approximation.

The experiment with varying cavity detuning revealed a very strong dependence of the cavity power oscillations on the cavity detuning: on resonance the secondary peak output power was merely (20±20) nW, while for $\Delta = 0.9$ MHz it was maximal at (170±90) nW. An extensive number of simulations for a range of parameter combinations did not replicate such a strong dependence, and tend to show that the dependence on detuning is very weak for $|\Delta| < 0.9$ MHz in the regime where the simulated primary output power peak is in agreement with the experiment.

CHAPTER 6

Future Prospects

6.1 Simulation Improvements

The most straightforward improvement to the model would be to calculate a decoherence rate due to atomic collisions, based on the temperature and density. This reduces the number of unknown parameters by one and may help us setting more narrow bounds on the temperatures in the simulations. Also the effect of spontaneous emission into the cavity mode should be accounted for, using e.g. the Heisenberg-Langevin approach.

Secondly, we have not evaluated the accuracy of the semiclassical approximation of factorizing the expectation values. It is crucial for the simulation that the number of differential equations scales linearly with the number of atoms or atomic groups, but more insight in the potential problems with the approximation may help explain the differences between simulations and experiments. If the theory is significantly affected by the approximation, the model could possibly be rewritten using a stochastic wavefunction approach, where the scaling is also more favorable than in the master equation approach [11, p. 821].

The large amount of time required to run simulations and the large number of parameters affecting the system makes it demanding to fit the model to experimental data, for example as seen in Section 5.3.6. When there is only time to run e.g. 10-100 simulations, and there are several parameters affecting the dynamics, it is crucial that the parameters for each simulation are chosen wisely to be able to learn anything about the system, and not randomly by e.g. a χ^2 minimization routine. Machine learning is becoming increasingly common within the physics community, and has a wide range of applications for both modeling, data treatment and experimentally. For example it has been used to optimize the optical density in a MOT using a sequence of laser pulses too advanced and remote from intuition for humans to come up with [32]. To search for parameter spaces within the model that could be in better agreement with experimental data, a neural network could be trained to build up its own mapping of how the different parameters affect the system and make educated guesses for new simulation parameters based on them. While the neural network's mapping can rarely tell us about the underlying physics in such systems, it may be able to search the parameter space more efficiently than humans, which may help us to investigate the discrepancies in Fig. 5.25 further.

6.2 Second-stage Cooling

Our findings in simulations of the dynamics of the current system showed that many different velocity groups play a role in the lasing process. Though we found in the steady state simulations for single atoms that interaction with the cavity mode for low power is extremely sensitive to the cavity detuning, the ensemble simulations did not show clearly that one particular velocity group starts the process. If the interval of velocity groups which can initiate the lasing process is not very narrow (a range in Doppler shifts on the order of Γ), we may not be within the desired bad cavity regime, and our potential frequency stability could be limited by the ensemble temperature. For these reasons we consider the prospects of further cooling the ensemble.

Since the $^1S_0$ - $^3P_1$ transition has a linewidth much more narrow than the $^1S_0$ - $^1P_1$ linewidth, the ensemble could be further cooled on the $^1S_0$ - $^3P_1$ transition with a second-stage 'red MOT'. This yields a Doppler cooling limit of just 0.18 μK, a factor 1000 below the limit of the current MOT. However the range of velocities that could be caught would also be narrow, so the original 'blue' $^1S_0$ - $^1P_1$ MOT would still be necessary as an initial step, and a large fraction of atoms would be lost in the process. With a red MOT, temperatures down to around 40 μK, R $\approx$ 0.25 mm and $3 \cdot 10^7$ atoms have been reported [23, p. 3]. A disadvantage of the red MOT is that the system becomes significantly more complicated, though it would still be simpler than the systems utilizing optical lattices.

We run simulations for ensembles with various numbers of atoms, assuming we are able to obtain R = 0.3 mm and T = 50 μK and otherwise the standard parameters of Section 3.3. The output power is shown in Fig. 6.1, and population dynamics in Fig. 6.2. With these parameters very close to 100 % of the population within the waist can be excited because of the low temperature. We see that if we can capture about five to ten million atoms, we can obtain an output power (and thus signal to noise ratio) comparable to our current experimental setup. Furthermore we see that if the ensemble is highly populated, the intra-cavity field builds up to such a high intensity that it drives several Rabi-oscillations within the cavity population during the primary lasing pulse.

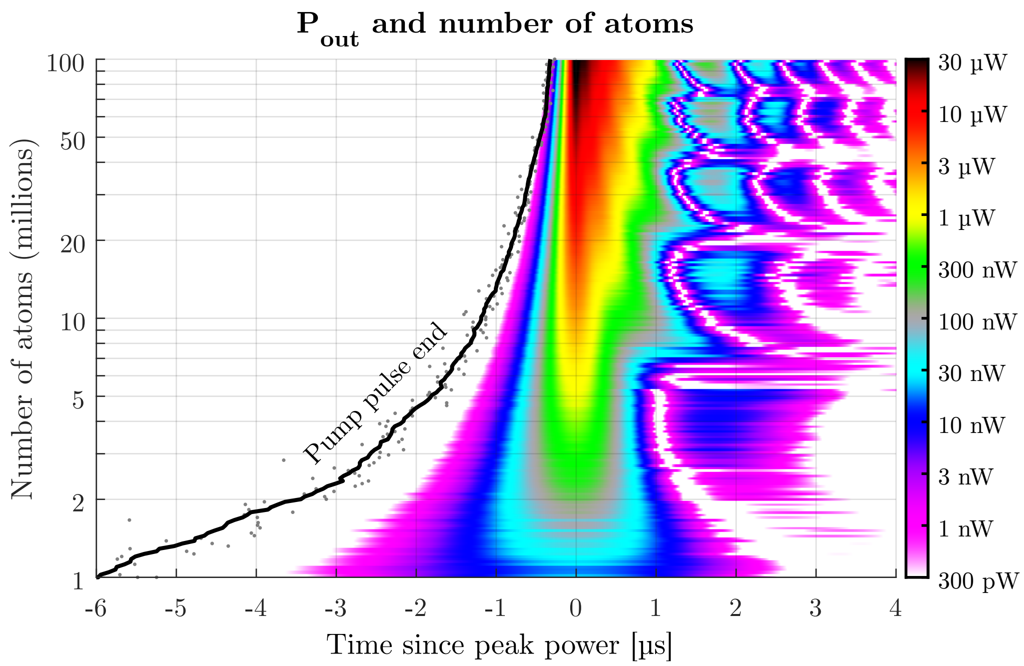

Figure 6.1: *The dependence of the cavity output power on the number of atoms for an ensemble with parameters obtainable with a red MOT. If about 5-10 million atoms are trapped, a good signal to noise ratio comparable to our current setup may be obtained. Several intervals with alternating prominent or small output power oscillations are visible.*

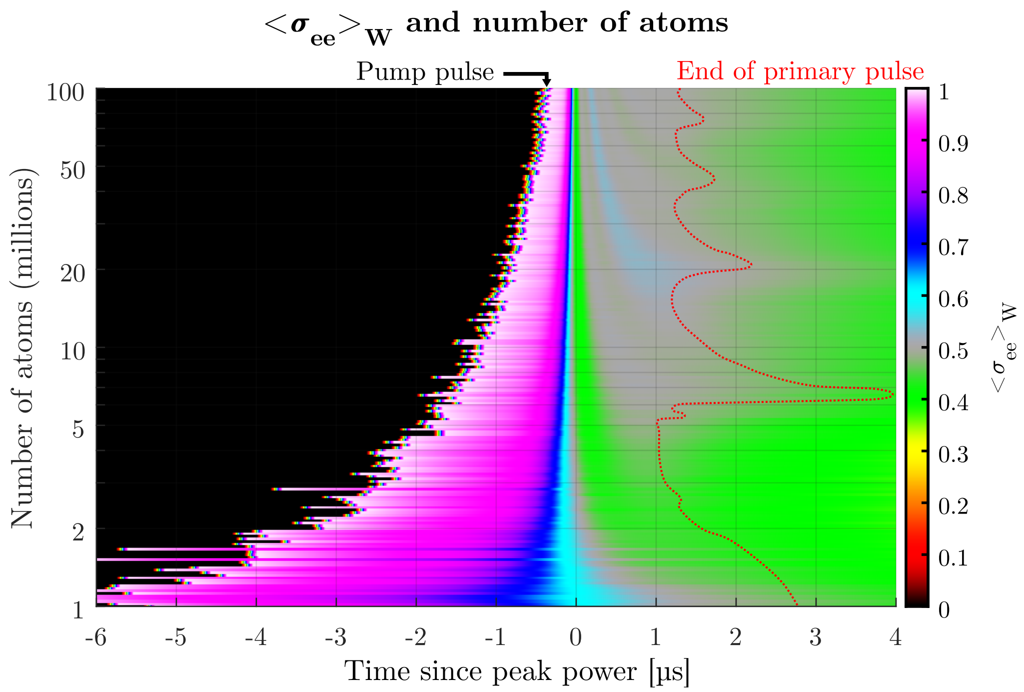

Figure 6.2: *Population dynamics for varying number of atoms in an ensemble with parameters obtainable with a red MOT. Once the intra-cavity power becomes high, it drives Rabi-oscillations in the atomic population - up to 4 cycles for N $\sim$ 100 million.*

CHAPTER 7

Conclusion

We have investigated the dynamics of a laser-driven optical cavity and a moving atom interacting with a cavity mode, finding results for how the interaction depends on the cavity detuning, intra-cavity power and atomic speed. Subsequently we investigated the effects of extending the model to a thermal ensemble interacting with the cavity mode and a pump laser. Using this model we investigated the main influence that different parameters have on the obtainable excited population and lasing dynamics. We also predicted optimal waist sizes of 2.4 mm and 1.0 mm for the pump pulse to maximize the signal to noise ratio of the lasing pulse, given the standard parameters of Section 3.3, and that there could be advantages in aligning the pump pulse close to the cavity axis.

Following this, we investigated how the lasing dynamics depend on the cavity detuning, and by grouping atoms by their velocities and positions we gain additional insight into the process. We see how the population dynamics vary across the ensemble spatially and across different velocity groups, and find highly synchronized absorption and emission across different velocity groups in a detuned cavity, promoting oscillatory dynamics.

Based on the results from investigating the ensemble interaction with the pump pulse, we determined the main experimental options to enhance the lasing process. We documented the changes to the setup in upgrading the pump pulse power using a tapered amplifier, which we found to be the most viable way of improving the setup. This has improved the signal to noise ratio when observing the lasing process and enabled the system to act as a master laser.

We have presented experimental results for determining some of the important variables for the model. We determined the cavity linewidth at (620.3±0.4) kHz, the number of atoms at (67±8) $\cdot 10^6$ in one experiment and the ensemble density parameter R = (1.0±0.1) mm. Finally we investigated the dependence of the lasing dynamics on the number of atoms, seed laser power and cavity detuning, and compared the results to the model. We find several qualitative agreements, while quantitative comparisons are challenging due to bias from the atomic group approximation as well as high uncertainties on several parameters. Especially the observed oscillations in cavity output power appear to be more sensitive to the cavity detuning than predicted by the model.

Finally we investigated the prospects of second-stage MOT cooling. Our model suggests that the frequency stability of the lasing signal could be improved by building a second-stage MOT to lower the temperature, which can also utilize the tapered amplifier, and that this is viable if we can trap 5-10 million atoms in the final ensemble.

Appendices

A.1 Influence of the MOT Coil Axis

In some simulations, an error in the code caused the modulation of the intensity was implemented so it corresponded to the coil symmetry axis to lie along the x rather than y axis. The effect of this can be seen on Fig. A.1 and A.2 (compare to Fig. 3.17 and 3.18). This reduces the negative influence of the magnetic field on the Rabi frequency, however the influence is tiny if y_{MOT} (or here, x_{MOT}) is 4 mm, the standard value for the parameter. Therefore the influence of the code error on the results in the other cases is negligible.

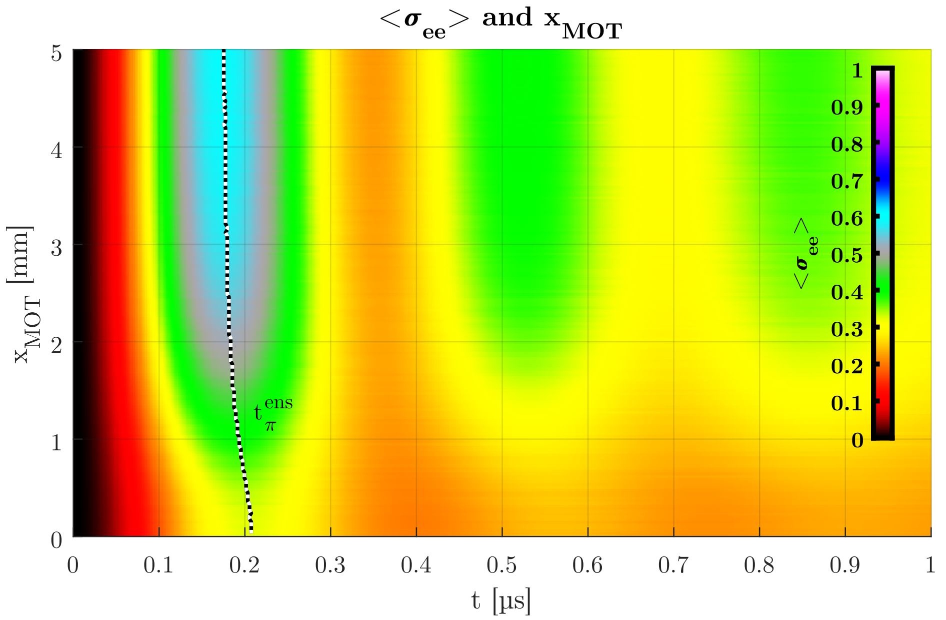

Figure A.1: *Population dynamics during a pump pulse for varying x_{MOT}, the standard parameters of Section 3.2 and 70,000 atomic groups.*

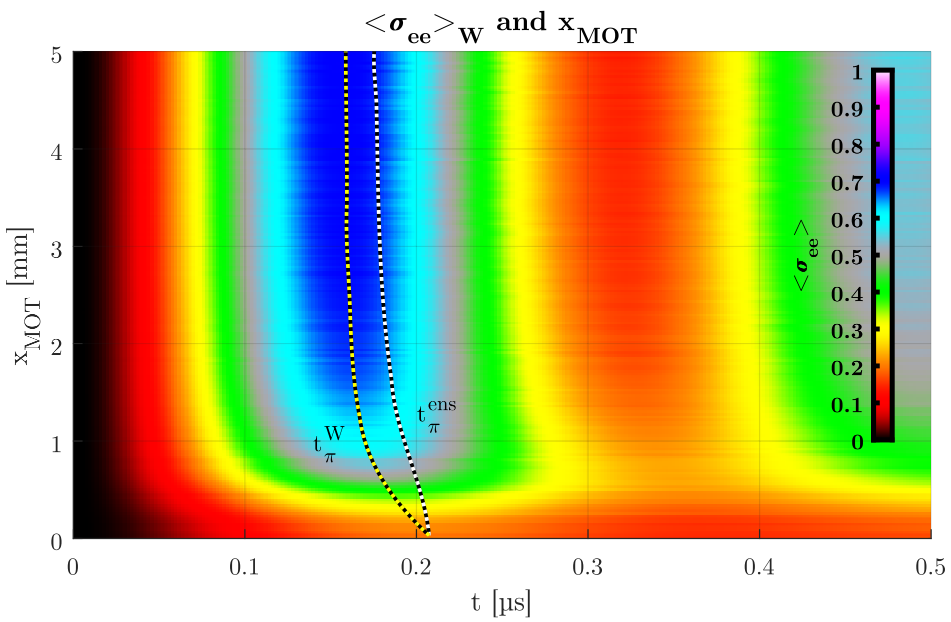

Figure A.2: *Population dynamics within the cavity waist for varying x_{MOT}.*

A.2 Simulations for the Seed Laser Power Experiment

Here we show additional simulations compared to the experimental data of Section 5.3.5.

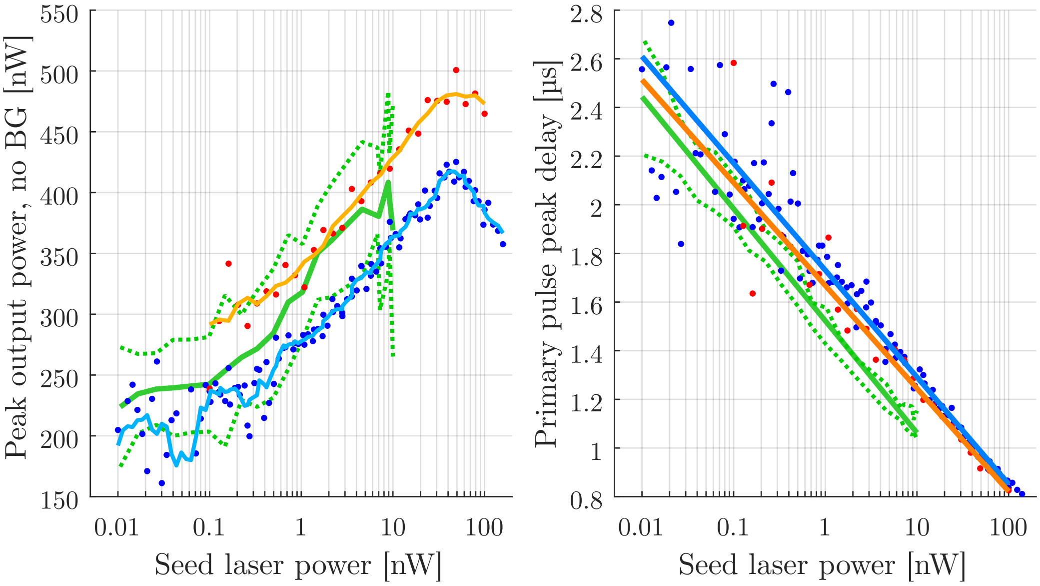

Figure A.3: *Peak output power from one mirror with background subtracted (left) and peak delay with respect to the pump pulse (right), depending on the seed laser power. Green: experimental results. Rest: Simulations for P_p = 100 mW, R = 0.8 mm, T = 3 mK, y_{MOT} = 4 mm and $W_{py} = W_{pxz}$ = 2.5 mm.*
Orange: $N = 49 \cdot 10^6$, blue: $N = 45 \cdot 10^6$.

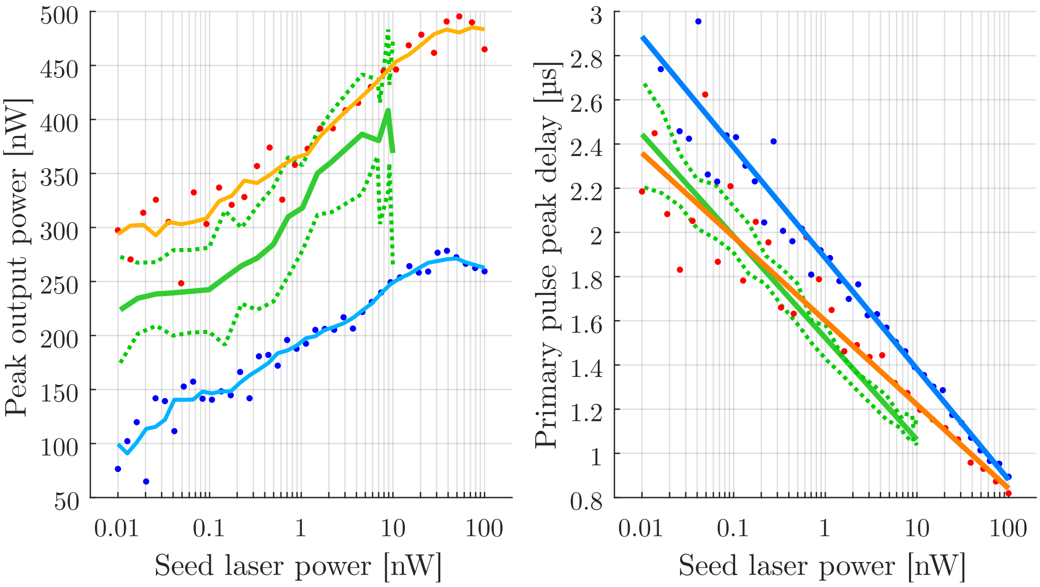

Figure A.4: *Same format as Fig. A.3. Simulation parameters: P_p = 100 mW, R = 0.8 mm, T = 2 mK, y_{MOT} = 4 mm and $W_{py} = W_{pxz}$ = 2.5 mm.*
Orange: $N = 40 \cdot 10^6$, blue: $N = 30 \cdot 10^6$.

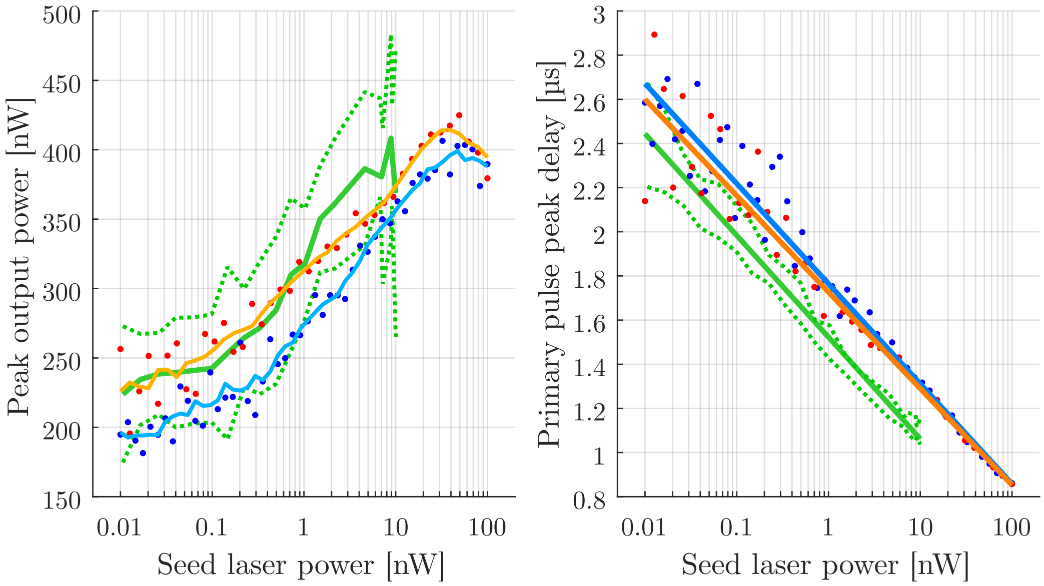

Figure A.5: *Same format as Fig. A.3. Simulation parameters:* $P_p = 100$ *mW,* $R =$ *0.8 mm,* $T =$ *3 mK,* $y_{MOT} =$ *1.5 mm,* $W_{p1} =$ *1.36 mm,* $W_{p2} =$ *2.13 mm and* $\theta_p = 39.2°$. *Orange:* $N = 45 \cdot 10^6$, *blue:* $N = 40 \cdot 10^6$.

Bibliography

[1] G. Kazakov and T. Schumm (2014) *Active optical frequency standards using cold atoms: Perspectives and challenges*, European Frequency and Time Forum (EFTF), Neuchatel, 2014, pp. 411-414
DOI: 10.1109/EFTF.2014.7331523 arXiv: https://arxiv.org/abs/1503.03998
(Retrieved August 5, 2018)

[2] G. Kazakov and T. Schumm (2013) *Active optical frequency standard using sequential coupling of atomic ensembles*, Phys. Rev. A, vol. 87, no. 1
DOI: 10.1103/PhysRevA.87.013821 (Retrieved June 28, 2018)

[3] C. W. Chou et al. (2010) *Frequency Comparison of Two High-Accuracy Al^+ Optical Clocks*, Phys. Rev., vol. 104, iss. 7
DOI: https://doi.org/10.1103/PhysRevLett.104.070802 (Retrieved July 9, 2018)

[4] B. P. Abbott et al. (2016) *Observation of Gravitational Waves from a Binary Black Hole Merger*, Phys. Rev., vol. 116, iss. 6
DOI: https://doi.org/10.1103/PhysRevLett.116.061102 (Retrieved July 9, 2018)

[5] P. Milonni and J. Eberly (2010). *Laser Physics.* John Wiley & Sons.

[6] T. L. Nicholson et al. (2015) *Systematic evaluation of an atomic clock at $2 \cdot 10^{-18}$ total uncertainty*, Nat. Commun. 6, 6896
DOI: 10.1038/ncomms7896 (Retrieved July 29, 2018)

[7] H. Bruus and K. Flensberg (2016). *Many-Body Quantum Theory in Condensed Matter Physics - An Introduction.* Oxford Graduate Texts.

[8] G. M. Moy, J. J. Hope, and C. M. Savage (1999) Born and Markov approximations for atom lasers, Phys. Rev. A, vol. 59, no. 1
journals.aps.org/pra/abstract/10.1103/PhysRevA.59.667 (Retrieved June 15., 2018)

[9] Thomas M. Barlow, Robert Bennett and Almut Beige (2015) A master equation for a two-sided optical cavity, Journal of Modern Optics
DOI: 10.1080/09500340.2014.992992 (Retrieved May 14., 2018)

[10] C. Gerry and P. Knight (2008). *Introductory Quantum Optics.* Cambridge University Press.

[11] Daniel A. Steck, Quantum and Atom Optics, available online at steck.us/teaching (revision 0.12.0, 16 May 2017)

[12] Andrée Tallet, "Raman emission versus dopplerons in a two-level atomic cell," J. Opt. Soc. Am. B 11, 1336-1349 (1994)
www.osapublishing.org/josab/abstract.cfm?uri=josab-11-8-1336 (Retrieved May 16, 2018)

[13] D. Walls and G. Milburn (1995). *Quantum Optics.* Springer-Verlag.

[14] L. Mandel and E. Wolf (1995). *Optical Coherence and Quantum Optics.* Cambridge University Press.

[15] R. Brecha et al. (1995). *Observation of oscillatory energy exchange in a coupled-atom–cavity system*, J. Opt. Soc. Am. B, vol. 12, no. 12, 2329-2339
DOI: 10.1364/JOSAB.12.002329 (Retrieved July 4, 2018)

[16] R. H. Dicke (1954). *Coherence in Spontaneous Radiation Processes*, Phys. Rev., vol. 93, iss. 1
DOI: 10.1103/PhysRev.93.99 (Retrieved July 30, 2018)

[17] M. A. Norcia et al. (2018) *Frequency Measurements of Superradiance from the Strontium Clock Transition*, Phys. Rev. X, vol. 8, iss. 2
DOI: 10.1103/PhysRevX.8.021036 (Retrieved July 30, 2018)

[18] D. E. Chang (2018) *Quantum optics using ordered atomic arrays*, The 26th International Conference on Atomic Physics, Book of Abstracts p. 87
URL: http://icap2018.eu/book-of-abstracts/ (Retrieved July 30, 2018)

[19] C. S. Adams et al. (2018) *Engineering collective light-matter interactions*, The 26th International Conference on Atomic Physics, Book of Abstracts p. 93
URL: http://icap2018.eu/book-of-abstracts/ (Retrieved July 30, 2018)

[20] M. Xu. (2016) *Theory of Steady-State Superradiance*, Physics Graduate Theses & Dissertations. 166.
URL: https://scholar.colorado.edu/phys_gradetds/166 (Retrieved July 30, 2018)

[21] R. Bonifacio and L. A. Lugiato (1974) *Cooperative radiation processes in two-level systems: Superfluorescence*, Phys. Rev. A, vol. 11, no. 5
DOI: 10.1103/PhysRevA.11.1507 (Retrieved August 1, 2018)

[22] A. Kumarakrishnan and X. Han (1998) *Superfluorescence from optically trapped calcium atoms*, Phys. Rev. A, vol. 58, no. 5
DOI: 10.1103/PhysRevA.58.4153 (Retrieved August 1, 2018)

[23] J. A. Muniz et. al, (2018) *A Robust Narrow-Line Magneto-Optical Trap using Adiabatic Transfer*
https://arxiv.org/abs/1806.00838 (Retrieved June 30, 2018)

[24] The tapered amplifier specifications are available at:
https://www.eagleyard.com/fileadmin/downloads/data_sheets/EYP-TPA-0690-00500-2003-CMT02-0000_01.pdf (Retrieved July 5, 2018)

[25] The ISOMET Model 1201E-1 specifications are available at:
http://www.isomet.com/AO_Pdf/1201e.pdf (Retrieved July 4, 2018)

[26] The ISOMET Model 1201E-1 manual is available at:
ISOMET Acousto-Optic Modulation Application Note (Retrieved July 4, 2018)

[27] The Casio EX-ZR100 manual is available at:
http://support.casio.com/manualfile.php?rgn=4&cid=001022003 (Retrieved July 10, 2018)

[28] B. T. R. Christensen (2016) *Laser Stabilization With Laser Cooled Strontium*, PhD Thesis, Niels Bohr Institute, University of Copenhagen
URL: ultracold-atoms.nbi.ku.dk/research/theses_conference/ (Retrieved August 2, 2018)

[29] S. A. Schäffer (2015) *Cavity Enhanced Spectroscopy on Ultra Cold Atoms*, M.Sc. Thesis, Niels Bohr Institute, University of Copenhagen
URL: ultracold-atoms.nbi.ku.dk/research/theses_conference/ (Retrieved August 2, 2018)

[30] Wang Shao-Kai et al. (2009) *Cooling and Trapping ^{88}Sr Atoms with 461 nm Laser*, Chinese Physics Letters, vol. 26, no. 9
DOI: https://doi.org/10.1088/0256-307X/26/9/093202 (Retrieved July 15, 2018)

[31] Gang Zhao et al. (2017) *Differential noise-immune cavity-enhanced optical heterodyne molecular spectroscopy for improvement of the detection sensitivity by reduction of drifts from background signals*, Opt. Express 25, 29454-29471
URL: https://www.osapublishing.org/oe/abstract.cfm?uri=oe-25-23-29454 (Retrieved July 11, 2018)

[32] P. K. Lam et al. (2018) *Multiparameter Optimisation of a Magneto-Optical Trap Using Deep Learning Artificial Neural Networks*, The 26th International Conference on Atomic Physics, Book of Abstracts p. 53
URL: http://icap2018.eu/book-of-abstracts/ (Retrieved July 30, 2018)